LS Scienza dei Materiali - a.a. 2005/06

Fisica delle Nanotecnologie – part 10

Microscopia a scansione di sonda per nanoscopia e nanomanipolazione

15/12/2005 – 16.30-18 – room T1

Introduction: need for higher resolution tools I

- Due to diffraction, optical methods fail in poviding the required space resolution

- Nanometer or even sub-nanometer resolution can be achieved by using electron microscopy (SEM, TEM)

BUT

➢ Contrast mechanism in electron microscopy are often indirect (they imply many effects)
➢ Morphology can be quantitatively derived only for the in-plane features (poor info on the relative height)
➢ Samples must be frequently prepared (made conductive, cut in thin slices,…)
➢ ***Specific physical quantities (e.g., the local density of states, the magnetic or electrical polarization, the surface optical properties,…) cannot be directly measured***

Ability to measure local ("point") physical quantities is required to investigate nanotechnology products

Introduction: need for higher resolution tools II

ON THE OTHER HAND

- Optical lithography is unable to provide material control at the desired level
- In a conventional context, electron beam lithography (EBL) can be used with excellent space resolution results

BUT

- ➢ Both optical and electron lithographies are thought essentially for top-down approaches
- ➢ EBL involves accelerated charges, in a process inherently destructive
- ➢ Bottoms-up approaches, based, e.g., on nanoparticles, nanotubes, organics, are hardly compatible with the "aggressive" technology which has been developed for inorganics (silicon technologies)
- ➢ *New, more flexible and more "gentle" techniques must be designed to access the full potential of nanotechnologies, at least in the laboratory environment (i.e., not necessarily suited for the industry)*

Ability to manipulate the matter at the nanometer level is required to produce new nanotechnology

Basics of Scanning Probe Microscopy (SPM)

Scanning: piezoelectric translator
Probe: tip probing local properties
Microscopy: sub-micrometer resolution
(+ system to control tip/sample distance
+ electronics for instrument operation)

Developed starting since '80s thanks to:

✓ Piezo translators with sub-nm resolution;
✓ sub-nm probes

Probe tip

Sample

z

x
Fast scan

y

Slow scan

Piezoelectric scanner
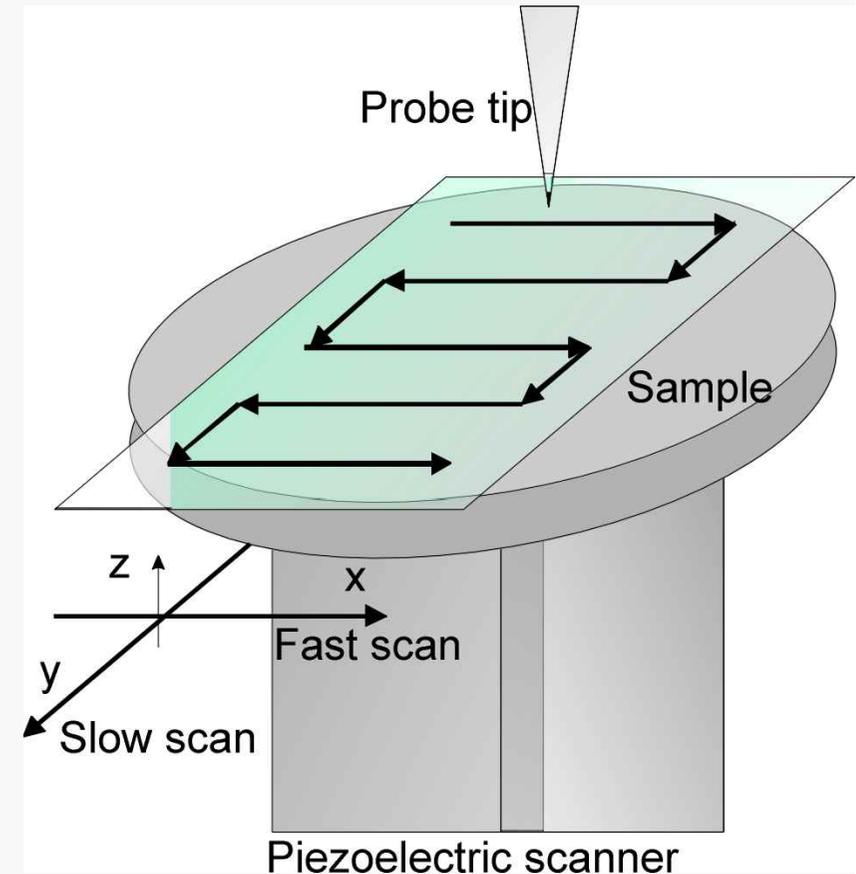
Various physical quantities can be measured point-by-point during the scan and an image (i.e., a map of the quantity) can be built

A few examples of SPMs

Technique	Probed quantity	Resolution
STM	Electron tunneling	atomic
AFM	Mechanical force	1 nm
SFFM	Friction force	
MFM	Local magnetization	
EFM	Local polarization	10 nm
SNOM	Optical properties	
Ap-SNOM	Optical properties	50 nm
...	...	

SFM { AFM, SFFM, MFM, EFM }

Depending on the probe and on its interaction with the surface, a variety of quantities can be investigated

Outlook

1. The mother of all SPMs: Scanning Tunneling Microscopy (STM):
    mechanisms and instruments to investigate local electronic properties

2. SPM based on probing mechanical forces:
    A. Atomic Force Microscopy (AFM);
    B. Variants (lateral, electrostatic, magnetic forces,...)

3. Sub-diffraction properties of electromagnetic waves:
    A. Scanning Near Field Optical Microscopy (SNOM);
    B. Polarization-Modulation SNOM

4. "Lithographies" (better stated as "nanomanipulations") associated with:
    A. STM;
    B. AFM;
    C. SNOM

A few details: piezoelectric scanner

...coefficient d is negative representing contraction perpendicular to the field; and positive for stain measured along the 3-direction (along which the thickness t is measured) representing expansion parallel to the electric field direction:

$$\Delta t = d_{33} V . \qquad (4.4)$$

Although there are many ceramic compositions used today, most can be placed into two general categories: hard and soft PZT materials. Typical d coefficients for hard PZT materials are

$$d_{33} = 250 \cdot 10^{-12} \text{ m/V} , \quad d_{31} = -110 \cdot 10^{-12} \text{ m/V} ;$$

and for soft PZT materials

$$d_{33} = 600 \cdot 10^{-12} \text{ m/V} , \quad d_{31} = -270 \cdot 10^{-12} \text{ m/V} .$$

For PZT-5H

$$d_{33} = 593 \cdot 10^{-12} \text{ m/V} , \quad d_{31} = -273 \cdot 10^{-12} \text{ m/V} .$$

Typ: hollow tubes made of PZT-based ceramics with a multi-electrode configuration aimed at controlling the displacement along different directions.

Main issues:
- Linearity (possibly closed loop);
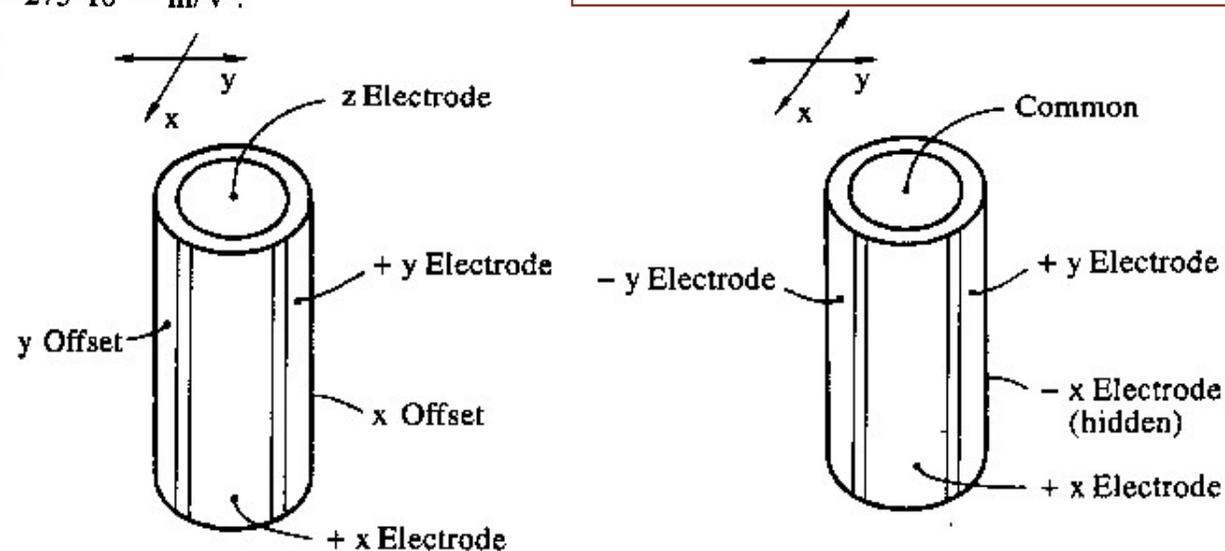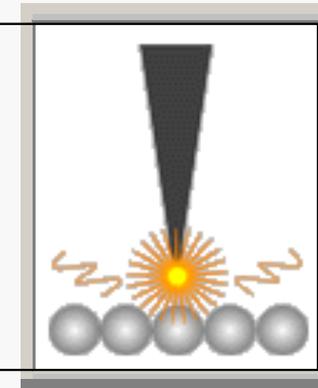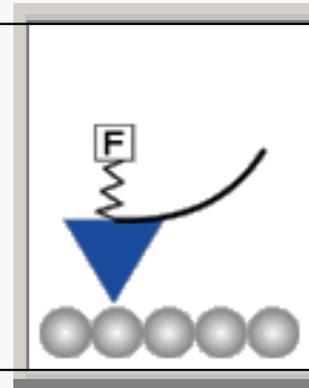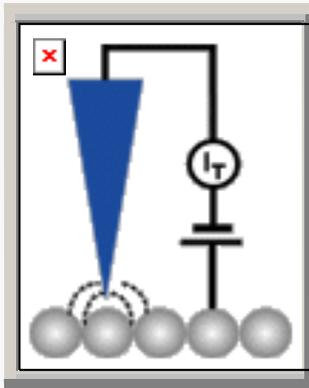- Hysteresis;
- Distorted motion (*artifacts*).

Fig. 4.5. Illustrating the voltages applied to the electrodes of the single-tube scanner
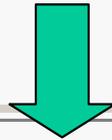
Da C. Bai, STM and its applications
(Springer, 1995)

1. Scanning Tunneling Microscopy (STM)

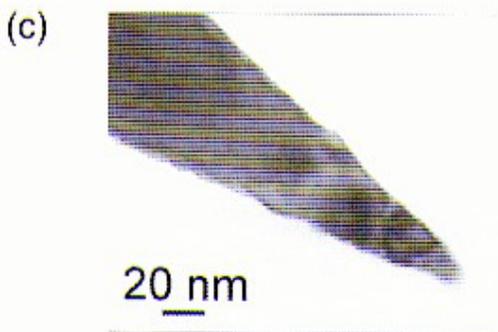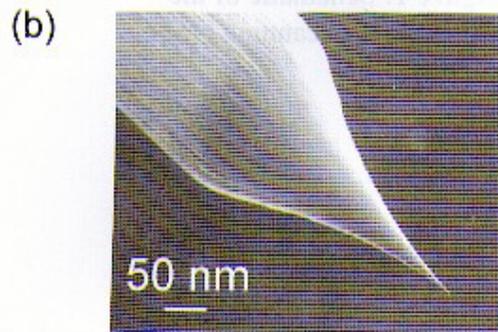|		
STM Scanning Tunneling Microscope (STM)	**AFM** Atomic Force Microscope (AFM)	**SNOM** Scanning Near field Optical Microscope (SNOM)
Electron tunneling	**Force microscopy**	**Optical near-field**
Locally probed quantity		

Historically, STM is the first working realization of SPM, and probably the simplest

STM tip (probe) preparation

Fig. 4.12. (a) Schematic diagram of the electrochemical cell showing the tungsten wire (anode) being etched in NaOH. The cathode consists of a stainless-steel cylinder which surrounds the anode. (b) Sketch of the etching mechanism showing the "flow" of the tungstate anion down the sides of wire in solution [4.13]

cathode: $6H_2O + 6e^- \rightarrow 3H_2(g) + 60H^-$ SRP $= -2.45$ V

anode: $W(s) + 80H^- \rightarrow WO_4^{2-} + 4H_2O + 6e^-$ SOP $= +1.05$ V

$W(s) + 20H^- + 2H_2O \rightarrow WO_4^{2-} + 3H_2(g)$ $E^0 = -1.43$ V.

Electrochemical etching of W or Pt/Ir typ used

Very sharp tips can be obtained (ideally, terminated by a "single" atom)
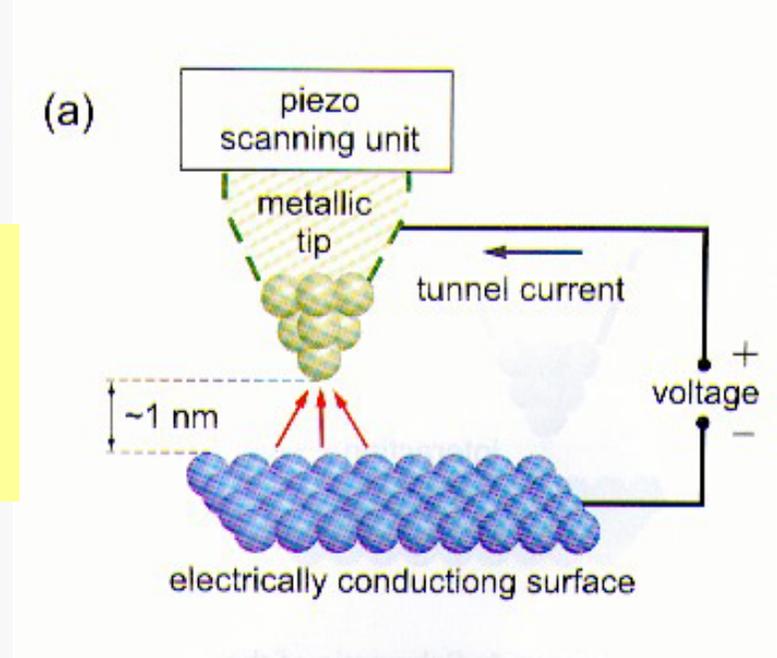
Basics of Scanning Tunneling Microscopy

Tip is scanned relative to the sample
(or sometimes the sample is scanned)

Tip measures
some property of
the surface

A feedback mechanism
is used to maintain the
tip at a constant height
above the sample

**The feedback provides a true (absolute)
measurement of the height (topography)**

control voltages for piezotube

piezoelectric tube
with electrodes

tunneling
current
amplifier

distance control
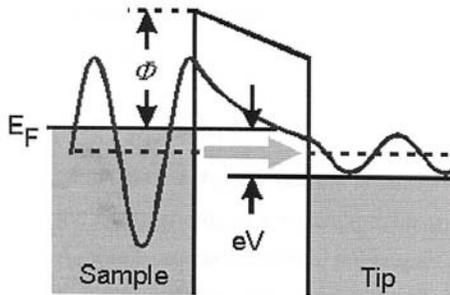and scanning unit

tip

sample

tunneling
voltage

data processing
and display

BIAS voltage

STM:
- ✓ Probe is a conductive tip
- ✓ Sample (surface) is mostly conductive or semiconductive
- ✓ A bias voltage is applied between sample and tip
- ✓ *Tip is kept at small distance from the surface (typ < 1 nm)*
- ✓ Tunneling current (typ in the pA range) is measured

Tunneling current

2.1. Electron Tunneling

In classical physics an electron cannot penetrate into or across a potential barrier if its energy E is smaller than the potential Φ within the barrier. A quantum mechanic treatment predicts an exponential decaying solution for the electron wave function in the barrier. For a rectangular barrier we get

$$\Psi(d) = \Psi(0)e^{-\kappa d} \qquad \text{where} \quad \kappa = \frac{\sqrt{2m(\Phi - E)}}{\hbar}$$

Extinction length

The probability of finding an electron behind the barrier of the width d is

$$W(d) = |\Psi(d)|^2 = |\Psi(0)|^2 e^{-2\kappa d}$$

Exponential decrease

In scanning tunneling microscopy a small bias voltage V is applied so that due to the electric field the tunneling of electrons results in a tunneling current I. The height of the barrier can roughly be approximated by the average workfunction of sample and tip.

$$\Phi = 1/2(\Phi_{sample} + \Phi_{tip})$$

If the voltage is much smaller than the workfunction $eV \ll \Phi$ the inverse decay length for all tunneling electrons can be simplified to

$$\kappa \approx \frac{\sqrt{2m\Phi}}{\hbar}$$

The current is proportional to the probability of electrons to tunnel through the barrier:

$$I \propto \sum_{E_n = E_F - eV}^{E_F} |\Psi_n(0)|^2 e^{-2\kappa d}$$

By using the definition of the local density of states for $\varepsilon \to 0$

$$\rho(z, E) \equiv \frac{1}{\varepsilon} \sum_{E_n = E - \varepsilon}^{E} |\Psi_n(z)|^2$$

Local density of states

the current can be expressed by

$$I \propto V\rho_{sa}(0, E_F)e^{-2\kappa d} \qquad (*)$$

$$\approx V\rho_{sa}(0, E_F)e^{-1.025\sqrt{\Phi}d} \quad \text{where} \quad [d] = \mathring{A}; \; [\Phi] = eV;$$

With 5eV as typical example for a workfunction value a change of 1Å in distance causes a change of nearly one order of magnitude in current. This facilitates the high vertical resolution.

Also

$$I \propto V\rho_{sa}(d, E_F)$$

which means that the current is proportional to the local density of states of the sample at the Fermi energy at a distance d, i.e. the position of the tip.

A more exact calculation of the current density of the square barrier problem requires the Schrödinger's equation to be solved in the three regions: before, in and behind the barrier. The coefficients have to be adapted so that the overall solution is continually differentiable.
Defining the transition probability as

$$T = \frac{j_T}{j_i}$$

yields

$$T = \frac{16E(V - E)}{V^2}e^{-2\kappa d}; \qquad \kappa = \sqrt{\frac{2m(V - E)}{\hbar^2}}$$
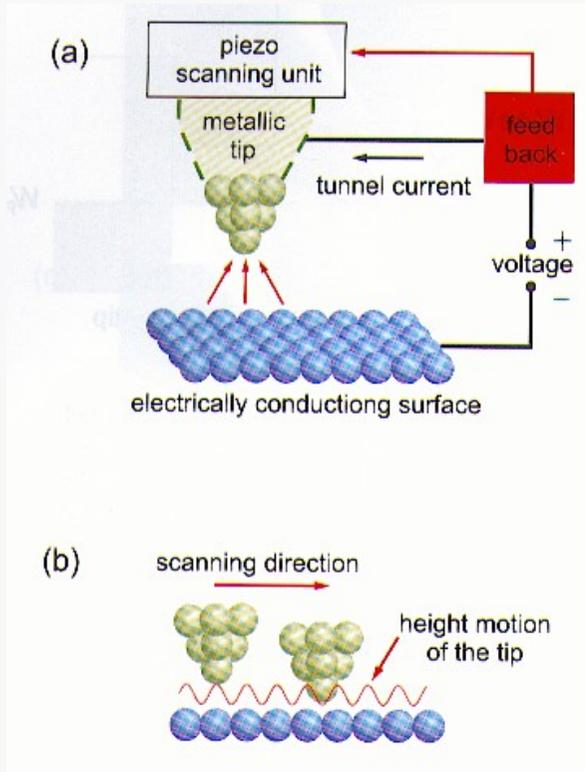
with the approximation $\kappa d \gg 1$.
The current density itself is defined as

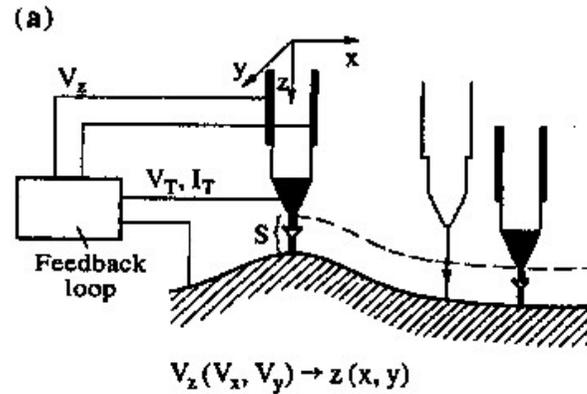$$j_z = -\frac{i\hbar}{2m}\left(\Psi^*(z)\frac{d\Psi}{dz} - \Psi(z)\frac{d\Psi^*}{dz}\right)$$

For a nonsquare potential the WKB method must be used. This is more adequate as the potential is changed by the applied voltage and influenced by the image force on the electron. The WKB method yields a transition probability of

$$T(E) \propto \exp\left(-\frac{2}{\hbar}\int_0^1 \sqrt{2mV(z) - E}\,dz\right)$$

Modes of operation in STM

(a)
piezo scanning unit
metallic tip
feed back
tunnel current
voltage
electrically conductiong surface

(b)
scanning direction
height motion of the tip

Constant current

Constant height

(a)

V_z

V_T, I_T

Feedback loop

S

$V_z(V_x, V_y) \rightarrow z(x, y)$

(b)

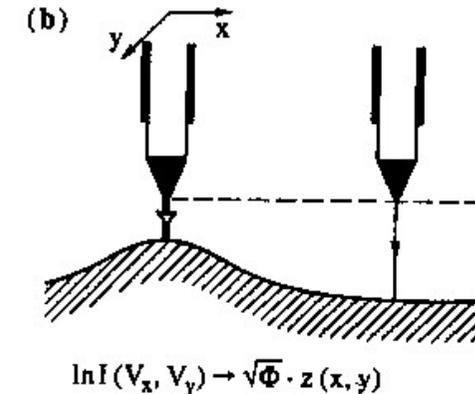$\ln I(V_x, V_y) \rightarrow \sqrt{\Phi} \cdot z(x, y)$

Fig. 1.2a,b. Schematic view of two modes of operation in STM [1.10]. S is the gap between the tip and the sample, I and V_T are the tunneling current and bias voltage, respectively, and V_z is the feedback voltage controlling the tip height along the z direction. (a) constant-current mode and (b) constant-height mode

2.2 Operating Modes of the Scanning Tunneling Microscope

Up to now, the theoretical background of a scanning tunnelling microscope has been presented, but nothing has been said about the experimental operation of a scanning tunnelling microscope. The simplest way to obtain a scanning tunnelling microscope image is to directly measure the variation of the tunnel current as a function of the scanning position while keeping the distance between tip and sample surface constant. A so-called current image is then obtained. Instead of directly recording the atomic variation of the current, however, the usual procedure is to keep the tunnel current constant while scanning over the surface. This is done by changing the distance between tip and surface using a feedback loop (Figure 8). In order to get an image, the voltage required at the piezoelectric crystal to adjust the distance is recorded. One obtains a so-called constant-current STM image.

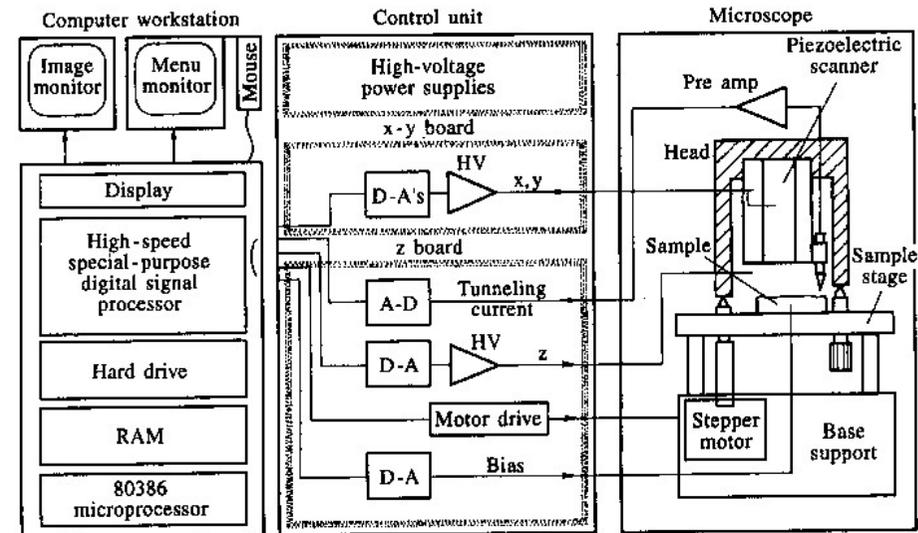**Fig. 4.27.** Block diagram of the STM control, data acquisition and display system indicating all of the equipment connections

Feedback loop used to keep constant the tunneling current → "absolute" topography map

Bardeen (quantum) approach to tunneling

2.2. Bardeen Approach

Another way of describing electron tunneling comes from Bardeen's approach which makes use of the time dependent perturbation theory. The probability of an electron in the state Ψ at E_Ψ to tunnel into a state χ at E_χ is given by Fermi's Golden Rule

Quantum mech. Treatment

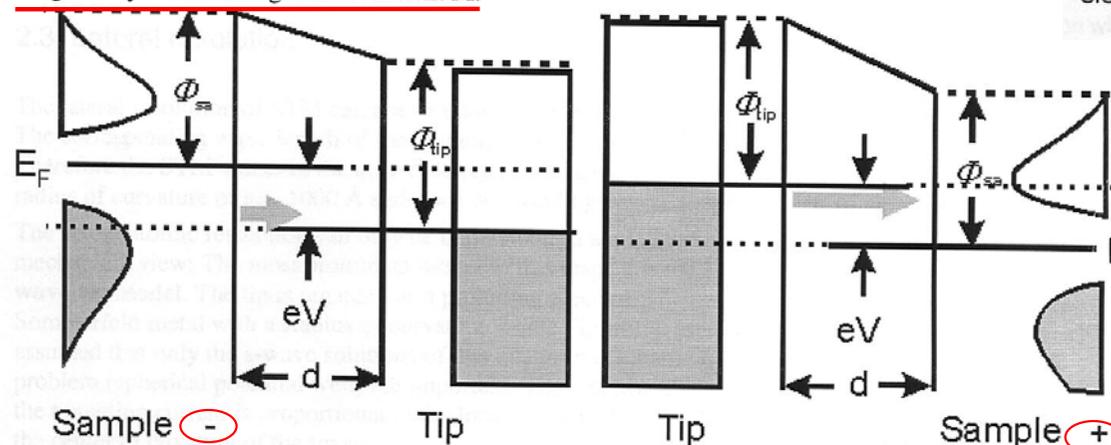$$w = \frac{2\pi}{\hbar} |M|^2 \delta(E_\Psi - E_\chi)$$

The tunneling matrix element is given by an integral over a surface in the barrier region lying between the tip and the sample:

$$M = \frac{\hbar}{2m} \int_{z=z_0} \left(\chi^* \frac{\partial \Psi}{\partial z} - \Psi \frac{\partial \chi^*}{\partial z} \right) dS$$

Applying a bias voltage V and approximating the Fermi distribution as a step function ($kT \ll \Delta E_{resolution}$), the current is
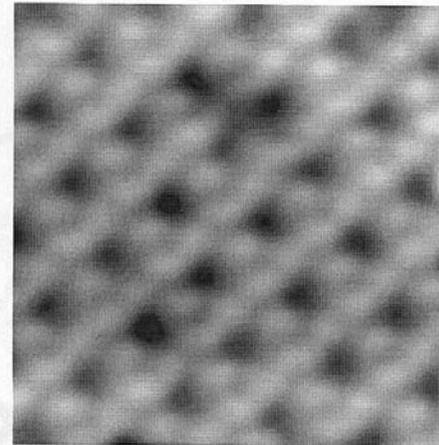
$$I = \frac{4\pi\, e}{\hbar} \int_0^{eV} \rho_{sa}(E_F - eV + \varepsilon)\, \rho_{tip}(E_F + \varepsilon)\, |M|^2 d\varepsilon \quad (**)$$

Hence the current is given by a combination of the local densities of states of the sample and the tip, weighted by the tunneling matrix element M.
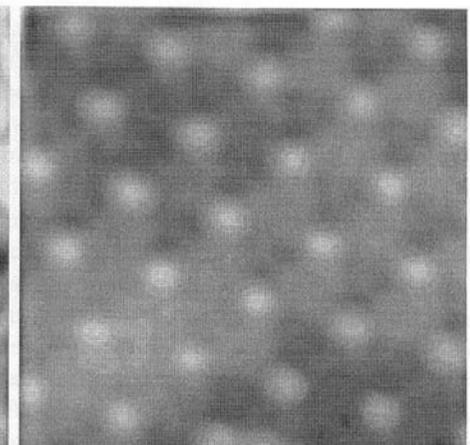

Imaging the occupied states of SiC(000$\bar{1}$)3x3

Imaging the unoccupied states of SiC(000$\bar{1}$)3x3

Schematic of electron tunneling with respect to the density of states of the sample.

Local density of states is actually imaged in STM

$\delta(E_\Psi - E_\chi)$ means that an electron can only tunnel if there is an unoccupied state with the same energy in the other electrode (thus inelastic tunneling is not treated). In case of a negative potential on the sample the occupied states generate the current, whereas in case of a positive bias the unoccupied states of the sample are of importance. Therefore, as shown below, by altering the voltage, a complete different image can be detected as other states contribute to the tunneling current. This is used in tunneling spectroscopy. It should finally be mentioned that the probability of tunneling (expressed by M^2) is larger for electrons which are close to the fermi edge due to the lower barrier.

Tunneling current and STM

2.1 Theoretical Fundamentals of the Scanning Tunneling Microscope

How does a measuring instrument function that allows us to see *single atoms*? In the case of a *scanning tunnelling microscope* a fine metallic tip is used as the probe (called *tunnelling tip*) (see Figure 3). This tip is approached toward the surface until a current flows when a voltage is applied between the tip and the sample surface. This happens at distances in the order of 1 nm. The current is called tunnel current since it is based on the quantum-mechanical *tunnel* effect. After a tunnelling contact is established, the tip is moved over the surface by a piezoelectric *scanning* unit, whose mechanical extension can be controlled by applying appropriate voltages. The scanning unit is typically capable of scanning an area of a few nm up to several μm. This allows us to obtain a *microscopic* image of the spatial variation of the tunnel current. Hence the name *scanning tunnelling microscope*.

- A metallic tip is moved as probe towards a conducting surface up to a distance of about 1 nm
- With an applied voltage a current flows due to the **tunnel** effect (tunnel current)
- The spatial variation of the tunnel current is measured by **scanning** over the sample surface
- A **microscopic** image of the surface is produced

At this stage we have to ask what kind of atomic-scale structures can be made visible by the scanning tunnelling microscope utilising the tunnel effect? These structures must by nature correspond to electrical states from or into which the electrons can tunnel. In the tunnelling process, the electrons must tunnel through the vacuum barrier between tunnelling tip and sample, which represents a potential barrier. The tunnel effect allows a particle (here an electron) to tunnel through this potential barrier even though the electron's energy is lower than the barrier height. The probability of such a process decreases exponentially with the geometrical distance between the tip and the sample and with increasing barrier height. An experimental apparatus making use of the tunnel effect must therefore minimise the potential barrier to be tunnelled through. This is realised in the scanning tunnelling microscope configuration by moving the tip very close (about 1 nm) to the surface. The electrons can then pass between the surface and the tip. The direction of the tunnel current is fixed by applying a voltage between sample and tip.

In order to explain and interpret the images of the surface states obtained in this way, efforts to develop a theory were made very soon after the invention of the scanning tunnelling microscope. One of the possible theoretical approaches is based on Bardeen's idea of applying a transfer Hamiltonian operator to the tunnelling process [2]. This had the advantage of adequately describing the many-particle nature of the tunnel junction. In the model, a weak overlap of the wave functions of the surface states of the two electrodes (tunnelling tip and sample surface) is assumed to allow a perturbation calculation. On this basis, Tersoff and Hamann developed a simple theory of scanning tunnelling microscopy [3], [4] Hence follows the tunnel current:

$$I \sim V \cdot \rho_{\text{tip}}(W_{\text{F}}) \cdot \rho_{\text{sample}}(r_0, W_{\text{F}}) \qquad (1)$$

The tunnelling tip is assumed to be a metallic s-orbital as shown schematically in Figure 4. In addition, it is assumed that low voltages V (i.e., much smaller than the work function) are applied. $\rho_{\text{tip}}(W_{\text{F}})$ is the density of states of the tip and $\rho_{\text{sample}}(r_0, W_{\text{F}})$ is that of the sample surface at the centre r_0 of the tip orbital and at the Fermi energy W_{F}. Eq. (1) shows that at low voltage *the scanning tunnelling microscope thus images the electronic density of states at the sample surface near the Fermi energy*. However, this result also means that the scanning tunnelling microscope images do not directly show the atoms, but rather the electronic states bound to the atoms. As can be seen in Eq. (1), the tips density of states enters in the measurement in the same way as the density of states of the sample. It is therefore desirable to know the exact electronic state of the tip, but unfortunately, in practice, every tip is different and the details remain unknown.

- Weak overlap of the wave functions of the surface states of the two electrodes (tunnelling tip and sample surface)
- Tunnelling tip approximated as an s-orbital
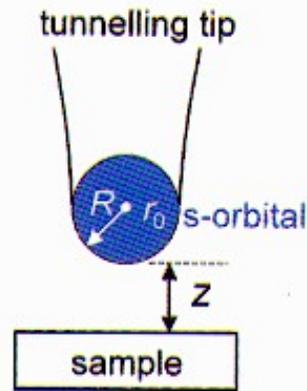- Low voltages ($V \ll$ work function)

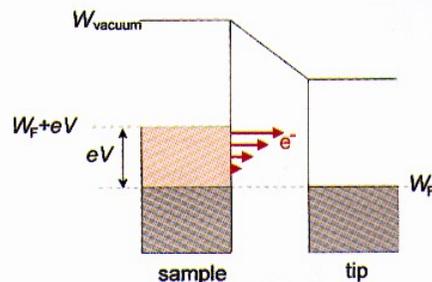**Figure 4:** Schematic representation of the tunnelling geometry in the Tersoff-Hamann model.

Figure 5: At high voltages not only the states near the Fermi energy W_{F} contribute to the current but all states whose energy ranges between W_{F} and $W_{\text{F}}+eV$.

Extension to "high" bias

- The tunnel current is proportional to the local density of states of the sample
- The scanning tunnelling microscope images the electronic local density of states of the sample near the Fermi energy.

In a first approximation the density of surface states decreases exponentially into the vacuum with the effective inverse decay length k_{eff}

$$k_{\text{eff}} = \sqrt{\frac{2m_{\text{e}}B}{\hbar^2} + |k_{\parallel}|^2} \qquad (2)$$

m_{e} is the electron mass and $k_{\parallel}$ is the parallel wave vector of the tunnelling electrons. B is the barrier height, which is approximately a function of the applied voltage V and the work functions Φ_{sample} and Φ_{tip} of the sample and tip [5], respectively:

$$B = \frac{\Phi_{\text{tip}} + \Phi_{\text{sample}}}{2} - \frac{|eV|}{2} \qquad (3)$$

The tunnel current thus decreases exponentially with the tip-sample distance z:

$$I \sim exp\left[-2k_{\text{eff}}\, z\right] \qquad (4)$$

The exponential current-voltage dependence is quite essential for the high measurement accuracy of a scanning tunnelling microscope, since even small changes in distance may cause a large change in the tunnel current. Thus the tip just needs one microtip, which is only about 0.1 nm closer to the surface than the next one, and still all current flows over only the closest microtip. Thus even apparently wide tips can yield atomic resolution via one microtip.

The description of the tunnel current by Eq. (1) however, has an important restriction: it strictly speaking only applies to low voltages V. In particular for the investigation of semiconductor surfaces voltages of the order of 2 to 3 V are required due to the existence of a band gap. Thus the theory must be extended. The simplest extension yields:

$$I \sim \int_{W_{\text{F,tip}}}^{W_{\text{F,tip}}+eV} \rho_{\text{tip}}(W)\rho_{\text{sample}}(W+eV)\ T(W,V)\ \mathrm{d}W \qquad (5)$$

$T(W,V)$ is a transmission coefficient which depends on the energy of the electrons and the applied voltage. The tunnel current is composed of the product of the density of states of the tip and sample at all the different electron energies that are allowed to participate in the tunnelling process (Figure 5). For example, an image measured at -2 V applied to the sample, consequently shows all occupied sample states with an energy between the Fermi energy and 2 eV below the Fermi energy. Tunnelling at a positive voltages analogously provides a measurement of the empty surface states in an energy interval determined again by the voltage.

In order to illustrate this effect more clearly, in the following the InP(110) surface will be presented. On InP(110) surfaces two electrical states exist near the surface: an occupied state below the valence band edge and an empty state above the conduction band edge (Figure 6). All the other states are located geometrically deeper in the crystal or energetically deeper in the bands. They thus contribute little to the tunnel current.

Lateral resolution in STM
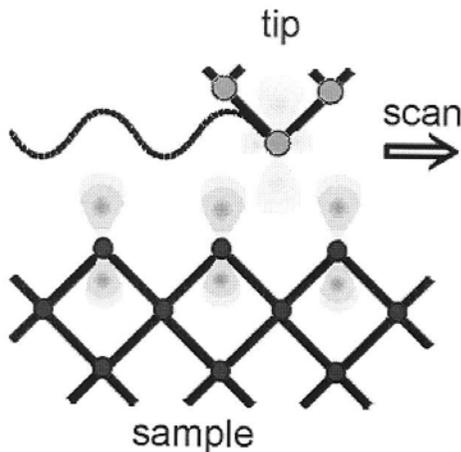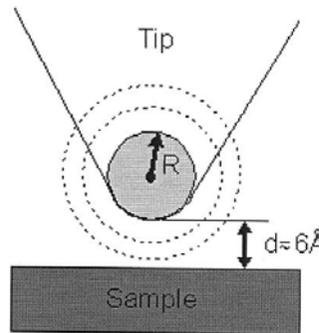
2.3. Lateral resolution

The lateral resolution of STM <u>can not be understood in terms of a Fraunhofer diffraction resolution.</u> The corresponding wave length of the tunneling electron would be $\lambda > 10$ Å. <u>Therefore the STM works in the near-field regime.</u> The overall geometric curvature of the tip with a radius of curvature of e.g. 1000 Å and $x = 1$ Å^{-1} would give rise to a resolution of about 50 Å.

The actual atomic resolution can only be understood in a quantum mechanical view: The most prominent model in this respect is the **s-wave-tip model**. The tip is regarded as a protuding piece of Sommerfeld metal with a Radius of curvature R (see Figure). It is assumed that only the s-wave solutions of this quantum mechanical problem (spherical potential well) are important. Thus, at low bias the tunneling current is proportional to the local density of states at the center of cuvature of the tip r_0:

$$I \propto \sum_{E_k = E_r - eV}^{E_r} \left| \Psi_\mu(\mathbf{r}_0) \right|^2 = eV \rho_{sa}(\mathbf{r}_0, E_F)$$

In this model only the properties of the sample contribute to the STM image which is quite easy to handle. But it cannot explain the atomic resolution.

Calculations and experiments showed that there is often a d_z^2 like state near the fermi edge present at the apex atom which also predominantely contributes to the tunneling current. It is understood that this state (and also the p_z like state) is advantageous for a „sharp„ tip. Since the tunneling current is a convolution of the tip state and the sample state, there is a symmetry between both: By interchanging the electronic state of the tip and the sample state, the image should be the same (reciprocity principle). This can also explain the fact that the corrugation amplitude of an STM image is often larger than that of the LDOS of the sample (measured by helium scattering). In this case the tip traces a fictitious surface with a d_z^2 like state. The state of the tip atom is dependent on the material and the orientation. As the tip is quite difficult to handle, it is one of the most difficult problems in a STM experiment.

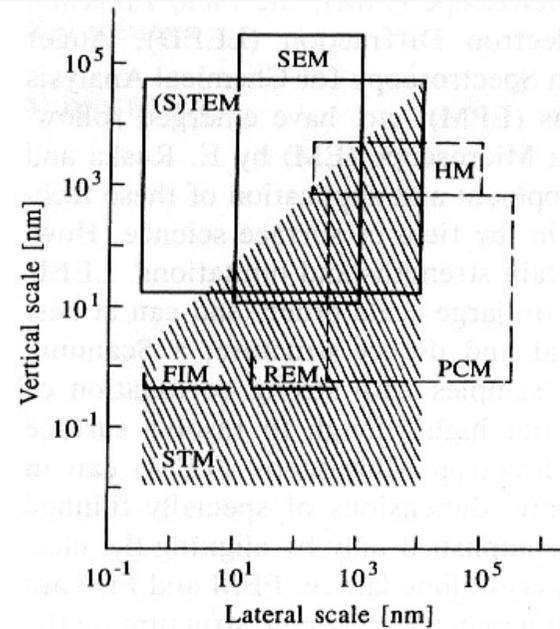Interaction which causes a high corrugated tunneling distribution

Fig. 1.1. Comparison of the resolution range of STM with that of other microscopes [1. 1]. [HM: High-resolution optical Microscope. PCM: Phase Contrast Microscope. (S)TEM: (Scanning) Transmission Electron Microscope. FIM: Field Ion Microscope. REM: Reflection Electron Microscope]
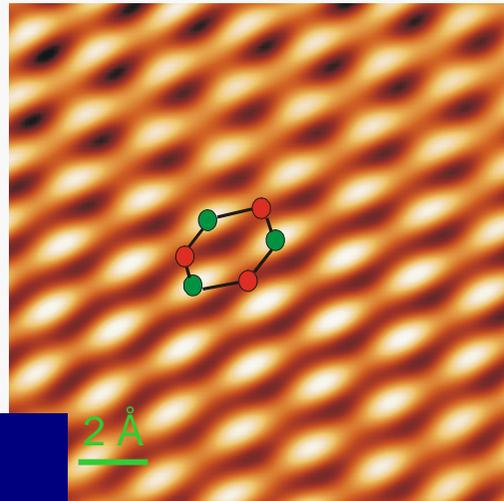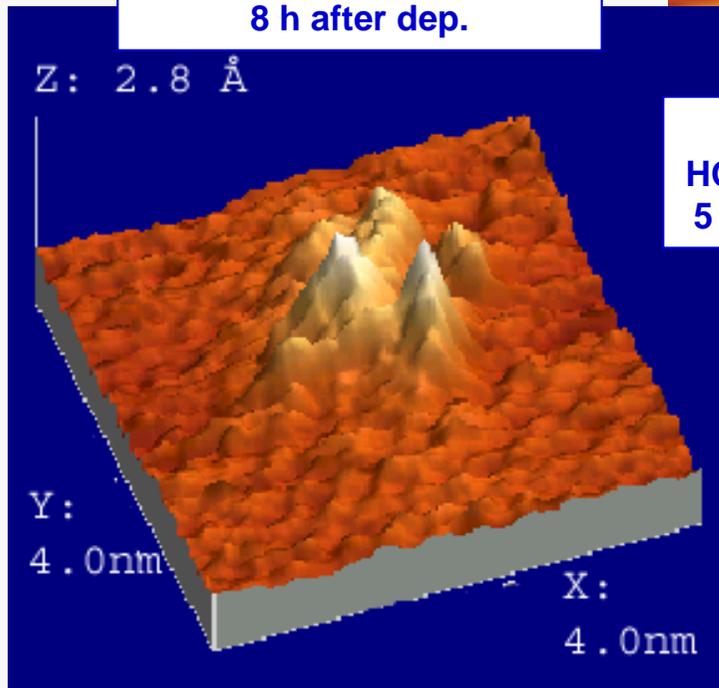
"Atomic" resolution achieved in STM

Atomic resolution in STM
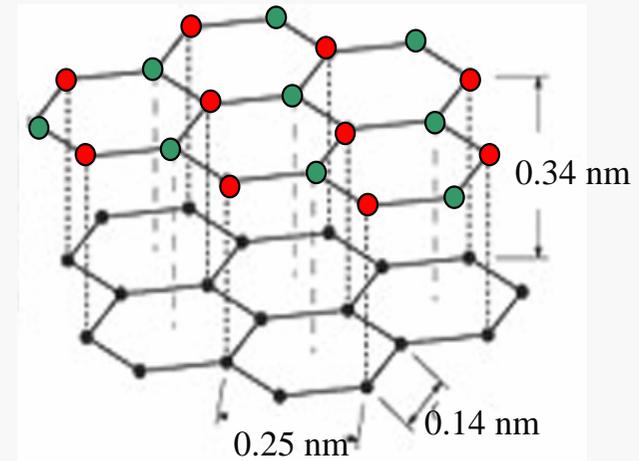
Highly Oriented Pyrolithic Graphite (HOPG) substrates well suited as test samples

A few examples

STM image - 3D view
Cs on HOPG (bias 0.5 V)
8 h after dep.

Z: 2.8 Å

Y: 4.0nm

X: 4.0nm

2 Å

STM image – plan view
HOPG substrate, $p < 10^{-8}$ mbar
5 nm x 5 nm scan (bias 0.5 V)

0.34 nm

0.14 nm

0.25 nm

Surface electron-related features can be easily observed
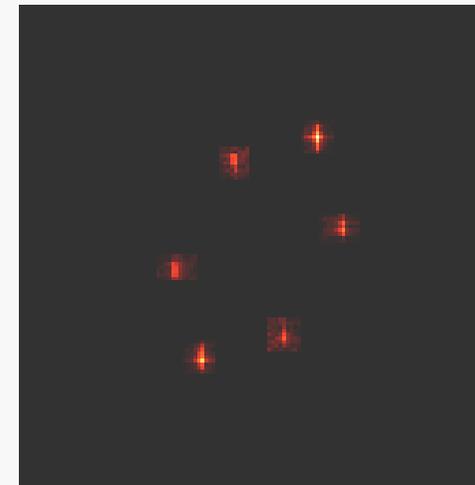
2D-FFT

Bias polarity-related contrast mechanisms

(a)

W_{vacuum}

In state

W_c

$W_F + eV$
W_v
eV

P state

W_F

InP(110) sample

occupied states

tip

(b)
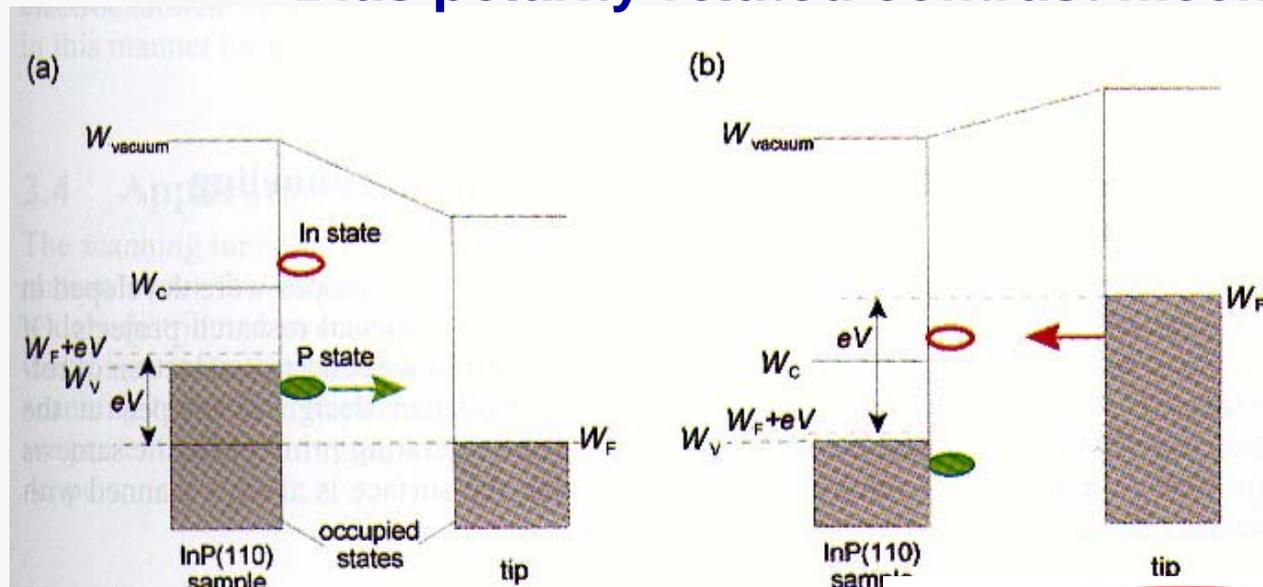
W_{vacuum}

W_F

eV

W_c

$W_F + eV$
W_v

InP(110) sample

tip

Figure 6: Schematic of the tunnelling process at (a) negative and (b) positive voltages applied to the InP(110) surface.

(a)

(b)

(c)

filled dangling bond

empty dangling bond

P
In
P
In

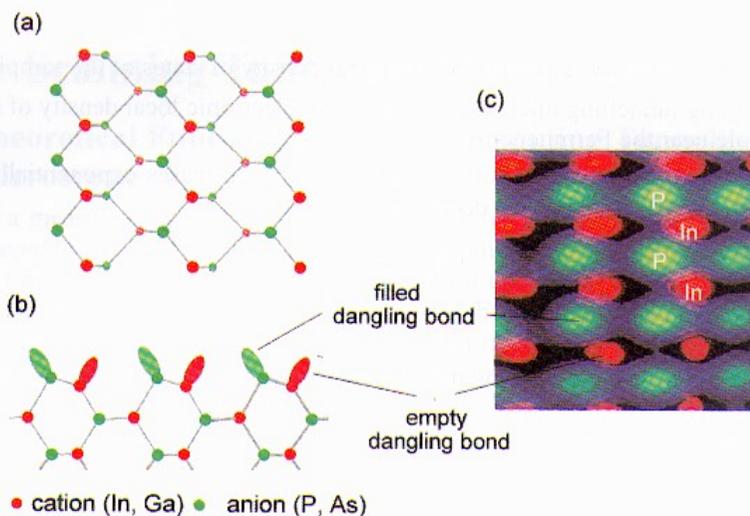● cation (In, Ga) ● anion (P, As)

Figure 7:
(a) Schematic top view and
(b) side view of the (110) surfaces of III-V compound semiconductors.
(c) Superposition of two scanning tunnelling microscope images measured at positive (red) and negative (green) voltage. The density of state maxima correspond to the surface states at the In and P atoms, respectively.

In the special case of the InP(110) surface, the occupied surface state is spatially located above the P atoms, whereas the empty state is bound to the In atoms (Figure 7a,b). The P and In atoms are alternately arranged in zigzag rows. At negative sample voltages, the scanning tunnelling microscope probes the occupied states located at the P sublattice, whose electrons tunnel into the empty states of the tunnelling tip (Figure 6a). Conversely, only the empty surface states at the In sublattice are probed at positive voltages applied to the sample (Figure 6b) [6] – [8]. If the voltage polarity is changed every scan line, i.e. the occupied and the empty states are probed each alternating scan line, the two resulting images can be superimposed and the zigzag rows of alternating "In" and "P" atoms become visible (Figure 7c).

Apart from the spatial distribution of the density of states, its energy dependence is also of interest, and it should be possible to determine this dependence from current-voltage characteristics using Eq. (5) In order to do so, however, information is required about the transmission coefficient, which turns out to be a great obstacle even if approximations [9] are used. Therefore, in most cases, an experimentally viable approach is used, in which the density of states is approximated as follows [10], [11]:

$$\rho_{sample}(eV) \approx (dI/dV)/(I/V) \qquad (6)$$

It is thus possible to experimentally measure the density of states as a function of the energy relative to the Fermi level.

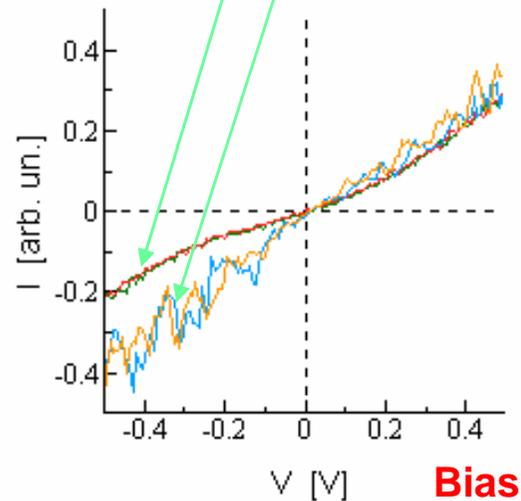Contrast mechanisms related to bias polarity

STM spectroscopy
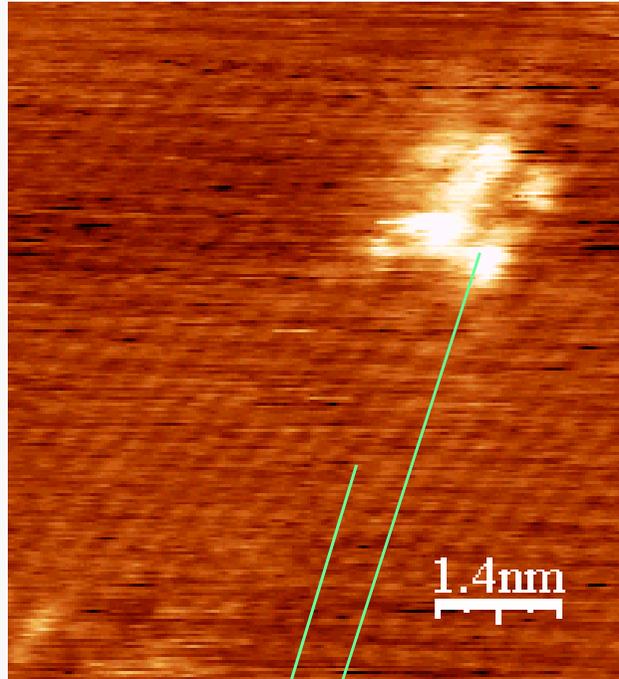
I-V curves can be acquired at different positions

STM image - plan view Cs on HOPG (bias 0.5 V) 8 h after dep.

Tunneling current (conversion factor 10^8)

Bias

Typical STM I-V curvesof different regions (covered/uncovered)

Possibility to discriminate "conductivity" of small-sized samples with an excellent space resolution

In the special case of the InP(110) surface, the occupied surface state is spatially located above the P atoms, whereas the empty state is bound to the In atoms (Figure 7a,b). The P and In atoms are alternately arranged in zigzag rows. At negative sample voltages, the scanning tunnelling microscope probes the occupied states located at the P sublattice, whose electrons tunnel into the empty states of the tunnelling tip (Figure 6a). Conversely, only the empty surface states at the In sublattice are probed at positive voltages applied to the sample (Figure 6b) [6] – [8]. If the voltage polarity is changed every scan line, i.e. the occupied and the empty states are probed each alternating scan line, the two resulting images can be superimposed and the zigzag rows of alternating "In" and "P" atoms become visible (Figure 7c).

Apart from the spatial distribution of the density of states, its energy dependence is also of interest, and it should be possible to determine this dependence from current-voltage characteristics using Eq. (5) In order to do so, however, information is required about the transmission coefficient, which turns out to be a great obstacle even if approximations [9] are used. Therefore, in most cases, an experimentally viable approach is used, in which the density of states is approximated as follows [10], [11]:

$$\rho_{sample}(eV) \approx (dI/dV)/(I/V) \tag{6}$$

"Spettroscopia" STM

It is thus possible to experimentally measure the density of states as a function of the energy relative to the Fermi level.

Fig. 3.1. The current versus voltage curve has a kink in it when the inelastic electron tunneling channel opens up. This kink becomes a step in the first derivative and a peak in the second derivative

filled dangling bond

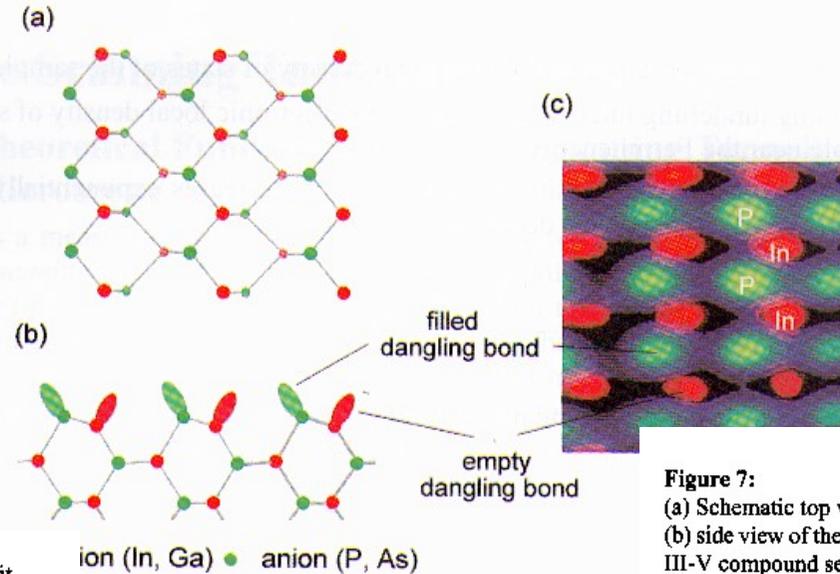empty dangling bond

cation (In, Ga) ● anion (P, As)

Figure 7:
(a) Schematic top view and
(b) side view of the (110) surfaces of III-V compound semiconductors.
(c) Superposition of two scanning tunnelling microscope images measured at positive (red) and negative (green) voltage. The density of state maxima correspond to the surface states at the In and P atoms, respectively.
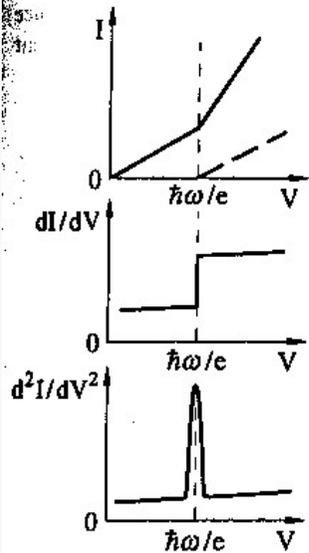

Figure 11: Phosphorus vacancies on
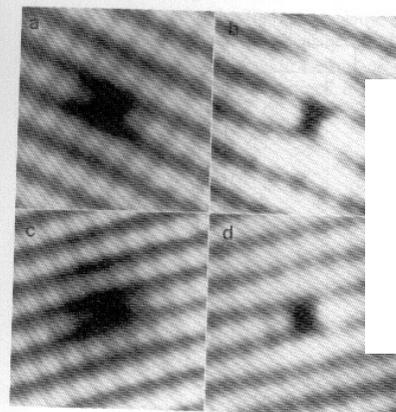(a) p- and
(b) n-doped GaP(110) and
(c) p- and
(d) n-doped InP(110). On the left, two positively charged vacancies are shown, whereas on the right they are negatively charged.

Figure 12: Schematic of the electron population of the defect energy level on p- and n-doped InP(110) and GaP(110) surfaces. On the left the vacancy is positively and on the right negatively charged.
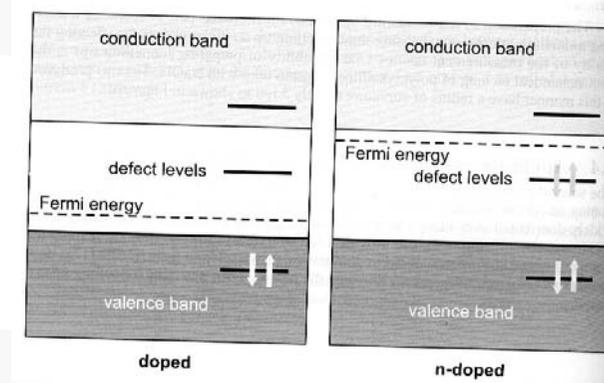
2. Scanning force microscopy (AFM and relatives)

STM	AFM	SNOM
Scanning Tunneling Microscope (STM)	Atomic Force Microscope (AFM)	Scanning Near-field Optical Microscope (SNOM)
Electron tunneling	**Force microscopy**	**Optical near-field**
	Locally probed quantity	
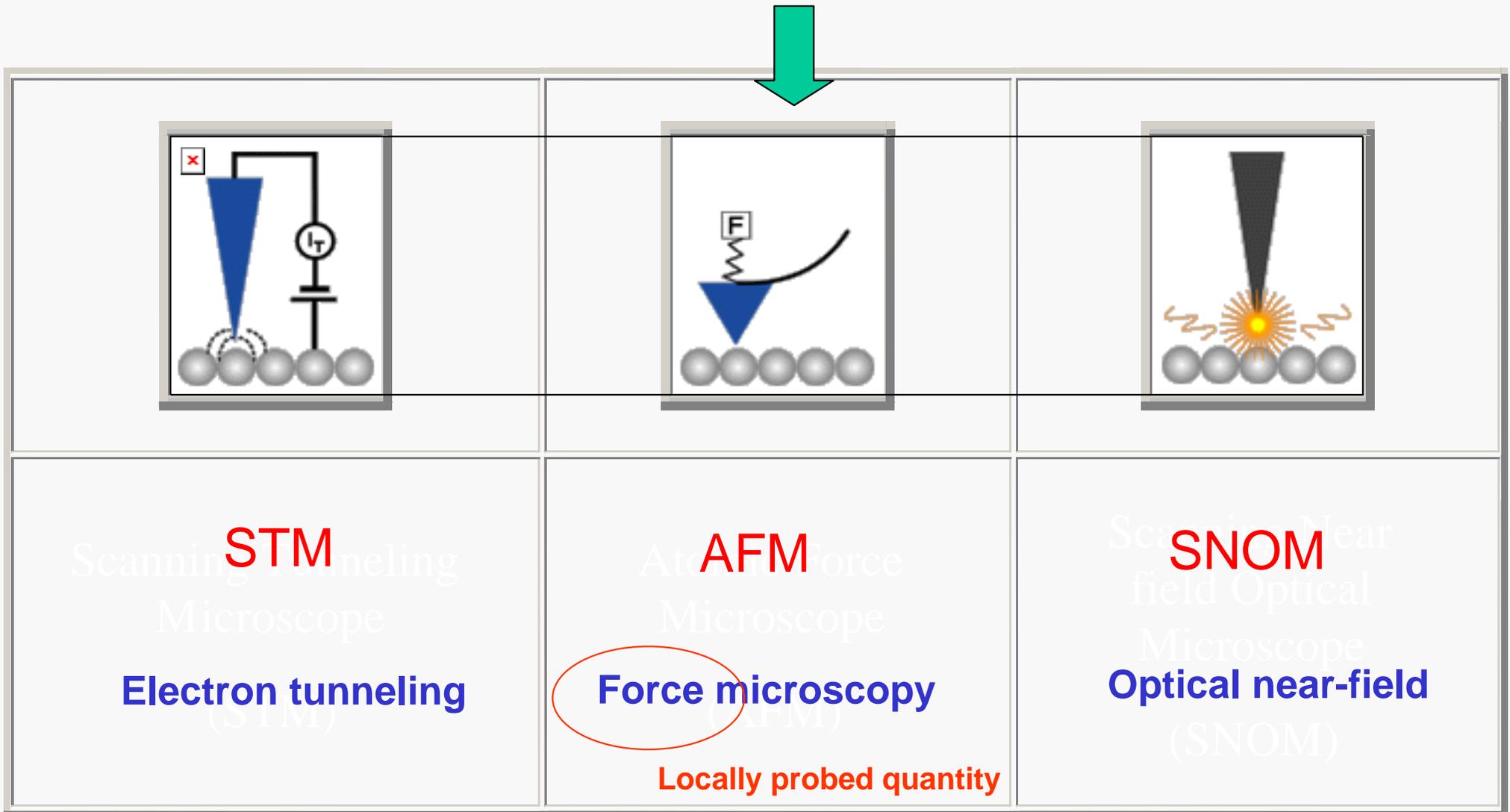
AFM is probably the most straightforward (and easy to understand/interpret) probe microscopy

Cantilevers for the AFM

Fig. 5.2a-d. Fabrication of thin-film microcantilevers. (a) A thin film of SiO_2 or Si_3N_4 is formed on the surface of a (100) Si wafer and patte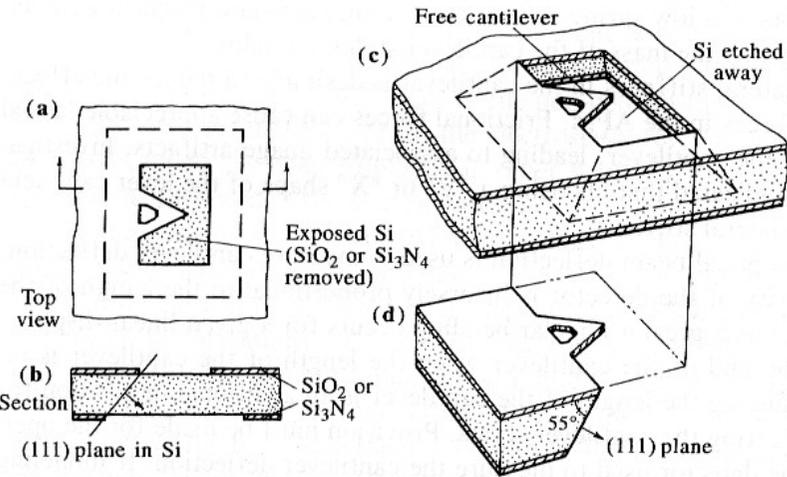rned to define the shape of the cantilever and to create openings on the top and bottom of the wafer. (b) The windows are aligned along (111) planes. (c) Anisotropic etching of the exposed Si with KOH undercuts the cantilever and self-terminates at the (111) planes as shown. (d) A small Si chip is cut from the wafer to serve as a pedestal for mounting the cantilever in the AFM [5.4]
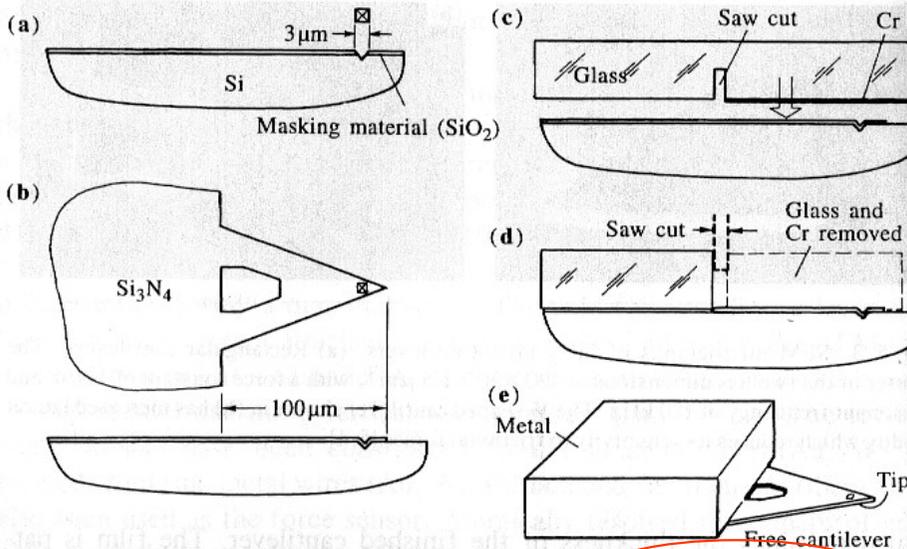
Fig. 5.4a-e. Fabrication of Si_3N_4 microcantilevers with integrated pyramidal tips. (a) to (e) illustrate the steps in the fabrication process, see text [5.4]

Advanced microfabrication tools needed to obtain suitable probes
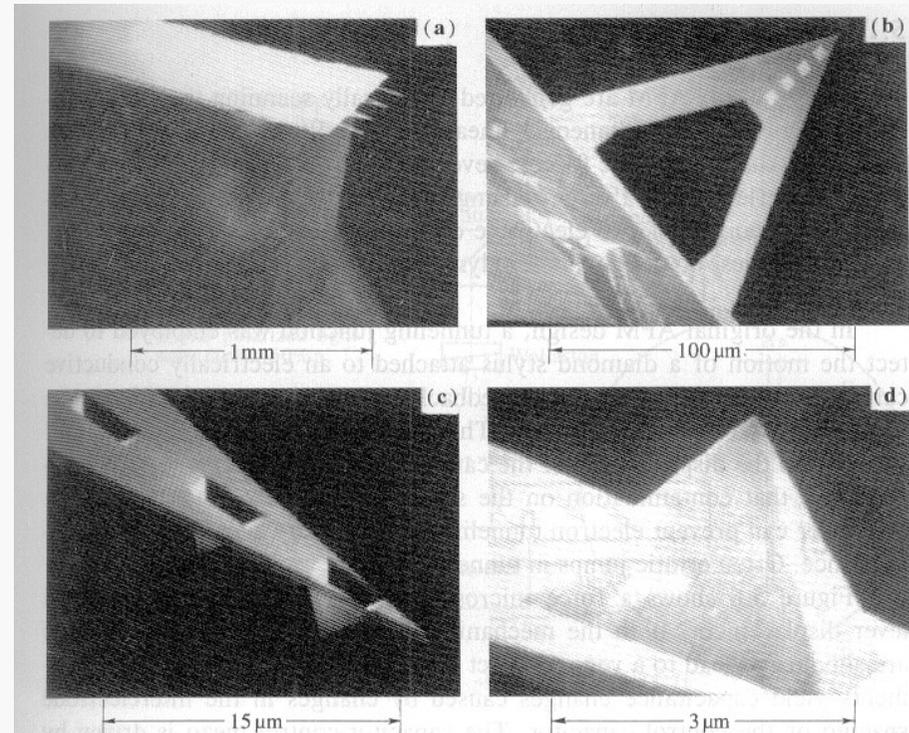
Fig. 5.5a-d. SEM micrographs of Si_3N_4 cantilevers with integrated pyramidal tips. (a) The Si_3N_4 film is attached to the surface of a glass block with dimensions of $2 \times 3 \times 0.7$ mm^3. Four cantilevers protrude from the edge of the block. (b) Four pyramidal tips can be seen at the end of this V-shaped cantilever. (c) The pyramidal tips are hollow when viewed from the back side. (d) Each tip has very smooth sidewalls, and the tip appears to terminate virtually at a point, with less than 30 nm radius [5.4]

Examples of commercial cantilevers

Microlevers™
GENERAL PURPOSE CANTILEVERS

ThermoMicroscopes Microlevers are ideal for all contact imaging modes, force modulation microscopy, and liquid operation. The range in force constants enable users to image soft samples in contact as well as high load force vs. distance spectroscopy.

FEATURES:

- Compatible with all major AFM brands.
- Typical radius of curvature: sharpened tips: < 20 nm., unsharpened tips: < 50 nm.
- Available with gold coating for high reflectivity.
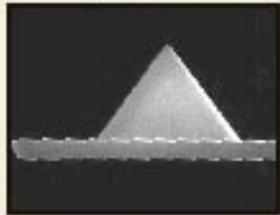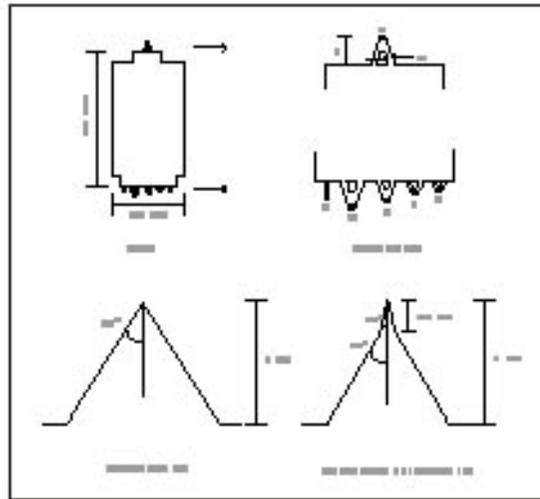- Recessed corners for easy sample approach.
- The widest range of spring constants commercially available on a single chip.

Typical Mechanical Characteristics

Cantilever type	A - triangular	B - rectangular	C - triangular	D - triangular	E - triangular	F - triangular
Standard mode of operation	Contact					
Cantilever length	180 μm	200 μm	320 μm	220 μm	140 μm	85 μm
Cantilever width	18 μm	20 μm	22 μm	22 μm	18 μm	18 μm
Cantilever thickness	0.6 μm	0.6 μm	0.6 μm	0.6 μm	0.6 μm	0.6 μm
Force Constant	0.05 N/m	0.02 N/m	0.01 N/m	0.03 N/m	0.10 N/m	0.50 N/m
Resonant Frequency	22 kHz	15 kHz	7 kHz	15 kHz	38 kHz	120 kHz

Ordering Information

Microlevers				
	Sharpened		Unsharpened	
Quantity	Gold coated*	Uncoated	Gold coated*	Uncoated
Half wafer - (250 chips)	MSCT-AUHW	MSCT-NOHW	MLCT-AUHW	MLCT-NOHW
Unmounted - (25 chips)	MSCT-AUNM	MSCT-NONM	MLCT-AUNM	MLCT-NONM
Mounted - (25 chips)	MSCT-AUMT-A	MSCT-NOMT-A	MLCT-AUMT-A	MLCT-NOMT-A
Mounted - (25 chips)	MSCT-AUMT-BF	MSCT-NOMT-BF	MLCT-AUMT-BF	MLCT-NOMT-BF

* Not for use with AutoProbe M5 systems

To Place an order, contact:
ThermoMicroscopes
1171 Borregas Avenue, Sunnyvale, CA 94089
Tel: (408) 747-1600 Fax: (408) 747-1601
E-mail: info@thermomicro.com
Web: www.thermomicro.com
Online Ordering: www.spmprobes.com

THERMOMICROSCOPES
Park Scientific Instruments TOPOMETRIX

Many different cantilevers are commercially available

They are different for:
- Dimensions and shape:
- Elastic constant (materials and design);
- Tip coating (conductive, super-hard, etc.)

Cantilever choice depends for instance on:
- Operation mode (contact/non contact);
- Quantities to be probed (e.g., if an electric field is needed, a conductive tip has to be used);
- Possible material manipulation (e.g., nanoindentation requires super-hard tips)

Basics of tip/sample interaction

When the tip is approached to the sample (at sub-nm distance!), forces depend roughly on van der Waals interaction between the apical tip atoms and the surface

At "large" distance forces are weakly attractive, at "short" distance they are repulsive

Surface topography (height variations) can be sensed by monitoring the force, i.e., the **cantilever deflection**
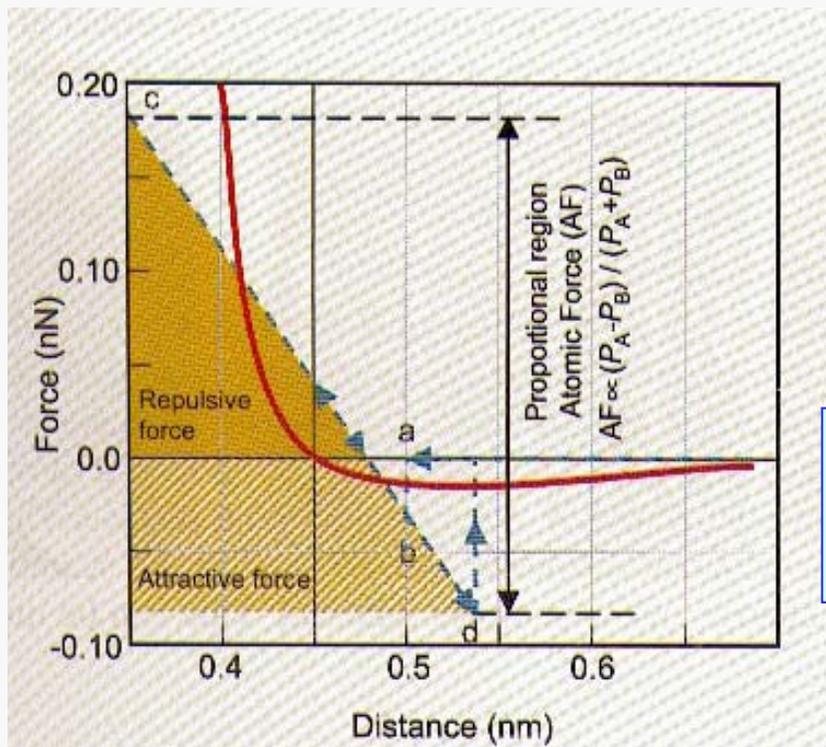
When tip/sample distance is kept in the repulsive region, **contact operating mode** is achieved

When tip/sample distance is kept *(mostly)* in the attractive region, **non-contact operating mode** is achieved

3.2 The Operation Principle of Scanning Force Microscope

The main electronic components of the SFM are the same as for the STM, only the topography of the scanned surface is reconstructed by analysing the deflection of the tip at the end of a spring. Today, the interferometrical and optical lever method dominate commercial SFM apparatus. The most common method for detecting the deflection of cantilever is by measuring the position of a reflected laser-beam on a photosensitive detector. The principle of this optical lever method is presented in Figure 18 a. Without

cantilever displacement both quadrants of the photodiode (A and B) have the same irradiation $P_A = P_B = P/2$ (P represents the total light intensity). The change of the irradiated area in the quadrants A and B is a linear function of the displacement

$$\delta \propto \Delta d = 2\sin(\Theta) \cdot S_2 = 2\Theta \cdot S_2 = 3S_2 \cdot \delta/L \qquad (10)$$

For small angles $\sin(\Theta) \approx \Theta$ and Θ may be evaluated from the relation $\Theta = 3\delta/2L$ (Figure 18b). For P_A and P_B one would get approximately $P_A = P/2 \cdot (d + \Delta d)/2$ and $P_B = P/2 \cdot (d - \Delta d)/2$. Using the simple difference between P_A and P_B would lead to

$\Delta P = P \cdot 3S\delta/(Ld)$ but in this case one cannot distinguish between the displacement δ of the cantilever and the variation in the laser power P. Hence the normalised difference is used, which is only dependent of δ:
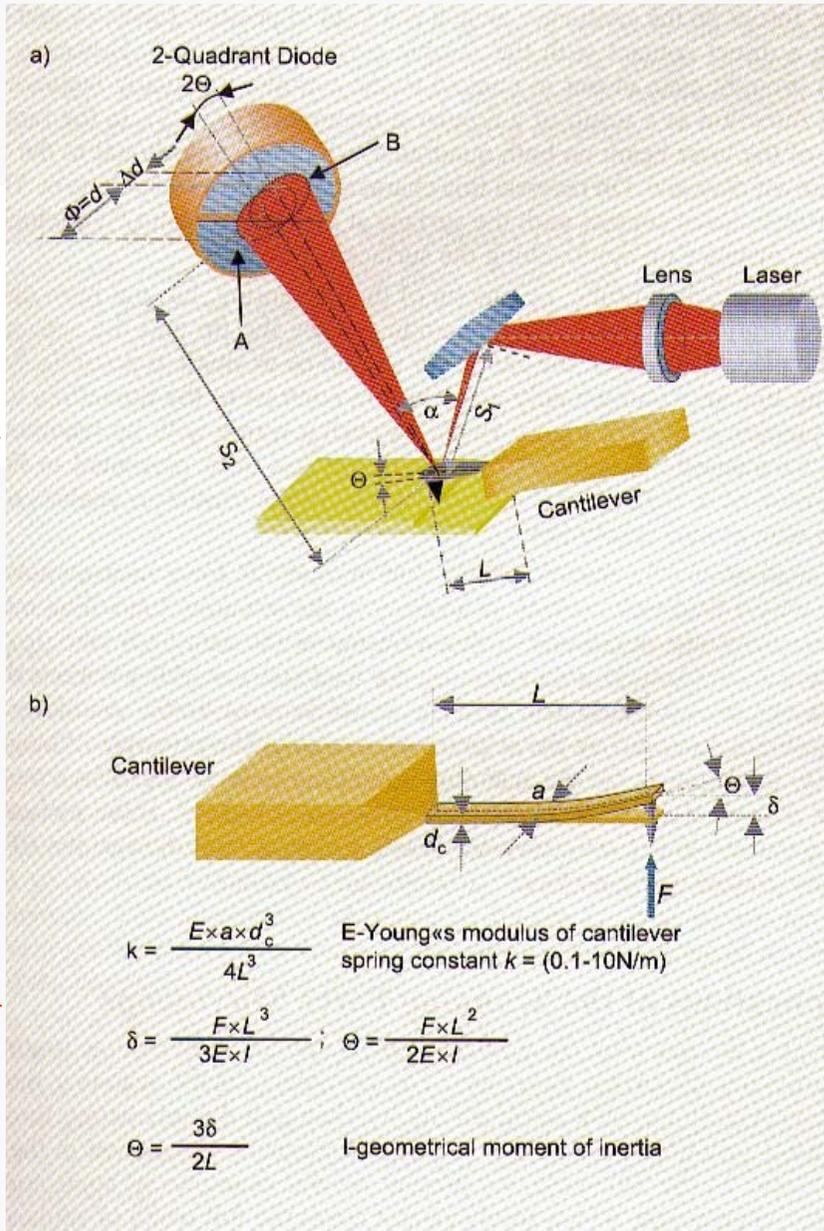
$$\frac{P_A - P_B}{P_A + P_B} = \delta \cdot \frac{3S_2}{Ld} \qquad (11)$$

The "lever amplification" $\Delta d/\delta = 3S_2/L$ is about a factor of one thousand. On the basis of this kind of technique one is able to detect changes in the postion of a cantilever of the order of 0.01 nm.

For large distances between the tip and the sample the bending of the cantilever by attractive forces is negligible. After the cantilever is brought closer to the surface of the sample (point "a" Figure 18c) the van der Waals forces induce a strong deflection of the cantilever and, simultaneously, the cantilever is moving towards the surface. This increases the forces on the cantilever, which is a kind of positive feedback and brings the cantilever to a direct contact with the sample surface (point "b"). However, when the cantilever is brought even closer in contact to the sample, it actually begins to bend in the opposite direction as a result of a repulsive interaction ("b-c"). In the range ("b-c") the position of the laser beam on both quadrants, which is proportional to the force, is a linear function of distance. On reversal this characteristic shows a hysteresis. This means that the cantilever loses contact with the surface at a distance (point "d") which is much larger than the distance on approaching the surface (point "a").

Up to now, the actual probe, i.e. the tip of the leaf spring, has not been discussed in detail. Its preparation is particularly demanding since the tip and the sensitive spring should be one piece. Moreover, the cantilever should be as small as possible. Nowadays, such scanning tips are commercially available (in contrast to the tunnelling tips, which you should prepare yourself). Figure 19 shows such a spring with tip (cantilever) made of Si. The characteristic parameters of a cantilever has been presented in Figure 18b. The spring constant $k = Ead_C^2/4L^3 \approx 0.1 - 10$ N/m of the cantilever enables topographical analysis with atomic resolution.

For the realisation of a scanning force microscope, the force measurement must be supplemented by a feedback control, in analogy to the scanning tunnelling microscope. The controller keeps the amplitude of the vibration of the cantilever (the tip), and thus also the distance, constant. During scanning the feedback controller retracts the sample with the scanner of a piezoelectric ceramic or shifts towards the cantilever until the vibration amplitude has reached the setpoint value again. The principle of height regulation is exactly the same as for the scanning tunnelling microscope. *The scanning force micrographs thus show areas of constant effective force constant.* If the surface is chemically homogeneous and if only van der Waals forces act on the tip, the SFM image shows the *topography of the surface.*

Contact mode of operation

$$k = \frac{E \times a \times d_c^3}{4L^3}$$

E-Young«s modulus of cantilever
spring constant $k = (0.1-10$N/m$)$

$$\delta = \frac{F \times L^3}{3E \times I} \quad ; \quad \Theta = \frac{F \times L^2}{2E \times I}$$

$$\Theta = \frac{3\delta}{2L}$$

I-geometrical moment of inertia

Figure 18: The amplification of the cantilever motion through the optical lever arm method.
(a) Optical laser path in the standard AFM set-up.
(b) Cantilever beam in bending.
(c) Cantilever force as a function of the distance tip – sample distance.

An optical lever method is used to detect the cantilever deflection

Scanning Force Microscopy II

3.1 Theoretical Principles of the Scanning Force Microscope

As already mentioned above, van der Waals forces lead to an attractive interaction between the tip on the spring and the sample surface. Figure 15 shows schematically the van der Waals potential between two atoms. The potential can be described in a simpler classical picture as the interaction potential between the time dependent dipole moments of the two atoms. Although the centres of gravity of the electronic charge density and the charge of nucleus are exactly overlapping on a time average, the separation of the centres of gravity is spatially fluctuating in every moment. This produces statistical fluctuations of the atoms' dipole moments. The dipole moment of an atom can again induce a dipole moment in the neighbouring atom and the induced dipole moment acts back on the first atom. This creates a dipole-dipole interaction on basis of the fluctuating dipole moments. This interaction decreases with d^{-6} in the case of small distances d (Lenard-Jones potential). At larger distances, the interaction potential decreases more rapidly (d^{-7}). This arises from the fact that the interaction between dipole moments occurs through the exchange of virtual photons. If the transit time of the virtual photon between atoms 1 and 2 is longer than the typical fluctuation time of the instantaneous dipole moment, the virtual photon weakens the interaction. This range of the van der Waals interaction is therefore called retarded, whereas that at short distances is unretarded.
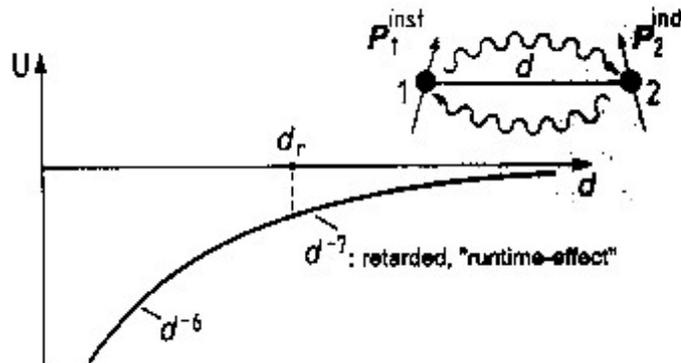
The scanning force microscope is not based on the interaction of individual atoms only. Both the sample and the tip are large in comparison to the distance. In order obtain their interaction, all forces between the atoms of both bodies need to be integrated. The result of this is known for simple bodies and geometries. In all cases, the summation leads to a weaker decrease of the interaction. A single atom at distance d relative to a half-space leads to an interaction potential of

$$U = -\frac{C\pi\rho}{6} \cdot \frac{1}{d^3} \tag{7}$$

where C is the interaction constant of the van der Waals potential and Δ the density of the solid. C is basically determined by the electronic polarizabilities of the atoms in the half-space and of the single atom. If one has two spheres with radii R_1 and R_2 at distance d (distance between sphere surfaces) one obtains an interaction potential of

$$U = -\frac{AR_1R_2}{6(R_1 + R_2)} \cdot \frac{1}{d} \tag{8}$$

where A is the so-called Hamaker constant. It is materials specific and essentially contains the densities of the two bodies and the interaction constant C of the van der Waals potential. If a sphere with radius R has a distance d from a half-space, an interaction potential of

$$U = -\frac{AR}{6} \cdot \frac{1}{d} \tag{9}$$

is obtained from Eq. (8). This case describes the geometry in a scanning force microscope best and is most widely used. The distance dependence of the van der Waals potential thus obtained is used analogously to the distance dependence of the tunnel current in a scanning tunnelling microscope to achieve a high resolution of the scanning force microscope. However, since the distance dependence is much weaker, the sensitivity of the scanning force microscope is lower.

Figure 15: The van der Waals potential U between two atoms. d_r is the critical distance above which the transit time effects weaken the interaction [23].

Contact mode is suitable for rather rigid surfaces

In the contact mode of operation, mechanical interaction leads to tip displacement, i.e., to cantilever deflection related to topography changes

As in STM (constant gap), typical operation foresees a **feedback** system, acting on the Z direction of the piezoscanner, which keeps constant the cantilever deflection during the scan

The "error signal" of the feedback system provides a **topography map (with a calibrated sub-nm space resolution)**

The dynamic operation method of a scanning force microscope has proved to be particularly useful. In this method the nominal force constant of the van der Waals potential, i.e. the second derivative of the potential, is exploited. This can be measured by using a vibrating tip (Figure 16). If a tip vibrates at distance d, which is outside the interaction range of the van der Waals potential, then the vibration frequency and the amplitude are only determined by the spring constant k of the spring. This corresponds to a harmonic potential. When the tip comes into the interaction range of the van der Waals potential, the harmonic potential and the interaction potential are superimposed thus changing the vibration frequency and the amplitude of the spring.

This is described by modifying the spring constant k of the spring by an additional contribution f of the van der Waals potential. As a consequence, the vibration frequency is shifted to lower frequencies as shown in Figure 17. ω_0 is the resonance frequency without interaction and $\Delta\omega$ the frequency shift to lower values. If an excitation frequency of the tip of $\omega_m > \omega_0$ is selected and kept constant, the amplitude of the vibration decreases as the tip approaches the sample, since the interaction becomes increasingly stronger. Thus, the vibration amplitude also becomes a measure for the distance of the tip from the sample surface. If a spring with low damping Q^{-1} is selected, the resonance curve is steep and the ratio of the amplitude change for a given frequency shift becomes large.

In practice, small amplitudes (approx. 1 nm) in comparison to distance d are used to ensure the linearity of the amplitude signal. With a given measurement accuracy of 1 %, however, this means that the assembly must measure deflection changes of 0.01 nm, which is achieved most simply by a laser interferometer or optical lever method.
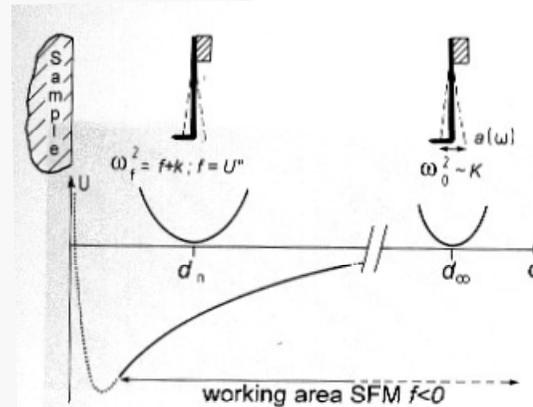

$\omega_f^2 = f+k; f = U''$

$\omega_0^2 \sim K$

$a(\omega)$

working area SFM $f<0$

Figure 16: Schematic representation of the effect of the van der Waals interaction potential on the vibration frequency of the spring with tip. As the tip approaches the surface, the resonance frequency of the leaf spring is shifted. (from [23]).
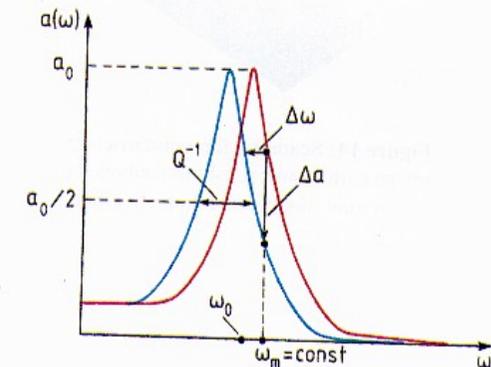

Figure 17: Resonance curves of the tip without and with interaction with a van der Waals potential. The interaction leads to a shift $\Delta\omega$ of the resonance frequency with the consequence that the tip excited with the frequency ω_m has a vibration amplitude $a(\omega)$ attenuated by Δa [23].

In **non-contact (tapping) mode**, the tip/sample distance is continuously modulated thanks to a vibrating tip

Tip vibration is typically achieved by using a piezoelectric transducer fed by an oscillating voltage and mechanically coupled to the cantilver

Oscillation frequency is typically set around the mechanical resonance frequency of the system (cantilever+tip), i.e., hundreds of kHz

The vibration reflects in an oscillation of the position-sensitive detector (multiquadrant diode) and amplitude is monitored

Tip/sample interaction leads to a **damping** (and **phase shift**) of the recorded oscillation when the distance gets small

Suitably conditioned electronic signals are sent into the feedback system in order to stabilize the distance and to derive the topography map

Non-contact modes suitable for "soft" surfaces

**No sample preparation is needed!!**

A very few examples of AFM images
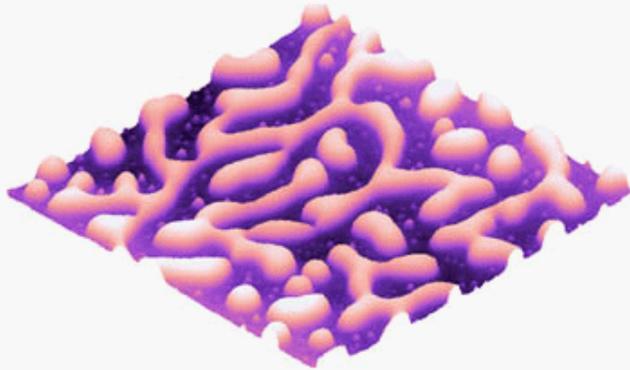
TappingMode AFM image of poly(styrene) and poly(methyl methacrylate) blend polymer film. The film was spin-cast on mica substrate from chloroform solution. The surface structure is resulted from the spinodal decomposition. The islands consist of a PMMS-rich phase while the surface matrix composes of a PS-rich phase. 3µm scan courtesy C. Ton-That, Robert Gordon University, U.K.

YBCO/YSZ/Ni
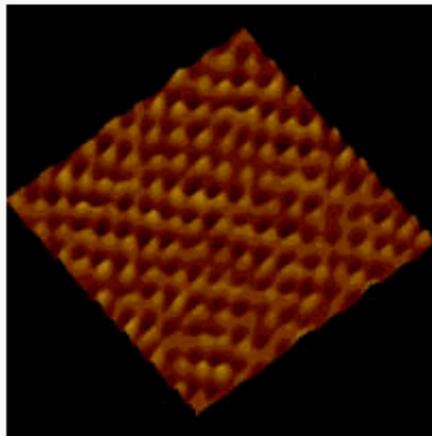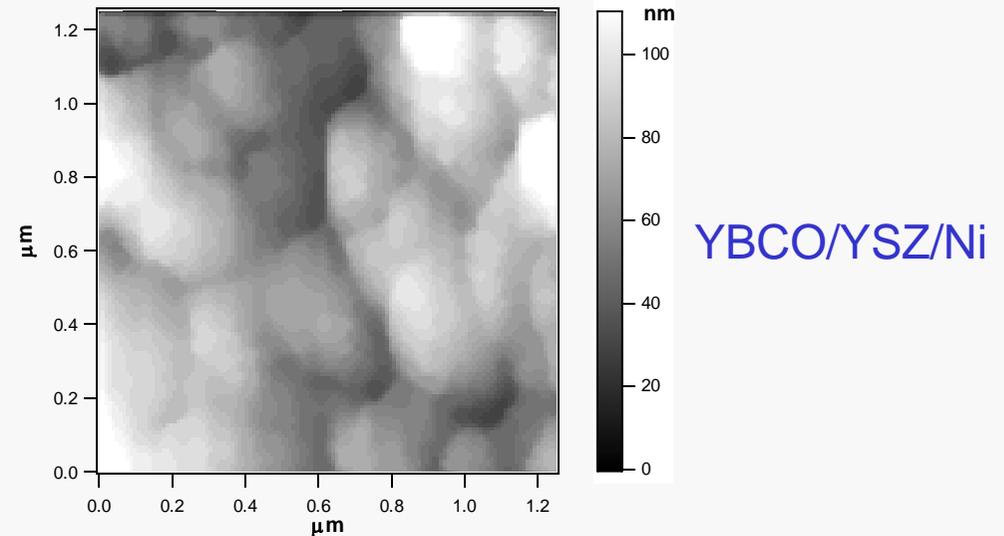
Atomic resolution image of the titanium oxide layer on top of a titanum substrate. Contact mode AFM in air, commercial silicon nitride cantalever. 5 nm scan courtesy P. Cacciafesta, University of Bristol, UK.
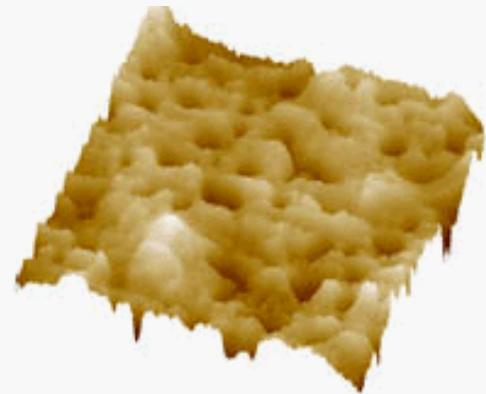
The sample is a strip of adhesive (3M Scotch tape) that has been peeled of a metal surface. The image shows small pits in the sticky surfaces of the adhesive. The image was acquired in TappingMode at frequency of 3 Hz and setpoint of 1.8 V. 2µm scan courtesy L. Scudiero, Washington State University, USA.

See http://www.veeco.com
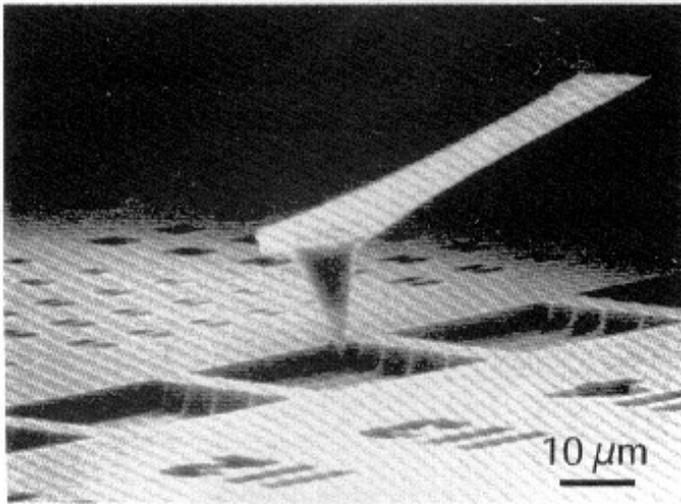
2.B. Force microscopies derived from AFM

Figure 19: Scanning electron micrograph of a cantilever made of Si. [24].

We have seen how AFM, based on the occurrence of tip/surface van der Waals forces, can map the local topography of the sample

No sample preparation is needed, and the topography map is derived in absolute terms

The achievable space resolution can reach the **atomic level**, even though most common instruments are capable of a slightly smaller resolution (in the nm range, depending also on the sample properties!)

The close vicinity between tip and surface realized in AFM opens the way for probing physical **quantities other** than the van der Waals interaction force

For instance, tribological and material quantities can be measured (e.g., friction, viscoelaticity, Young modulus, etc.)
With suitable tips (conductive, magnetic), static and quasi-static electromagnetic forces can be derived locally occurring at the sample surface

Lateral Force Microscopy (LFM, SFFM) I

Frictional force microscopy
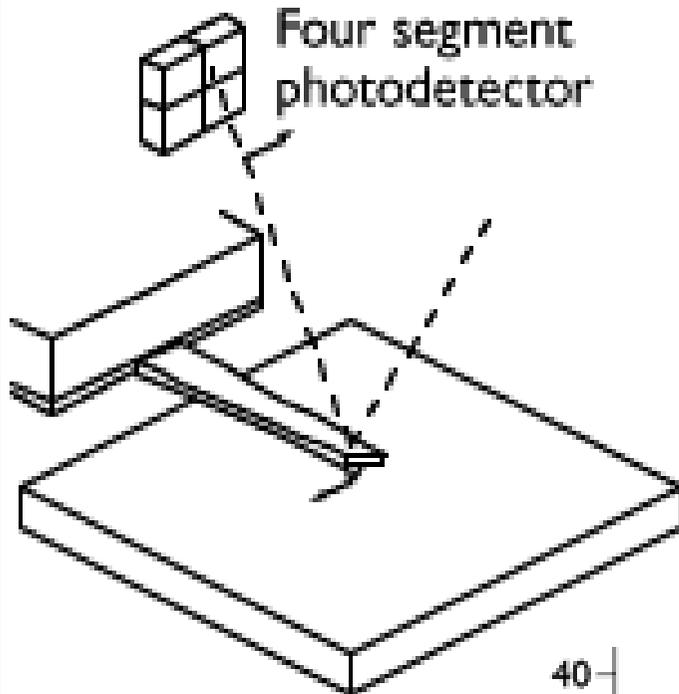
During the scan, the tip is continuously displaced with respect to the surface

Friction forces occur, resulting in a *twisting* of the cantilever

Cantilever twist can be recorded by a two-dimension position sensitive detector (i.e., a 4-quadrant photodetector)

Friction effects can be corrected by the topographical artifacts by comparing forward and backward scans

Forward scan

Hysteresis loop
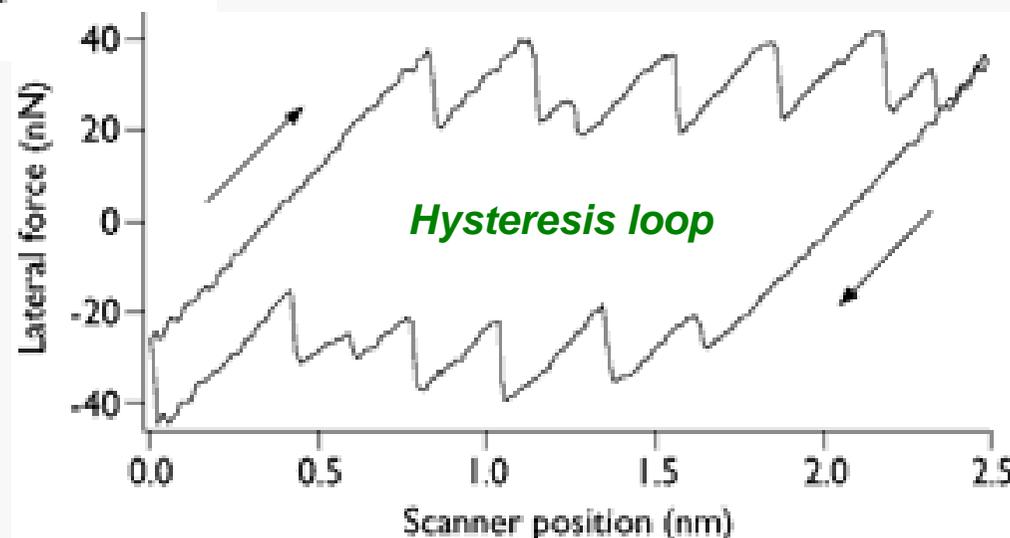
Backward scan

Microscopia a forza laterale (LFM, SFFM) II
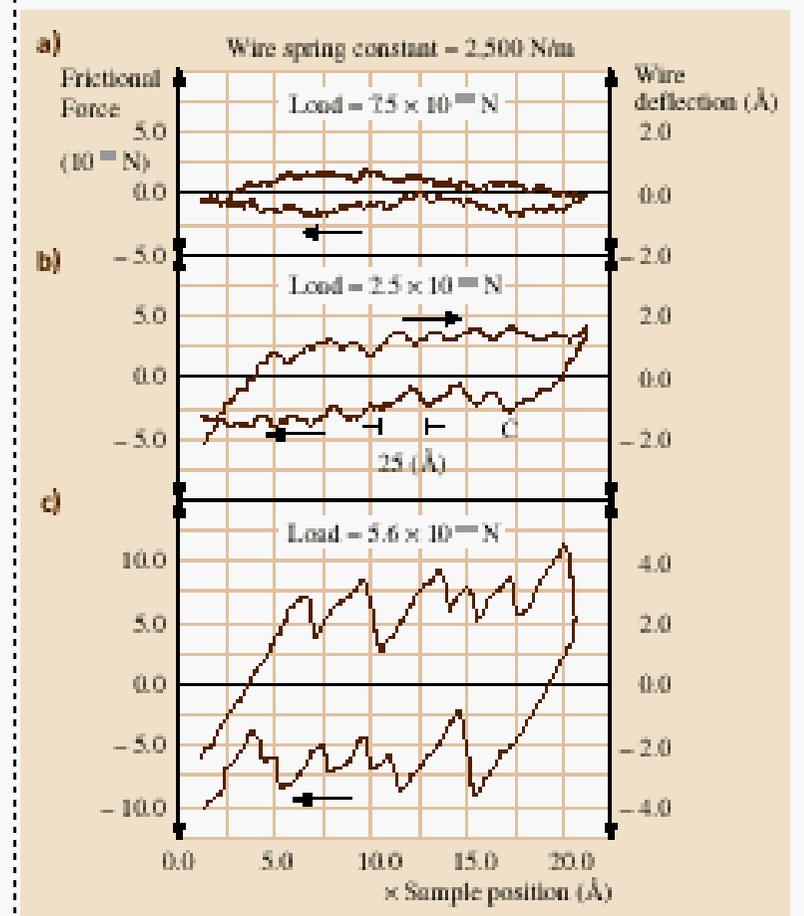
Fig. 20.15a–c Friction loops on graphite acquired with (a) $F_N = 7.5$ μN, (b) 24 μN and (c) 75 μN. (After [20.1])

Fig. 20.18 (a) Topography and (b) friction image of Si(111)7×7 measured with a PTFE coated Si-tip. (After [20.29])
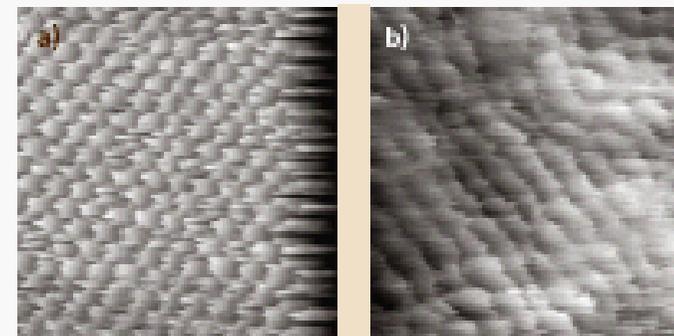
Fig. 20.19a,b Friction images of (a) Cu(111) and (b) Cu(100). Frame size: 3 nm. (After [20.34])

✓LFM/SFFM offers an additional contrast mechanism
✓Possibility to discriminate different materials at the atom level
✓Nanotribology investigations can be carried out

Da B. Bhushan, Handbook of nanotechnology (Springer, 2003)

Magnetic Force Microscopy (MFM)

3.3.2 Magnetic Scanning Force Microscopy (MFM)

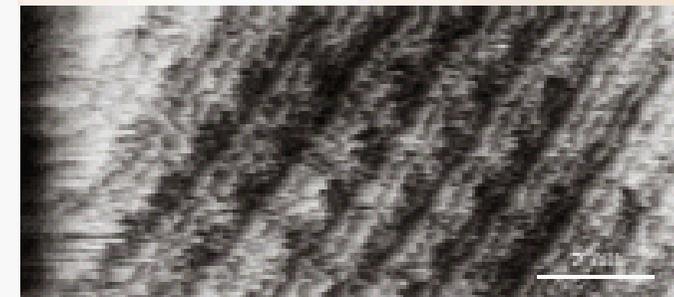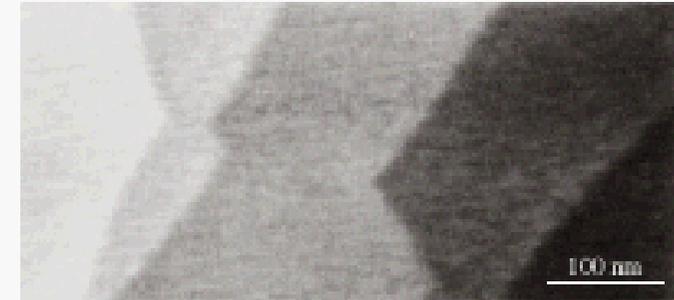If a magnetic tip is used in the scanning force microscope, magnetic structures can be imaged. Magnetic scanning force microscopy is of interest, in particular, for the investigation of magnetic storage media. In the most general case, the magnetic force between sample and tip is

$$F_{mag} = -\nabla \int_{tip} M_{tip} \cdot H_{sample}\, dV \qquad (13)$$

or

$$F_{mag} = (m_{tip} \nabla)B_{sample} \qquad (14)$$

where H_{sample} and B_{sample} are the magnetic stray field and the magnetic induction of the sample, respectively. M_{tip} and m_{tip} are the magnetisation and the magnetic moment of the tip, respectively. Since in most cases the exact magnetic structure of the tip is not known, a model tip magnetization must assumed. In the simplest case, the tip is a spherically structured magnetic single domain with the magnetisation M_{tip}. Of particular interest are the stray fields of magnetic storage media which consist of different domains. Since the important aspect in force microscopy is not the forces but the force gradient, a pronounced variation of the signal is found near the domain walls, but not inside a domain. This situation is sketched in Figure 21. The parameter of the two curves shown (solid and broken lines) is the ratio of the working distance d and the radius R of the magnetic domain of the tip.

Figure 22a shows an experimentally measured picture of four different oriented magnetic domains. Images **b** and **c** show the fine structure of a 180° domain. Alternating bright and dark contrasts can be seen. These contrast changes show that the domain wall consists of segments with different wall orientation. This example illustrates that magnetic SFM is well suited for imaging magnetic structures that are commonly used in today's' storage media.

$$F_{mag} = -\mathrm{grad}\left(-\int_{sample} dV M_{sample}\, H_{sample}\right)$$

Figure 21: Principle of magnetic scanning force microscopy. On the left, the tip-sample configuration is shown and on the right the force and nominal force constant as a function of distance for this configuration. Two domain walls exist at position 5 (after [23])

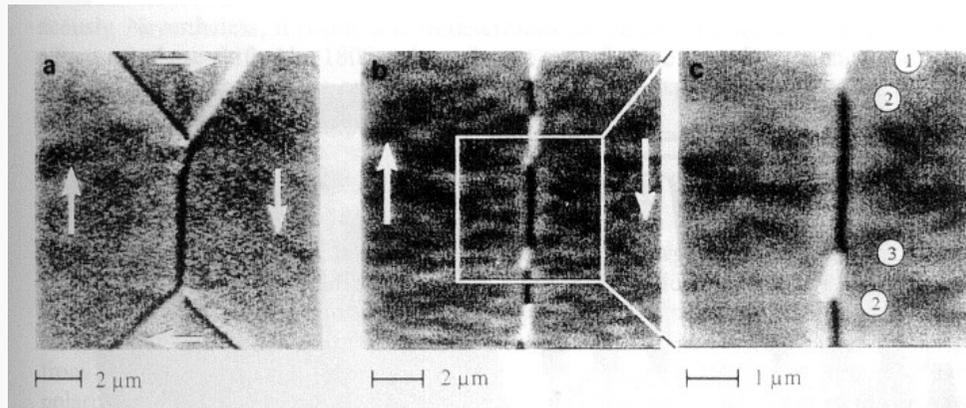**Figure 22:** Magnetic SFM image of magnetic domains.
(a) shows four domains of a Landau-Lifshitz structure in which the domain walls are the dark and bright lines.
(b) and (c) show the fine structure of a 180° domain wall. The domain wall consists of segments with different wall orientation. Arrows denote the domain orientation. (after [26]).
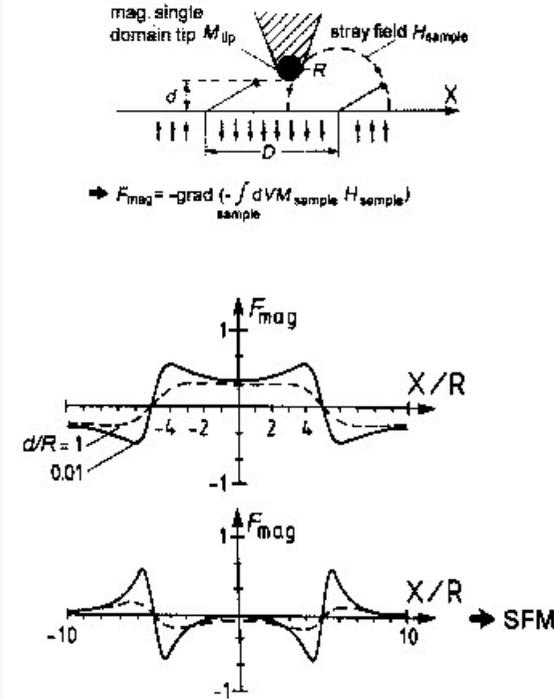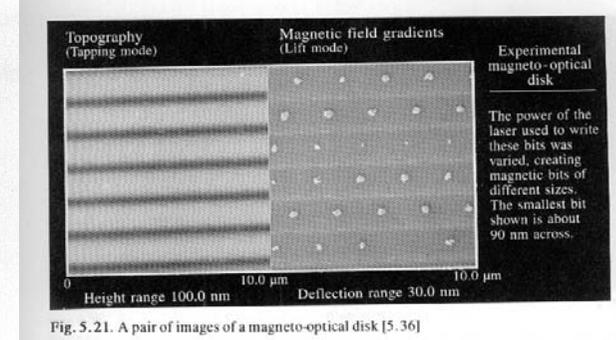

Fig. 5.21. A pair of images of a magneto-optical disk [5.36]

Electrostatic Force Microscopy (EFM)

3.3.3 Electrostatic Scanning Force Microscopy (EFM)

The scanning force microscope can also be used for electrostatic or Coulomb images. In this case, however, the tip must be insulated. A modern version of electric force microscopes uses for the determination of surface charge or surface potential a complicated lock-in and phase loops electronics. The essential modification with respect to the old apparatus is the so called two-pass technique (LiftMode). In this method each line must be scanned twice. On the basis of two line scans, in which the first represents the topography of the surface in a contact mode and the second is taken at a fixed distance relative to the surface (Figure 23), one can reconstruct precisely the distribution of the charge or the potential on the surface without topographical error. In Figure 24 an example case is given, which highlights the possibilities of this modern tool for microelectronics. An other example showing an image of a broken carbon nano tube is represented in Figure 25.

Figure 23 shows the effect of the charge when the tip comes into the region of the local surface charge. An attractive Coulomb interaction existss between these charges and the charge induced in the tip. The electrostatic force as a function of distance is given by

$$F_{el} = -\pi \varepsilon_0 U^2 \frac{r^2}{d^2} \tag{15}$$
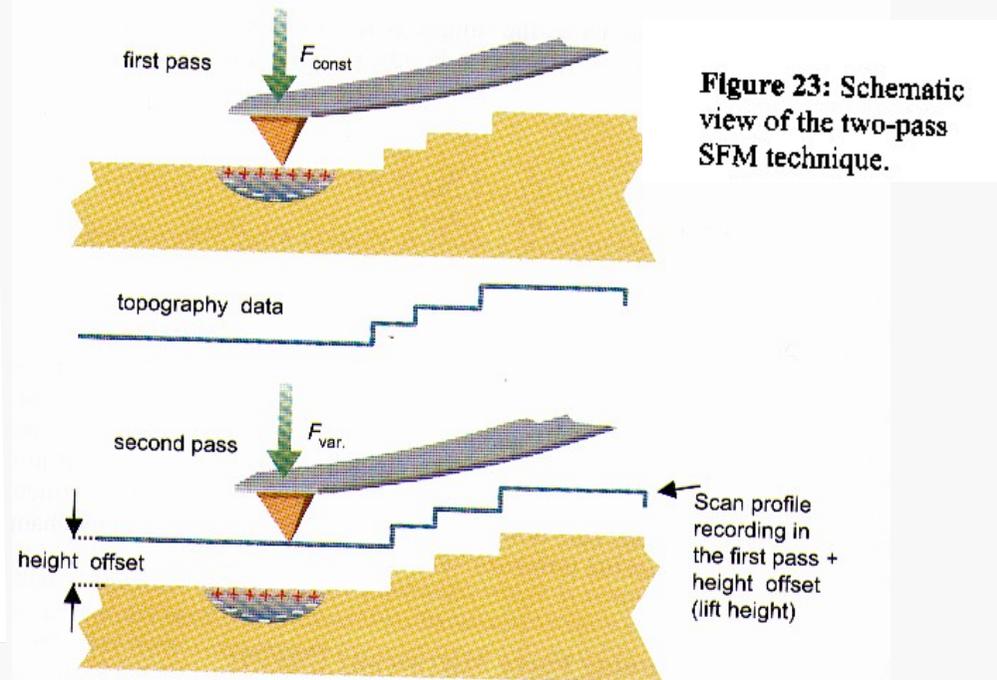
Figure 23: Schematic view of the two-pass SFM technique.
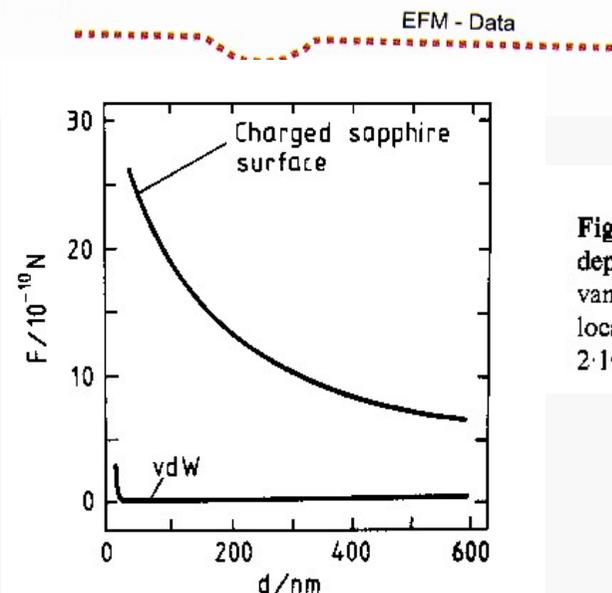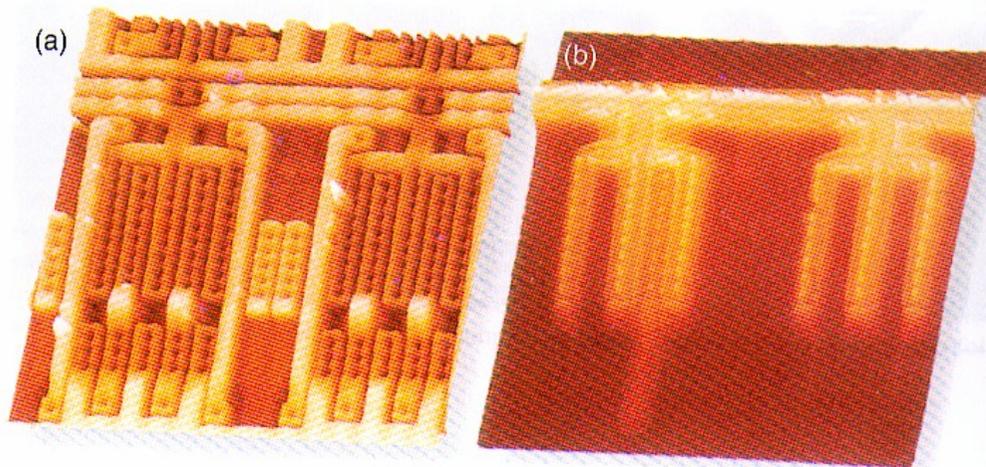
Figure 26: Comparison of the distance dependence of the electrical and van der Waals forces between a tip and a local electrical surface charge of $2 \cdot 10^{-16}$ C (after [23]).

3. Scanning Near Field Optical Microscopy (SNOM)

STM	AFM	SNOM
Scanning Tunneling Microscope (STM)	Atomic Force Microscope (AFM)	Scanning Near field Optical Microscope (SNOM)
Electron tunneling	**Force microscopy**	**Optical near-field**
		Locally probed quantity

*SNOM holds the **unique** ability to analyze optical properties with sub-diffraction space resolution*

SNOM probes (aperture-SNOM) I

Different configurations for SNOM exist

Here we will mention only **aperture-SNOM**, which often exploits tapered optical fibers as probes

SNOM probe: tapered optical fiber, with metallization and apical aperture a<<λ (*aperture-SNOM*)

Fig. 7.7a–d. SEM micrographs of SNOM probes: (a) Tip of an aperture probe consisting of a thermally pulled tip of a quartz monomode fiber coated with aluminum. (By Courtesy of Sunney Xie). (b) Etched fiber tip according to Ohtsu [7.23]. The tip is fabricated by wet etching of a monomode quartz fiber. The thickness of the fiber coating is strongly reduced at the end of the fiber and a sharply pointed tip sticking out from the end is formed from the core. (c) Aperture probe fabricated on the basis of an etched tip, as shown in (b). The etched tip is coated with gold which is removed from the apex of the tip by a lithographic process such that a small aperture is formed with the tip sticking out [7.117]. (d) Tetrahedral tip. The tetrahedral tip consists of a glass fragment which is coated with metal. By courtesy of, R. Reichelt, Institute of medical Physics and Biophysics, University of Münster

Typical aperture diameter: 50-100 nm

Note: metal layer (typ Cr, Ni) can absorb radiation → power entering the fiber cannot exceed the mW range!

Note: probe "throughput" (i.e., ratio between output/input power) is quite low for fiber probes, ~ 1/10000, but near field **intensity** can be large enough

SNOM probes (aperture-SNOM) II

Conventional probe fabrication
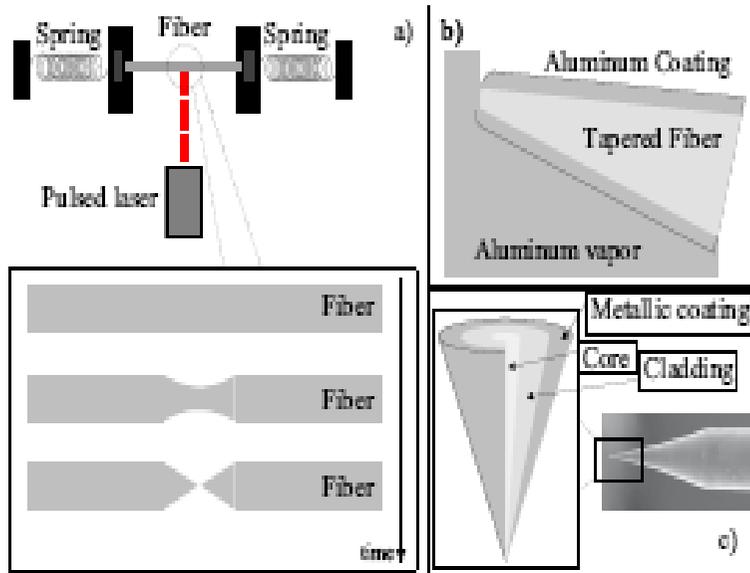
Figure 1.1: a) Heat and pull, one of the procedure to taper optical fibres for SNOM applications. b) Metallization of the SNOM fibre tip at steep angle to leave a sub-wavelength aperture at the end. c) SEM image of the resulting tip and sketch of its interior.

An alternative technique
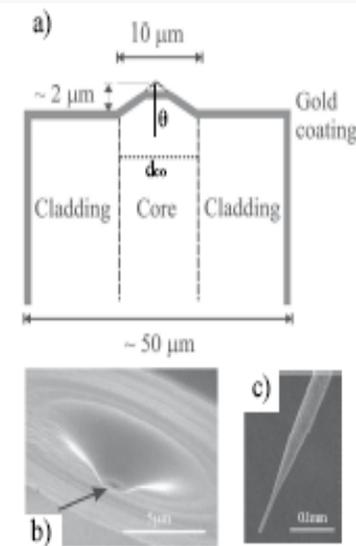
Figure 3.13: (a) Schematic of a SNOM fibre probe produced by selective chemical etching (SCE). The protruding cone is formed due to a slower etching rate of the core with respect to the cladding. After gold metallization (indicated by light gray lines), the tip is punched against a hard surface, producing a flattened apex with a sub-wavelength aperture at the center (black arrow), as evidenced by the SEM micrograph in (b).

An alternative probe

Figure 5.1: Back of an hollow cantilever. The square is the back aperture of the pyramidal hole produced by selective chemical etching. The inset shows a light spot coupled directly into the cantilever's hole by means of a microscope objective.

Many probes are available, including hollow cantilevers (similar to those for AFM, but with a pyramidal aperture)

Materiale tratto da Antonio Ambrosio
PhD Thesis Applied Physics, Pisa, 2005

Optical Near Field I

Ideal case (e.g., studied in the 20's by Bethe): radiation sent onto a conductive plane with a subwavelength aperture

When aperture diameter is much smaller than wavelength, far-field (propagating) intensity gets negligible compared to near-field (**non-propagating**) intensity

Near field space distribution in the ideal case can be approximated with two oscillating dipoles (electric and magnetic, respectively)

B .... k .... z

A .... k ....

a
Onda piana
a > λ

B .... k .... z

A .... k ....

a
Onda piana
a ~ λ

B .... k .... z

A .... k ....

a
Onda piana
a << λ

Schermo opaco

P_M

a

P_E

$|H|^2$=cost

$|E|^2$=cost

Onda incidente
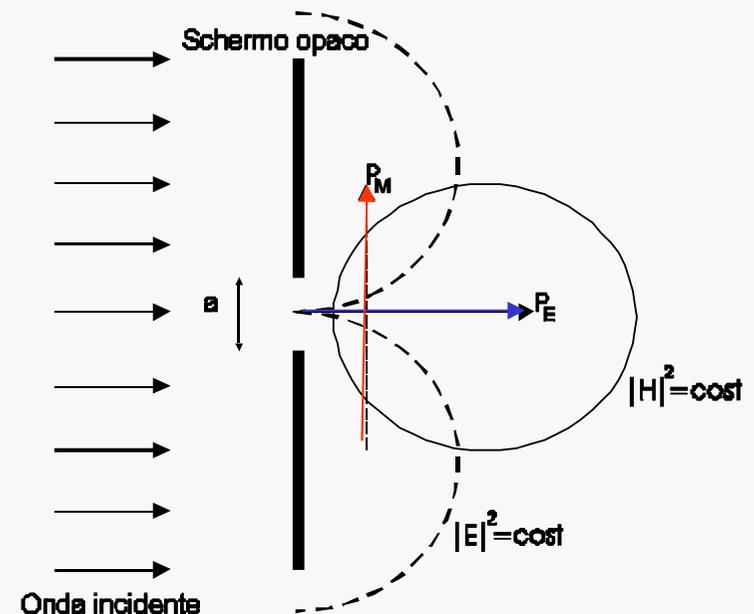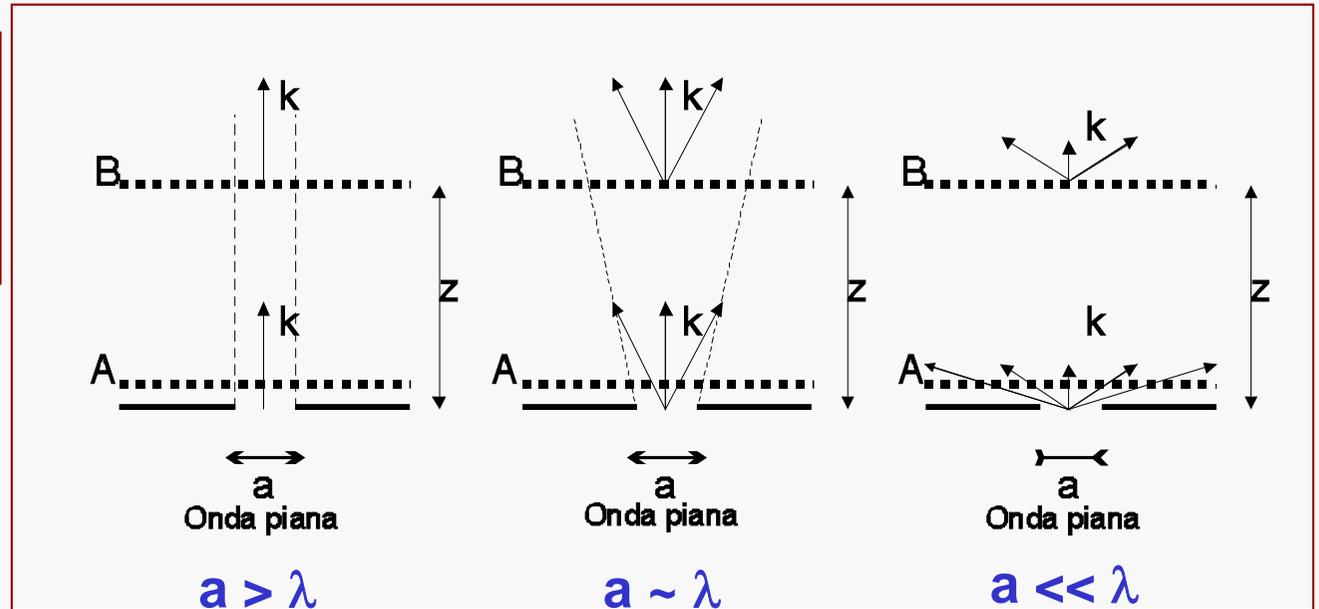
The resolving power of a conventional microscope, i.e. the distance (Δr) between two object points which a microscope can just resolve, depends on the numerical aperture (NA) of the objective and the wavelength (λ) of the light used. The relation between these quantities is fixed by the *Rayleigh's* criterion that sets:

$$\Delta r = 0.61 \frac{\lambda}{NA} \qquad (1.1)$$

Equation 1.1 has been derived following the theory of image formation in a microscope, formulated by Abbe in 1873 [1] and is limited by the diffraction suffered by light during propagation. The best microscope objective has a numerical aperture of $NA = 1.4$. Such high-performance objective combined with illumination in the lower visible wavelength ($\lambda = 400$ nm) leads to a resolving power $\Delta r \sim 170$ nm.

Using ring-shape illumination, the numerical factor in equation 1.1 can decrease until 0.36 leading to the best achievable resolving power of $\Delta r \sim 100$ nm.

The whole limits discussed above can be regarded in terms of quantum mechanics. In fact, applying the Heisenberg's uncertain principle to the components (x_i) of a photon's position and to those of the linear momentum (p_i) of the photon:

$$\Delta x_i \cdot |p_i| \geq \hbar \qquad (1.2)$$

where i is an index indicating the projections along x, y or z axes. Each component of the linear momentum of the photon is related to the corresponding components (k_i) of the light wavevector (k) by $p_i = \hbar k_i$. The relation 1.2 may then be written as:

$$\Delta x_i \geq \frac{1}{|k_i|} = \frac{1}{|n_i|} \frac{\lambda}{2\pi} \qquad (1.3)$$

This formula fixes the physical limit for the linear dimensions of a focused beam as well as the achievable optical resolution. The possible values of k_i are limited by the mathematical condition being between each vector and its components:

$$|k| = \sqrt{k_x^2 + k_y^2 + k_z^2} \qquad (1.4)$$

Classical optics and microscopy employ free propagating waves for which all the components k_i are real. In this case $k_i^2 = |k_i|^2$ and the relation 1.3 limits the best resolution achievable to values no much smaller than $\lambda/2$.

> "The subwavelength aperture is a low-pass filter for the spatial frequencies"

$$\Delta x \, \Delta k_x > 2\pi$$

$$E \propto \exp\left(iz \frac{2\pi}{\lambda} \sqrt{1 - (\lambda k_x)^2 - (\lambda k_y)^2} \right)$$
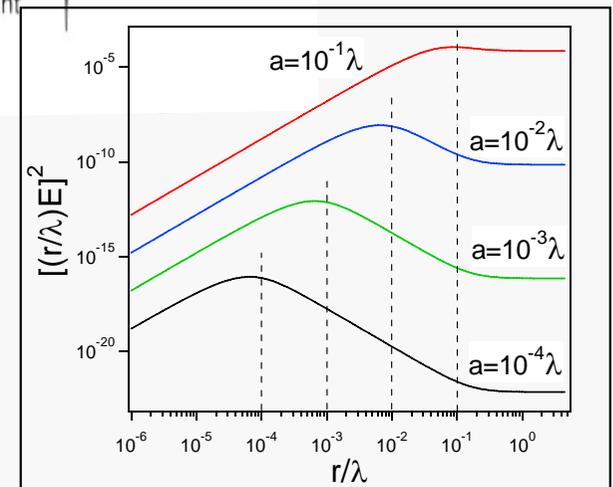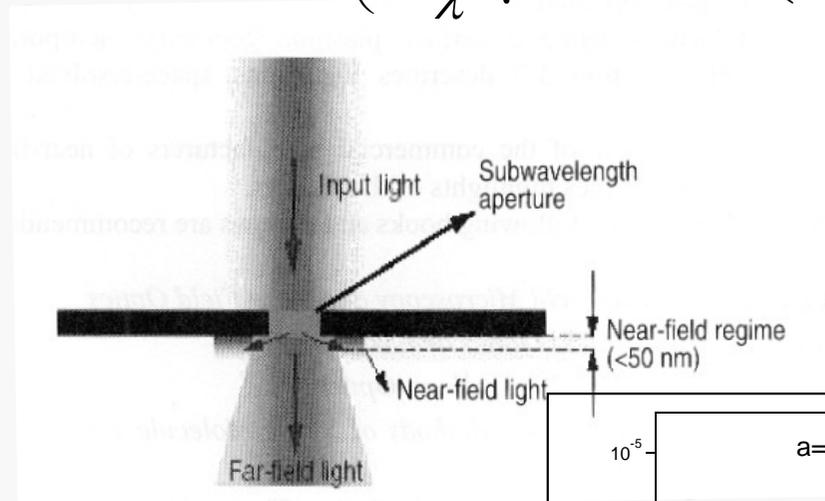
Near field intensity is a strong function of distance from tip (practically localized in a region sized ~a)

3.2 THEORETICAL MODELING OF NEAR-FIELD NANOSCOPIC INTERACTIONS

Although Maxwell's equations provide a general description of electromagnetic phenomena, their analytical solutions are limited to relatively simple cases and rigorous treatment of nanoscale optical interactions presents numerous challenges. The various ways of approaching the theory of near-field optics can be classified according to the following considerations (Courjon, 2003):

- The physical model of the light beam
- The space chosen to carry out the modeling (i.e., the direct space or Fourier space modeling)
- Global or nonglobal way of treating the problem (e.g., performing separate calculation for the field in the sample and then computing the capacity of the tip to collect the field)

Among several methods used for electromagnetic field calculation, one can distinguish techniques derived from the rigorous theory of gratings like the differential method (Courjon, 2003) and the Reciprocal-Space Perturbative Method (RSPM), as well as techniques that operate in direct space like the Finite-Difference Time-Domain Method (FDTD) and the Direct-Space Integral Equation Method (DSIEM).

In general, analytical solutions can provide a good theoretical understanding of simple problems, while a purely numerical approach (like that of the FTDT method) can be applied to complex structures. A compromise between a purely analytical and a purely numerical approach is the multiple multipole (MMP) model (Girard and Dereux, 1996). With the MMP model, the system being simulated is divided into homogeneous domains having well-defined dielectric properties. Within individual domains, enumerated by the index i, the electromagnetic field $f^{(i)}(\mathbf{r}, \omega_0)$ is expanded as a linear combination of basis functions

$$f^{(i)}(\mathbf{r}, \omega_0) \approx \sum_j A_j^{(i)} f_j(\mathbf{r}, \omega_0) \qquad (3.1)$$

where the basis functions $f_j(\mathbf{r}, \omega_0)$ are the analytical solutions for the field within a homogeneous domain. These basic functions satisfy the eigenwave equation for the eigenvalue q_j (analogous to the equation in Table 2.1):

$$-\nabla \times \nabla \times f_j(\mathbf{r}, \omega_0) + q_j^2 f_j(\mathbf{r}, \omega_0) = 0 \qquad (3.2)$$

MMP can use many different sets of basis fields, but fields of multipole character are considered the most useful. The parameters $A_j^{(i)}$ are obtained by numerical matching of the boundary conditions on the interfaces between the domains.

As an example of the use of this technique for investigations of nonlinear optical processes in the near field, we show here investigations of second harmonic generation in a noncentrosymmetric nanocrystal exposed to fundamental light from a near-field scanning tip (Jiang et al., 2000).

One notes that a consequence of nonlinear optical interaction in the near-field is that the phase-matching conditions do not need to be fulfilled because the domains are much smaller than the coherence length. Starting from Maxwell's equations, the electric fields of the fundamental and the second harmonic (SH) wave can be shown to satisfy the nonlinear coupled vector wave equations

$$\nabla \times \nabla \times \mathbf{E}(\mathbf{r}, \omega_0) - \frac{\omega_0^2}{c^2} \varepsilon(\mathbf{r}, \omega_0)\mathbf{E}(\mathbf{r}, \omega_0) = 4\pi \frac{\omega_0^2}{c^2}\mathbf{P}^2(\mathbf{r}, \omega_0) \qquad (3.3)$$

$$\nabla \times \nabla \times \mathbf{E}(\mathbf{r}, 2\omega_0) - \frac{4\omega_0^2}{c^2} \varepsilon(\mathbf{r}, 2\omega_0)\mathbf{E}(\mathbf{r}, 2\omega_0) = 4\pi \frac{4\omega_0^2}{c^2}\mathbf{P}^2(\mathbf{r}, 2\omega_0) \qquad (3.4)$$

where $\varepsilon(\mathbf{r}, \omega_0)$ and $\varepsilon(\mathbf{r}, 2\omega_0)$ are linear dielectric functions for the fundamental and the SH waves, respectively.

The propagation constant k_z along the z direction is

$$k_z = (\mathbf{k}^2 - \mathbf{k}_{\parallel}^2)^{1/2} = k_0(1 - n_1^2 \sin^2 \theta)^{1/2} \qquad (3.5)$$

where $k_0 = 2\pi/\lambda$, λ is the wavelength of illumination light in free space; n_1 is the refractive index of the tip, and θ is the incident angle. If $1 - n_1^2 \sin^2 \theta > 0$ (i.e., k_z is real), the waves will propagate with constant amplitude between the probe and the sample, which corresponds to the "allowed light" in the sample. In the areas where k_z is imaginary, the waves will decay exponentially within distances comparable to the wavelength, thus such waves have evanescent character and produce the "forbidden light" in the sample. From the electrical field distribution of the fundamental wave calculated with the MMP method, we can obtain the electrical field distribution of the SH wave and the different contributions of "allowed light" and "forbidden light."

Detailed description of the near field produced by actual probes requires sophisticated numerical methods

Da P.Prasad, Nanophotonics (Wiley, 2004)

Tip/sample distance control

Shear-force method

Sostegno portapunta
Filtro ν=ν1−ν2 → AD 536 A
Scheda PC
Oscillatore O2
Oscillatore O1
Mixer
Amplificatore
Piezoelettrico di *dither*
Fork
Punta

Q=400
F0=33800
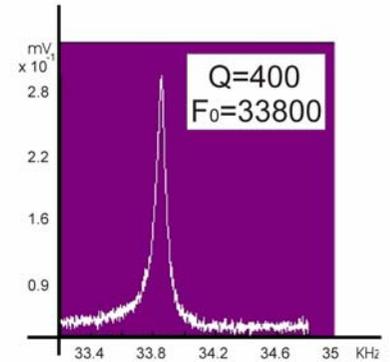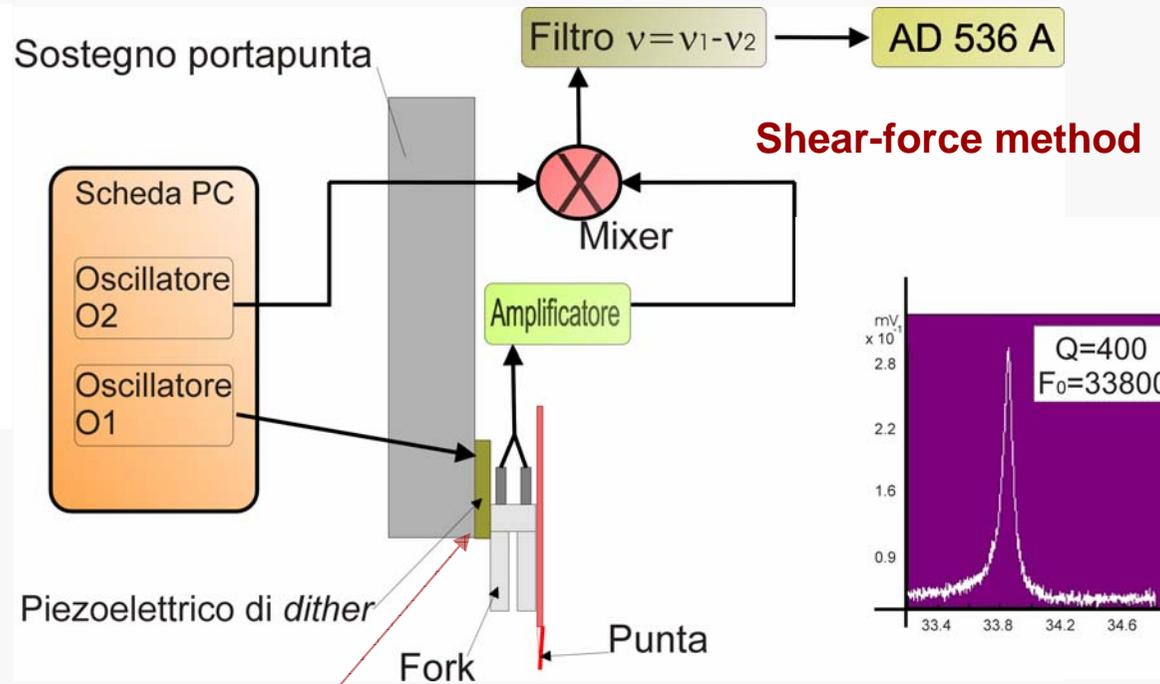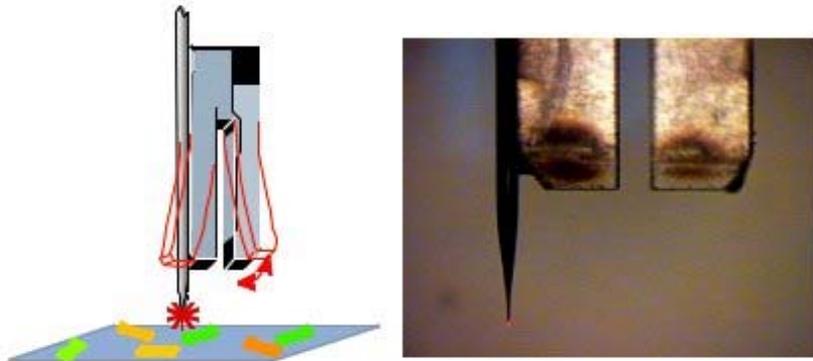
tip approach curve
fiber osc. amplitude (arb. units)
working point
tip-sample distance
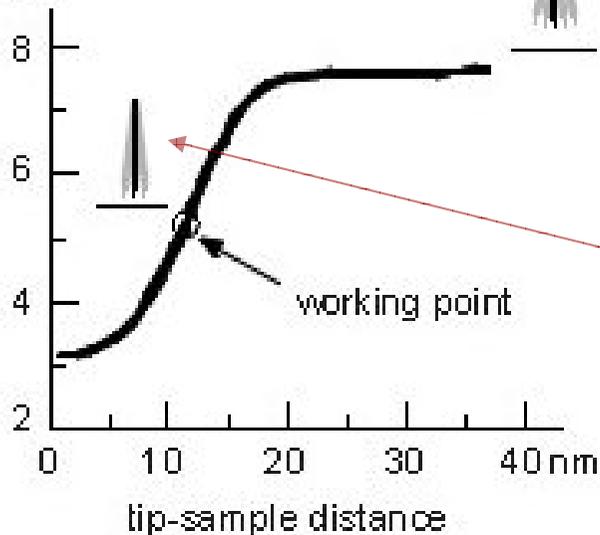
- A dithering piezoelectric transducer keeps the probe tip in oscillation along a direction **parallel** to the surface
- Oscillation amplitude is monitored by a *tuning fork*
- When the distance gets smaller (typ., below 10 nm), the oscillation is **damped** (and phase is changed) due to **shear-forces** involving many effects (e.g., viscous interaction of the air layer between tip and sample)
- Similar to AFM in tapping mode, but for the oscillation direction, the relevant distance and the involved mechanisms

Operation modes for SNOM I

Illumination mode **Collection mode**

Fig. 7.3. The characteristic components of a SNOM. In collection modes the position of the detector and of the source is interchanged with respect to their position in the illumination modes
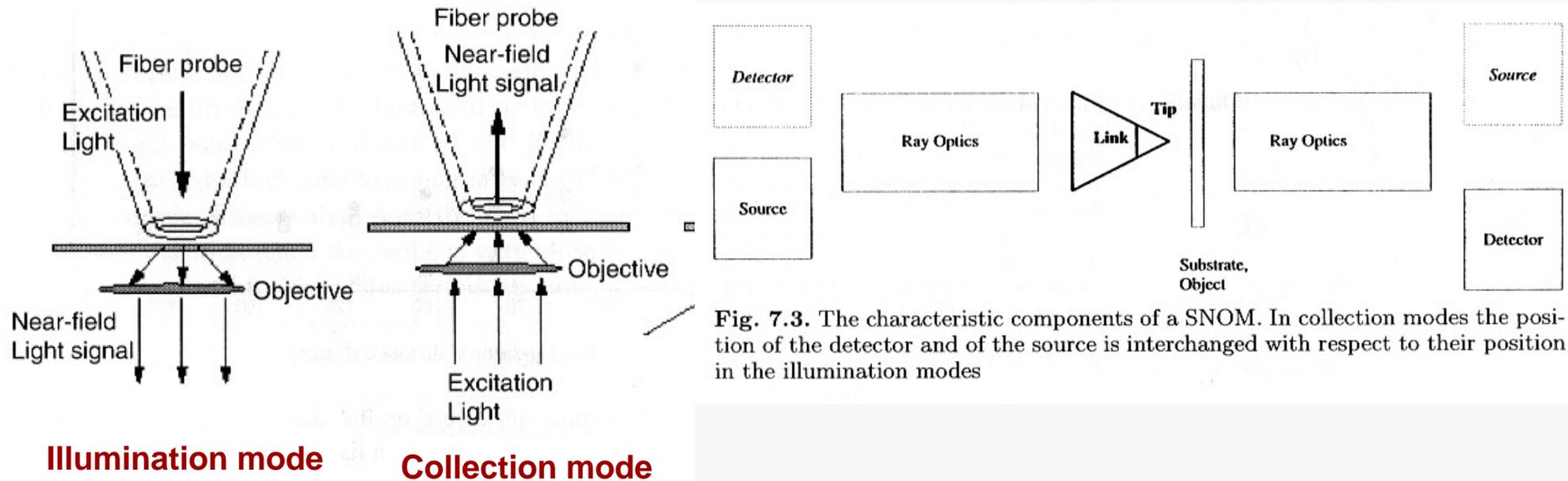
In **illumination mode** (the most common) the surface is concerned by the near field and the resulting scattered light is collected "in the far field" (either in transmission or reflection)

In **collection mode** the surface is illuminated by a propagating (conventional) field and the resulting scattered light is collected in the near field by the probe

Sub-diffraction space resolution is due to the non-propagating character of the near-field
(typ resolution comparable to the aperture size, i.e., tens of nanometers)

7.2.1 Ray Optics of a SNOM

SNOM techniques differ mainly in the types of probes which are used and also by their ray optical components, i.e., their optical scheme, which is useful for a classification of most types of SNOM concepts. As shown schematically in Fig. 7.4, three different regions where the rays propagate can be distinguished: I) the body of the probe, II) the outside and III) the substrate of the object. In general, regions I and III will have a higher refractive index than the outside region II. Different angular domains of rays propagating in regions I and III exist, which can be distinguished by the criterion of total reflection of a ray falling on its boundary or of it being partially refracted into the outside II. Thus, in the case of a transparent substrate III, we distinguish between the angular domain III_1 of angles ε with $-\varepsilon_t < \varepsilon < \varepsilon_t$, where ε_t is the critical angle of total reflection ($\varepsilon_t = 41.5°$ for glass of refractive index 1.5) and the angular domain III_2 with $90° > \varepsilon > \varepsilon_t$ or $-90° < \varepsilon < -\varepsilon_t$, which is sometimes called the range of forbidden light. Rays of the domain III_2 are totally reflected in the substrate, whereas rays of domain III_1 are partially refracted into the outside II. Also within the body of the tip I two different domains may be distinguished (Fig. 7.4). This figure only shows the case of a rectangular wedge, a two-dimensional analog of the three-dimensional body of the tip. For such a wedge, with a refractive index $n = 1.5$, rays entering at an angle within the angular domain ($-3.5° < \varepsilon < +3.5°$, region I_2) will be totally reflected back into a reflected ray of the same angle ε. Rays entering the wedge at different angles will also be reflected into the same angle and be partially refracted into the outside II of the wedge. This situation also applies, if the wedge is coated with a partially transparent metal film, as is typical for SNOM probes. Similar considerations also apply for a three-dimensional tip.

In summary, in many cases it is possible to distinguish in regions I and III between angular domains I_1 and III_1 where total reflection of the rays occurs into the same domain and the domains I_2 and III_2 from where light is partially refracted to the outside II.
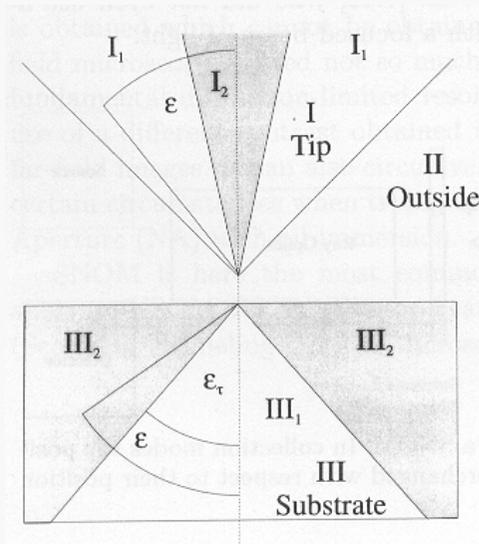
Fig. 7.4. Ray optics of a SNOM. One can distinguish between three different regions where the rays propagate; the body of the probe I, the outside II and the substrate III of the object. Different angular domains of rays propagating in regions III and I at an angle ε can be distinguished by the criterion of a ray falling on its boundary being totally reflected into the same domain (III_2, I_2) or being partially refracted into the outside II (III_1, I_1)

In illumination mode, once scattered from the surface, photons acquire a propagating character
→ Detection of the scattered radiation can be carried out by using conventional (far-field) optics (and sub-diffraction space resolution is still given by the spatial extent of the exciting near field)

What can be measured by SNOM

The effects of the **local interaction between the sample surface** (i.e., a layer with thickness comparable to the near field range) **and the near field** photons are recorded

They can be regarded as analogous (but for the sub-diffraction resolution and the surface origin) of conventional **optical transmission and/or reflection** measurements (depending whether the sample is transparent or opaque)

Non propagating behavior of the exciting near field can however play a role (for instance, specific polarization can give access to otherwise forbidden transitions, …)

Examples

✓ **Local variations of the "refractive index"** can be derived by analyzing the scattered radiation
✓ In case of emitting (photoluminescent) samples, fluorescence can be excited by the near field, and **photoluminescence** maps can be acquired
✓ By implementing a polarization control system *(see later on)*, **optical activity** of the sample (e.g., dichroism, birifringence) can be analyzed at the sub-diffraction level

Examples

Collection mode can be used to map emission of, e.g., electroluminescent devices
Also, evanescent radiation, e.g., stemming from a waveguide surface, can be mapped

In addition, the tip/sample distance control, being based on a feedback system, allows acquisition of topography maps simultaneously with every SNOM scan (with a space resolution in the tens nm range)
Morphological and optical information acquired and compared at glance!

A very few words on apertureless SNOM

3.5 APERTURELESS NEAR-FIELD SPECTROSCOPY AND MICROSCOPY

As mentioned in Section 3.3, an emerging approach is the apertureless near-field spectroscopy and microscopy (Novotny et al., 1998; Sanchez et al., 1999; Bouhelier et al., 2003). The use of an aperture such as a tapered fiber opening poses a number of experimental limitations. Some of these are:

- Low light throughput due to the small fiber aperture and the finite skin depth (light penetration) into the aluminum metal coating around the tapered fiber.
- Absorption of light in the metal coating; this can produce significant heating that can create a problem in imaging, particularly of biological samples.
- Pulse broadening in the fiber, when using short pulses for nonlinear optical studies. Also, the fiber tip may be damaged by the high peak intensity as already discussed in Section 3.3.

The apertureless approach overcomes these limitations, at the same time providing a significantly improved resolution. It has been demonstrated by Novotny, Xie, and co-workers (Sanchez et al., 1999; Hartschuh et al., 2003; Bouhelier et al., 2003) that optical images and spectra of nanodomains ≤25 nm can be obtained using the apertureless near-field approach involving a metal tip of end diameter ≤10 nm.
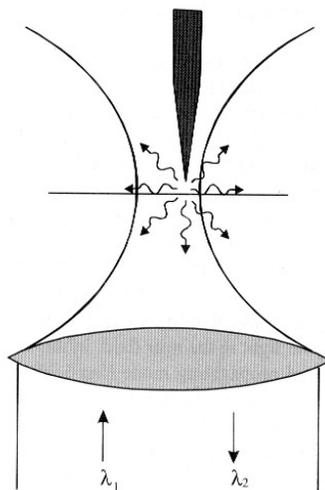
The two approaches used for apertureless NSOM are:

1. Scattering type, which involves nanoscopic localization and field enhancement of the electromagnetic radiation by scattering of the light from a metallic nanostructure. An example is provided by Figure 3.2 where the light is scattered by a sharp metallic tip. Scattering and field localization can also be produced by a metallic nanoparticle within nanometers of distance from the sample surface. The localization and enhancement of electromagnetic field by plasmon coupling to a metallic nanoparticle is discussed in Chapter 5 under "Plasmonics." This principle of obtaining nanoscopic resolution using scattering from a metallic nanoparticle also forms the basis of "plasmonic printing," discussed in Chapter 11 on "Nanolithography".

2. Field-enhancing apertureless NSOM, where a metallic tip is used to enhance the field of an incident light in the near field. In this case, the light is incident on the tip as a normal propagating mode (far-field). The strongly enhanced electric field at the metal tip produces nanoscopic localization of optical excitation. This approach offers simplicity and versatility of using light by just focusing on the metallic tip through a high-numerical-aperture lens. Hence it is described here in detail, with examples of some recent studies utilizing this approach.

Figure 3.22. Metallic tip enhancing the local field by interacting with the focused beam at λ_1. The optical response at another wavelength λ_2 is collected by the same objective lens.

A nanoparticle, or a nanosized tip, irradiated by a propagating field, acts as the quasi-pointlike source of the near field

Advantages:
➢Better space resolution (below 10 nm??)
➢No, or negligible, throughput limitations

Disadvantages:
➢Cumbersome operation
➢Stray light (in the far field)

Examples of SNOM photoluminescence

Saiki et al. (1998) and Matsuda et al. (2001) conducted room temperature photo-luminescence study on a single quantum dot from InGaAs quantum dots grown on a GaAs substrate. Their result is shown in Figure 3.12. Because of the spectral resolution obtained by sampling only a single quantum dot (no inhomogeneous broadening), they were able to observe, at an appropriate excitation density, emission not only from the lowest level (subband) of the conduction band but also from higher levels. (See Chapter 4 for a description of these bands.) They were able to study the homogeneous line width, determined by the dephasing time of excitation (see Chapter 6 for a description of dephasing time), as a function of the interlevel spacing energy. They found that the line width was larger for a smaller-size quantum dot for which the interlevel spacing is larger. (This is predicted by a simple particle in a box model as the length of the box becomes smaller, see Chapters 2 and 4.)

Figure 3.13. Fluorescence NSOM images of single molecules. From Professor D. Higgins and Professor P. Barbara, unpublished results.

Figure 3.12. Photoluminescence spectrum of single QD at room temperature (a), and dependence of the homogeneous linewidth of ground-state emission on interval spacing, which is closely related to size of Qd's (b). From Saiki and Narita (2002), reproduced with permission.
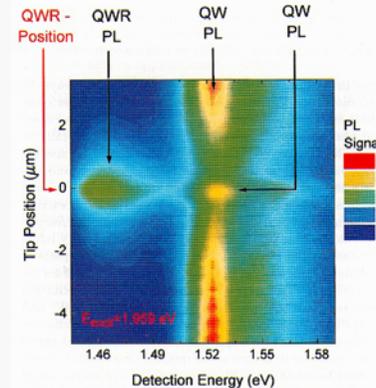
Fig. 7.23. Spatially resolved near-field photoluminescence spectrum of the quantum wire heterostructure. The spectrum was recorded for spatially resolved excitation of the sample at 1.959 eV. The tip was scanned along the lateral direction perpendicular to the wire. The PL intensity (in arbitrary units) is plotted as a function of tip position and detection energy. The color red corresponds to high, while purple corresponds to low PL intensity. The quantum wire emission is centered around 1.46 eV. Note that, in addition to the flat quantum well luminescence at 1.522 eV, a further, slightly blue shifted, sidewall quantum well emission is resolved
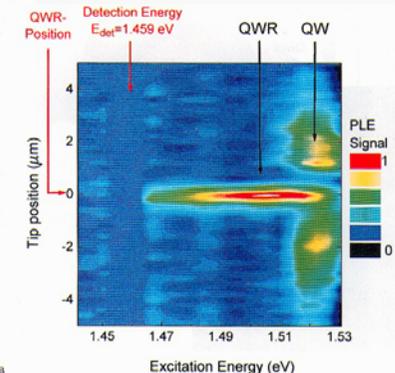
Fig. 7.24. Spatially resolved near-field photoluminescence excitation spectrum. The PLE signal is plotted as a function of tip position and excitation energy. The scan direction is perpendicular to the wire. The photoluminescence was detected at 1.46 eV. The color red corresponds to high and purple to low intensity

Single, isolated nanostructures, nanoparticles, or emitting molecules can be analyzed in spectral terms

A system is used to control the polarization of the laser light entering the fiber probe: polarization is linear but continuously rotating (at a frequency typ. in the kHz range)
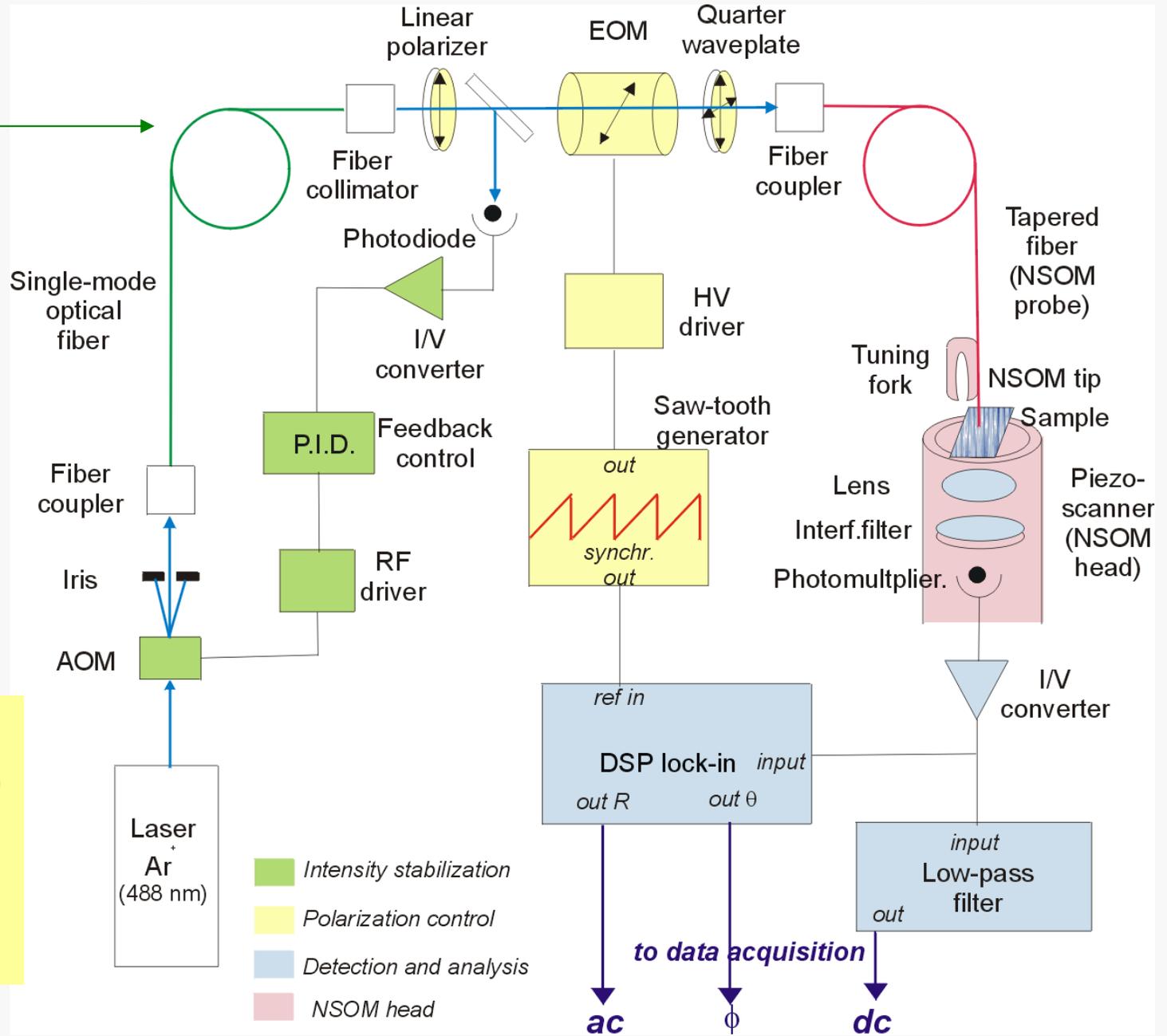
Optical activity of s samplem (e.g., dichroism, birifringence) can be anlyzed with sub-diffraction space resolution

Linear polarizer

EOM

Quarter waveplate

Fiber collimator

Photodiode

I/V converter

Single-mode optical fiber

Fiber coupler

Tapered fiber (NSOM probe)

HV driver

Tuning fork

NSOM tip

Sample

P.I.D. — Feedback control

Saw-tooth generator

Lens

Piezo-scanner (NSOM head)

Iris

RF driver

out

synchr. out

Interf.filter

Photomultplier.

AOM

ref in

I/V converter

DSP lock-in   input

out R   out θ

input

Low-pass filter

out

Laser + Ar (488 nm)

Intensity stabilization

Polarization control

Detection and analysis

NSOM head

to data acquisition

ac   φ   **dc**

PM-SNOM II

A viable example of application:
Investigation of host-guest systems (high density PET matrix containing a dispersion of molecular chromophore)
Mechanical stretching of the polymer film leads to *linear dichroism*

Tertiophene-like chromophore dispersed (3% wt) in a ultra-high molecular weight polyethilene (UHMWP)

Chromophore molecule

Chromophore choice:
➤ chemical compatibility with the host;
➤ rigid structure;
➤ absorption in the blue (peaked around 400 nm);
➤ optical activity (right- and left-handed isomers available).

Fabrication process (at *Dipartimento di Chimica e Chimica Industriale, Università di Pisa, group of Prof. Ciardelli and Prof. Ruggeri*):
- cast (to obtain pristine films) followed by
- high temperature drawing (to obtain films with stretched polymer chains)

PM-SNOM III

Sample: L-R (50:50) stretched (drawing ratio 30), 10x10 µm scan
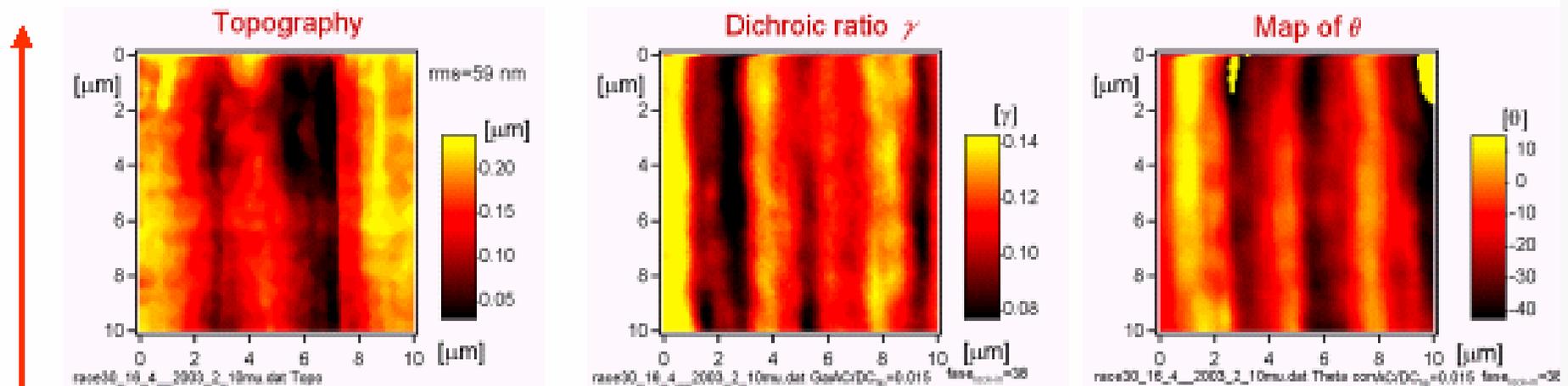
drawing direction

Topographical variations due to local changes in polymer chain stretching

Local optical activity strongly affected by (host) stretching

Chromophore molecules follow host molecule alignment
Macroscopic dichroism ($\gamma \sim 0.1$ in this sample) due to the combined effect of elongated islands with locally inhomogeneous optical activity

Information on the sample properties (and suggestions to improve the fabrication process) can be found which are masked in conventional (macroscopic) polarimetry

4. "Lithography" with SPMs

"As usual", the microscopy is "accompanied" by a "lithography"

In this case, the term "lithography" can be better replaced by "**manipulation**", since position and/or local properties of the materials can be modified, i.e., manipulated, by SPMs

Indeed, as we have already seen in several examples, matter can be **manipulated at the nanometer level** by using SPMs (e.g.: CNT or nanoparticle based MOSFETs)

This kind of "lithography" is obviously *serial*, due to the scanning nature of SPMs, and not suited for industrial environment, but attempts are being made to get some *parallel* character (e.g, by using several probes in parallel)

Wide variety of methods can be envisioned: we will mention here in the following a few of them, based on STM, AFM, and SNOM

Their relevance is in fabrication, in surface modifications, in nanowriting for data storage

Nanomanipulation by SPM

Main objectives:

The excellent space resolution offered by SPM can be exploited also to:
• Manipulate (spatially) nanoparticles on a surface;
• Produce very local modifications of the surface (physical and/or chemical)

5 Manipulation of Atoms and Molecules

The scanning probe microscopes do not only have the ability to image individual atoms. The interaction needed for imaging the surfaces can also be used to manipulate individual adatoms, molecules, or the surface structure itself on the atomic scale. Indeed a large number of works concentrated on the manipulation of individual atoms and in the following novel nanostructures were built. Here we briefly show the work by Eigler and coworkers [44], [45] as examples, followed by a more subtle tip-induced manipulation of atoms, and the tip-induced migration of defects by tip-induced excitement of defects [46], [47]. More recently the group of Rieder could even perform full chemical reactions with single molecules [48]. Three different manipulation modes can by distinguished: the lateral and the vertical manipulation as well as the tunnel current induced changes. The combination of all three modes enables to achieve tip controlled chemical reactions.

The same instrument can be used to produce and assess the manipulation
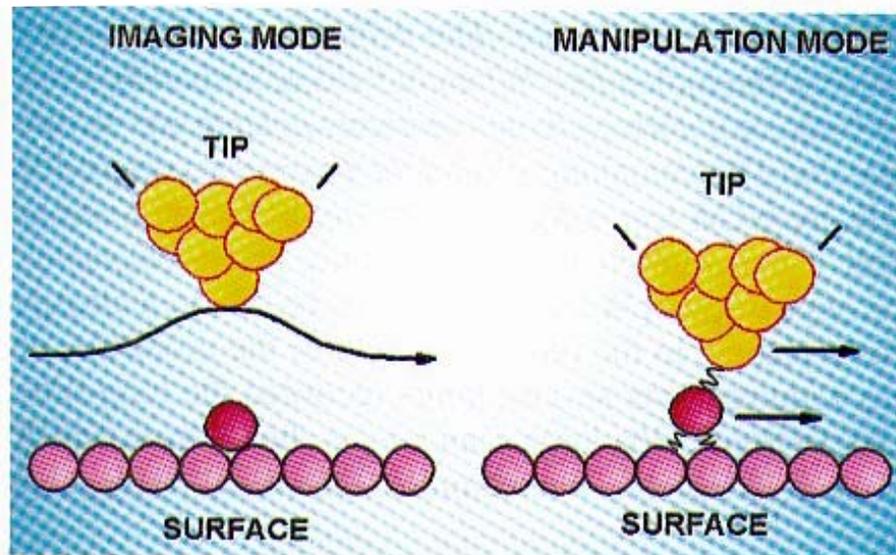

Figure 32: In the STM imaging mode the tunnel current is kept constant and the cantilever is raised. For manipulation the tip is lowered above an atom dragging it to the desired position, lifting the cantilever losing interaction with the atom [44].

Da R. Waser Ed., Nanoelectronics and information technology (Wiley-VCH, 2003)

In the STM device, the tip is so close to the target as to make the electron current highly spatially confined - it is the key to the extremely high spatial resolution of STM images. The key element in surface modifications is also the STM tip. To affect these modifications one utilizes a variety of tip-sample interactions, including attractive and repulsive forces, electric fields, and the effect of highly spatially confined electron currents. The small distance between tip and sample, which is about one nanometer, causes electrons to tunnel to (or from) a region on the sample that is approximately one nanometer in diameter, with an even smaller major distribution area. Thus, the surface fabrication produced by STM must be performed on the nanometer scale, i.e., STM can nanofabricate. Later, we will see that it is also possible to manipulate a single atom or molecule adsorbed on the surface with STM.

Since the invention of STM in 1981, as a nanofabrication tool it has been used in direct surface identation, electron-beam-induced deposition, etching, single-atom manipulation, and so on. All of these techniques have a wide-spread application potential. First, it is possible to reduce the line-width of large-scale integrated circuits from the micrometer scale to the nanometer scale by lithography, beam-induced deposition and etching, which is one of the goals of high technology. In most cases the resulting feature with dimensions on the order of hundred nm [9.1], but features with dimensions of a few nm have also been achieved [9.2-4]. An exciting possibility will be to use the tip to "operate" on biomolecules such as DNA and proteins. The electronic properties of devices may be dominated by quan-tum-size effects when their size is reduced to the nanometer or atomic scale. By STM and other techniques, it is possible to discover new phenomena, design new devices and fabricate them. Next, STM can be utilized to repair masks and integrated circuits. The surface topographies can be imaged in situ during the surface fabrication process by STM, which makes it possible to discover defects in masks and circuits, to repair them by surface deposition and etching, and then to examine the final results by STM. Lastly, using the STM as a tool, the essential research on the growth, migration and diffusion of clusters on surfaces, and the interactions between small particles or between substrates and particles can be performed in order to manipulate clusters or atoms on purpose.

Lens-focused electron beams, ion beams and X-rays can also be employed in nanofabrication. Although the STM seems unlikely to become competitive in some areas of nanofabrication such as wafer-scale resist patterning, it has its own characteristics. First, an STM can work in either the tunneling mode or the field-emission mode. When working in the latter, a low applied voltage (higher than a few volts) can produce a strong enough electric field to make electrons emit from the tip over the barrier, because the distance between tip and sample is very small. These emitting electrons with a certain current and energy, will not diverge greatly because of the small separation which results in a nanometer beam diamter on the substrate surface. Unlike conventional high-energy electron lithography, the low-energy STM beam reduces the problems associated with electron back-scattering and the generation of secondary electrons. A resolution of about 10 nm, and exposure rates comparable to those of conventional electron lithography have been achieved. Secondly, by moving the tip to contact the sample, the STM tip can also produce local contact forces and electrostatic forces in a small region on the sample surface to create indentations directly. Lastly, at present, STM is the only instrument that can provide a nm-sized beam of very low energy electrons (0÷20eV). The importance of electrons with low energy is obvious when it is considered that many of the processes such as migration, bond breaking, chemical reactions that would be interesting to control, have activation energies less than 10 eV per atom which require a low-energy beam.

Nanomanipulation by STM: application of suitable voltages or voltage pulses can be used to "modify" (typ to break) matter

9.4 Nanofabrication in Solution and in Gaseous Environments

Electron-beam-induced etching and deposition is a way of writing patterns on substrates in solution and in gaseous environments. The basic idea for etching and deposition is very simple. The focused beam is used to supply energy to decompose chemicals in a localized region. The decomposition products can include a metallic species to be deposited on a surface, or a corrosive species intended to participate in an etching reaction resulting in locally etched structures on a surface. The substrates used include Si, GaAs, graphite and metals. The STM system for operation in solution should supply the necessary solution. To minimize unwanted Faradic leakage current, the tip must be treated using some special methods such as coating wax up to the extreme end of the tip (Chap.4). Deposition and etching can also be induced with the STM tip as an electrochemical electrode to drive a localized Faradic current of ions. A gaseous environment can be utilized by introducing organometallic gas with a pressure of several Pa into a vacuum chamber with a base pressure of $10^{-5} \div 10^{-6}$ Pa. For different deposition metals, the introduced gas is different. They include DMCd, $W(CO)_6$, WF_6, and organometallic chemical of Au. Three possible mechanisms have been assumed to account for the dissociation of organometallic molecules [9.35]. (i) Electrons tunneling inelastically between the tip and sample break apart gas molecules adsorbed on the surface of the substrate. (ii) Current traveling between the tip and sample can locally heat the surface of the substrate enough to cause pyrolytic dissociation of adsorbed gas molecules. (iii) High fields between the tip and sample break down the gas creating a microscopic plasma between the tip and sample which then deposits the metal atoms on the surface. All of these will break the chemical bonds from the energy of electrons traveling between the tip and sample, thus the STM ought to be operated in the field-emission mode.
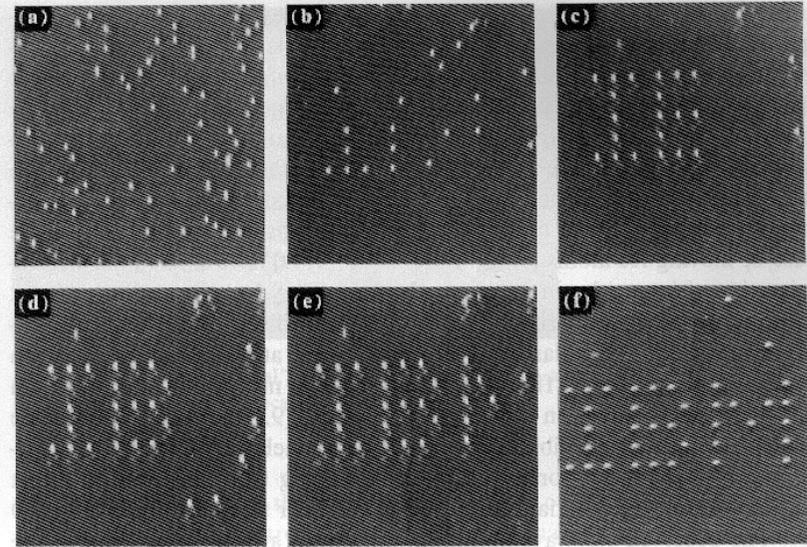
Nanomanipulation of Xe atoms on a surface

Fig. 9.10a–f. A sequence of STM images taken during the built-up of a patterned array of the letters I, B and M constructed of xenon atoms on the Ni (110) surface. The atomic structure of the nickel surface is not resolved. (a) The surface after xenon dosing. (b)-(f) Various stages during the construction. Each letter is 5 nm from top to bottom [9.40]

Electric fields locally applied by STM can induce local modifications, chemical reactions,...)

5.3 Effects induced by the Tunnel Current

It is also possible to excite atoms by the tip-sample interactions. Figure 42 shows a set of consecutive STM images acquired with 8 s time interval. The images show that the defects change their lattice positions [58], [59]. The tip can excite defects by several physical mechanism. The case shown here is based on a field-induced migration, due to the strong electrostatic field penetrating into the semiconductor. Defects can, however, also be excited by tunnelling of minority carriers into defect states followed by a charge carrier recombination with electron-phonon coupling [47]. There are surely even further mechanisms which may possibly excite atoms on the surface. Which of those will take place depends sensitively on the measurement conditions.

Finally, in Figure 43 the cutting of a carbon nano tube with an AFM is presented [60]. Earlier experiments controlling the length of carbon nano tubes were carried out using a STM [61]. At first the 600 nm^2 area is scanned then the AFM cantilever is lowered at the positions marked in the left image and for cutting a voltage pulse of −6 V is applied. The image on the right hand side shows the carbon nano tube after cutting.

Defects can be "excited" (or created) by local tunneling currents

Figure 42: Migration of three phosphorus vacancies on the GaP(110) surface. The chances of the lattice positions of the vacancies is induced by the tip of the scanning tunnelling microscope. In this particular case the jumps are field-induced.
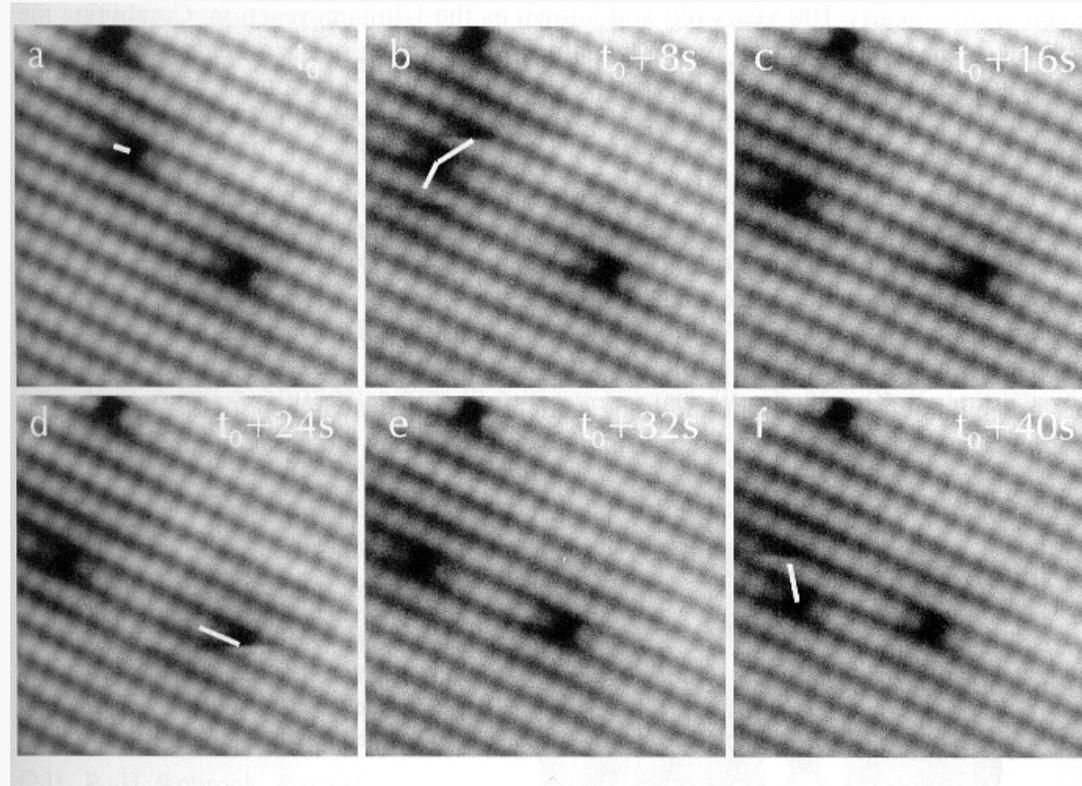
5.4 Complex Chemical reactions with the STM

In 1904, Ullmann et al. heated iodobenzene with copper powder as catalyst and discovered the formation of biphenyl with high purity [62]. This aromatic ring coupling mechanism is now nearly 100 years old and known as the Ullmann reaction. Combining the presented STM manipulation methods, namely the moving of adsorbents and the influence via increased tunnel current, it is possible to control this complex chemical reactions at low temperatures step by step. S. H. Hla et al. presented the synthesis of to one biphenyl molecule out of two iodobenzene on a copper surface at 20 K [48].

The synthesis consist of three different steps. First two iodobenzene (C_6H_5I) have to be dissociated into phenyl (C_6H_5) and iodine (Figure 44a and b). Secondly the two phenyl rings have to be located one to another (Figure 44d and e) and finally in the third step, through tunnelling electrons the two phenyl rings are associated to biphenyl (Figure 44e).

To abstract the iodine from the iodobenzene the STM tip is positioned right above the molecule at a fixed height and a the sample voltage is switched to 1.5 V for several seconds. The energy transfer from a single electron causes the breaking of the C-I bond Figure 45a – c, [62]. As the bond energies of the C-H and C-C bonds are two and three times higher than the C-I bond, it is not possible to break them with a single electron process at this voltage. After preparing to phenyl reactants and moving away the iodine, the left phenyl Figure 45c is brought close to the other one by lateral manipulation using the tip adsorbate forces Figure 45d. Though the two phenyls are close together they do not join at 20 K. The two phenyls can easily be separated again by lateral manipulation. Both phenyls are still bond to the Cu step edge via their σ_{C-Cu} bonds. Figure 46 shows a model where the phenyl is lying with its ð ring on the terrace while one of its C atoms is pointing towards the step edge and σ-bonding to a Cu atom. The final reaction step to associate the two phenyls to biphenyl is done by positioning the tip right above the centre of the phenyl couple and increasing the current drastically. The successful chemical association can be proved by pulling the synthesized molecule by its front end with the STM tip [62].

STM-controlled electrochemical reactions
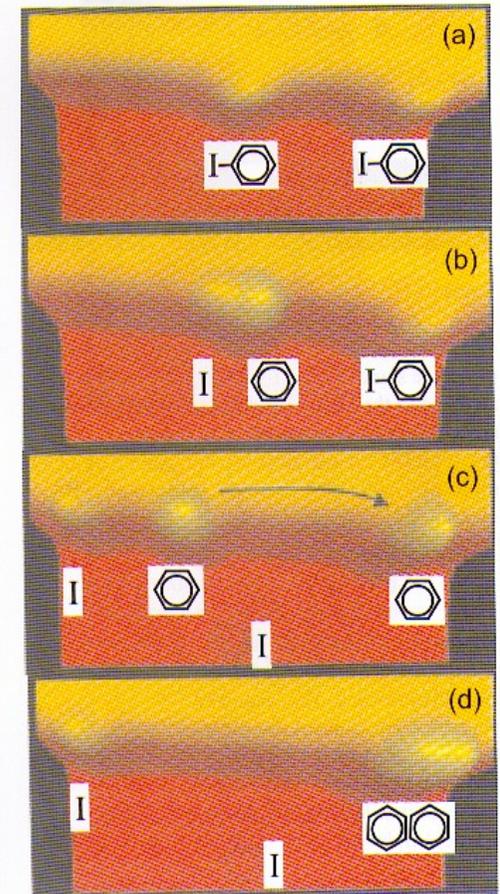
Figure 45: STM image of the Ullmann synthesis induced by the tip.
(a) Two iodobenzene molecules are absorbed at a Cu(111) step edge. Introducing a voltage pulse through the tip abstracts the iodine from the phenyl molecules
(b) (the left molecule).
(c) By lateral manipulation the molecules are further separated and
(d) the phenyl molecules are moved together to prepare for their association. (scan area 7 × 3 nm²) [48]
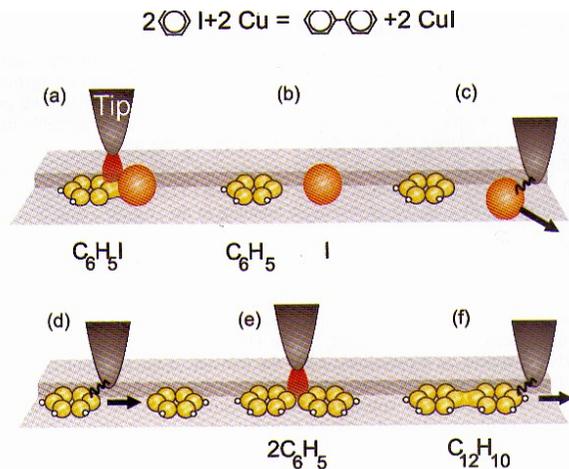
$2\ \text{◯}\ I + 2\ Cu = \text{◯}-\text{◯} + 2\ CuI$

Figure 44: Schematic presentation of the tip-induced Ullmann reaction.
(a), (b) Electron-induced abstraction of the iodine from the iodobenzene.
(c) Pulling the iodine atom to a terrace site.
(d) Bringing together to two phenyl molecules by lateral manipulation and
(e) electron-induced chemical association to biphenyl.
(f) Pulling the synthesized molecule by its front end to prove the association.

9.3 Nanolithography on Resist Films

Direct writing of nanometer-scale features on organic materials opens the door to using film as a resist for the etching mask and the possibility of etching in air [9.30].

The resists can directly be exposed with conventionally focused electron beams to create various structures. The e-beam resist materials frequently utilized in conventional lithography are PolyMethylMethAcrylate (PMMA) and polydiacetylene with urethane substitutents (P4BCMU). They are typically sensitive to low-energy (<20 eV) electrons. The primary beam of a conventional e-beam lithography system has a considerably higher energy, so exposure of the resist occurs through interactions with secondary and backscattered electrons produced by the primary beam; a resist is consequently exposed over an area which is significantly larger than the primary beam spot size. The STM, even working in the field-emission mode, can supply focused electron beams with low energy which can interact with resists directly. Because the tip can be held within a few nanometers from the sample, which leads to an effective beam spot size on the sample of the order of the tip-sample separation, and the tip can transversely scan over the surface controlled precisely by a computer, STM can easily be employed in lithography for writing directly on the resist surface. The degradation in resolution because of interactions between the resist material and secondary electrons in conventional lithography can be overcome in STM lithography, which makes it possible to obtain more precise structures. Using STM it is also possible to make a thorough investigation of the exposure mechanism by controlling the bias voltage precisely (i.e., the energy of electrons with which the resists are exposed) in a certain time interval under constant current. In addition, STM generally ought to work in the field-emission mode because the electrons must have enough energy to induce a chemical reaction in resists (i.e., to expose resists). In this mode, a linear

dependence of the tip-sample separation on the bias is expected in the absence of geometric effects, which make the widths of the features increase with the bias voltage.

In order to be successfully exposed with an STM, the resist film coated on conducting substrates such as Si, GaAs, Au, graphite and so on must be extremely thin, on the order of a few tens of nanometers, for two reasons. First, the low-energy electrons must be able to completely penetrate the film in order to properly expose it and to prevent excessive charging of the surface. Second, if the film thickness is greater than the gap between the tip and the conducting substrate, the tip will penetrate and damage the resist film. Experimentally, the thickest film that can be used is V nm, where V is the bias voltage in volts. There are different kinds of materials which can be used as resist films in STM lithography, including polymers such as PMMA and P4BCMU which were often employed in conventional e-beam lithography, metal halides such as GaF_2 and AlF_3, etc. The resist can be applied to the substrates by evaporation or deposited from a Langmuir-Blodgett (LB) film balance and spin coating.
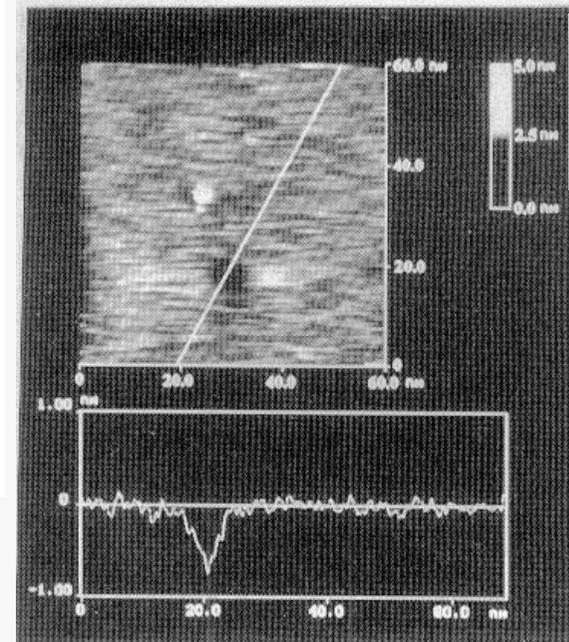

Fig. 9.3. The cross sectional profile of a STM fabricated crater on HOPG fitted with the numerical results derived from a low energy electron diffusion model [9.15]

The local electric field produced by the STM tip behaves similarly to the electron beam in EBL

"Lateral" manipulation of single atoms

5.1 Lateral Manipulation

In the lateral manipulation mode a particle on the sample surface is moved along the surface to the desired location without losing contact to the surface. The motion can be obtained either by dragging or pushing. Figure 31a to d show the build up of a quantum corral by manipulating individual Fe atoms on a Cu(111) surface at 4 K [44]. The final structure of 15 nm diameter consists of 48 Fe atoms. At this stage one may ask how such a fine manipulation can be achieved. The procedure is as follows: Fe atoms are evaporated onto a Cu(111) surface cooled to 4 K. The surface containing statistically distributed Fe atoms is then examined by STM. Normally, no atoms are displaced, but if the distance between tunnelling tip and a Fe atom is reduced, then the tunnelling tip exercises an attractive force on the Fe atom and the Fe atom can be dragged by the tunnelling tip to the desired location on the surface [44], [45]. Once the desired location is reached, the tip is retracted. Increasing the distance between the tip and the sample reduces the tip-Fe atom interactions and, hence, the Fe atom remains at its new position (Figure 32). Figure 31e shows that in this way a whole circle of iron atoms can be built up. The artificially build nanostructure shown in Figure 31 confines the electrons of the two-dimensional surface electron gas on Cu(111). Therefore, as soon as the circle is complete, the electrons are scattered in the circle and form standing electron waves due to quantum mechanics. Figure 31e thus illustrates the wave nature of the electrons.

In a quantum well, due to the quantization of the electron states, not only standing electron waves but also discrete energy values of the electrons are expected. Consequently, increased electron densities should occur at specific energies. As already described, the density of states can be approximately calculated from experimentally measured current-voltage characteristics by calculating $(dI/dV)/(I/V)$. For metals, however, I/V is generally constant and the sample density of states is therefore proportional to dI/dV. The variation of dI/dV as a function of voltage reflects the density of states variation as a function of energy. Figure 33 shows the density of states thus obtained for three different surface positions. At the centre of the circle, as expected, peaked energy levels occur (curve a), whereas outside the circle no structure in the density of states is measurable (curve c). If the density of states is measured at a distance of 0.9 nm from the circle centre, even more energy levels occur as shown by the arrows in curve b.

This example of spectroscopic measurements and of the spatial distribution of the electron waves in a potential well provides a particularly illustrative picture of quantum mechanics. The construction of different quantum structures by an atom-by-atom manipulation approach using scanning probe microscopes nowadays allows a new look into the quantum world and a direct spatial measurement of the electron waves.
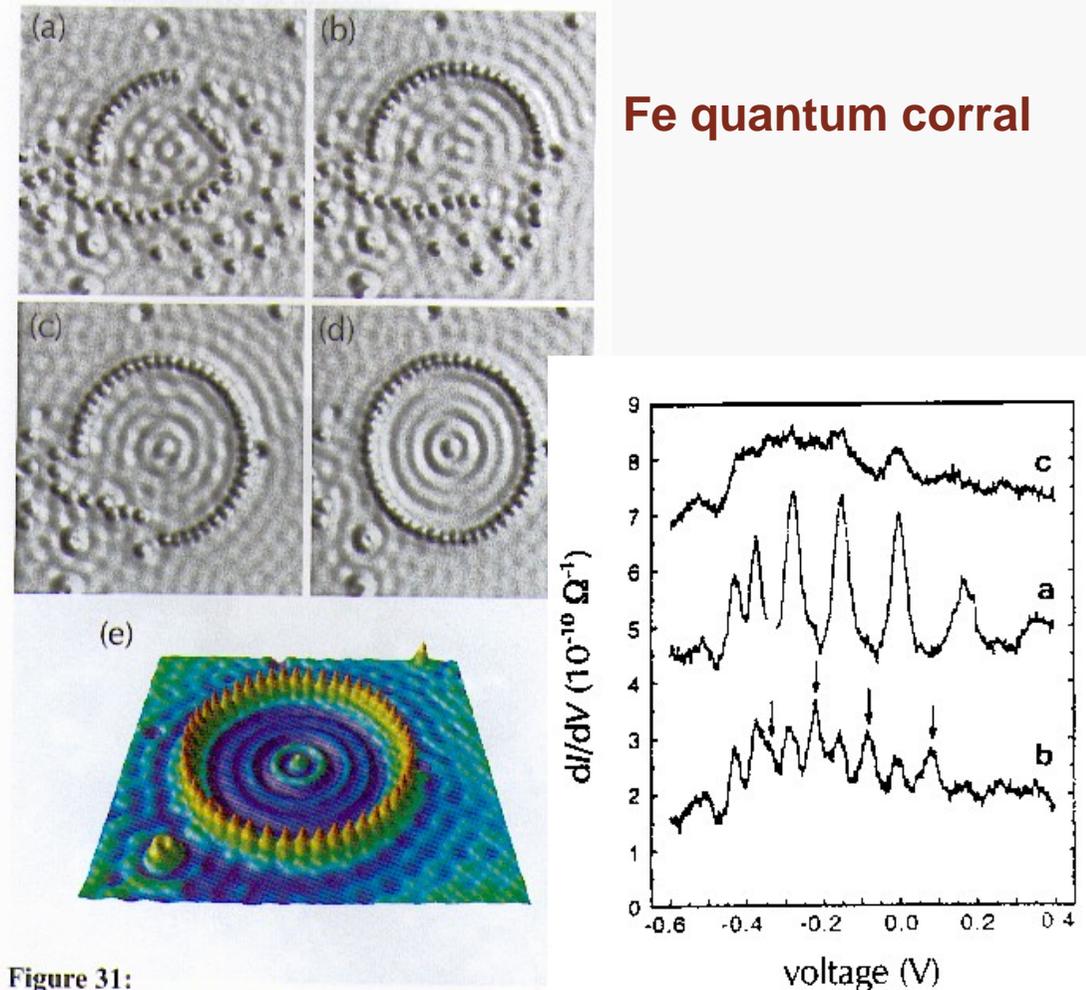
Fe quantum corral

Figure 31:
(a) to (d) show the process of building a quantum corral consisting of 48 Fe atoms positioned on a Cu(111) surface. The resulting structure and the standing waves induced by the quantum confinement of surface electrons in the structure is visible in the three-dimensional view (e) of the quantum corral [44].

Artifical quantum structures can be produced by placing in close proximity different atoms (physisorbed) on a surface

"Lateral" manipulation and surface reconstruction

Instead of evaporating foreign atoms onto a copper surface it is also possible to reconstruct the substrate surface itself, which is more difficult due to the higher coordination number and binding energy of the atoms located in the surface or in steps [49]. The experiments shown here are carried out on Cu(211) substrates at 30 – 40K. In Figure 34 a sphere model of the copper surface is shown, whereby the atoms are shaded darker the deeper they lie. Lateral manipulation of single Cu atoms parallel and perpendicular to step edges is presented in Figure 35 [49]. A measure for the minimum force necessary to move a copper atom is the tunnel resistance which displays the distance between tip and sample. The tunnel resistance used for motion along a step edge was approx. 700 kΩ and ~500 kΩ for moving them over a step edge. Figure 36a – c demonstrate that it is even possible to "dig out" single copper atoms from even higher coordinated sites. The single Cu atom (Figure 36a) is used as a marker. Figure 36b, c show the drag out of single Cu atoms leading to a corresponding vacancies in the initial site of the atoms.

Furthermore instead of moving single atoms, the lateral manipulation technique is also capable to move entire molecules. Gimzweski et al. deposited hexa-*tert*-butyl decacyclene (HB-DC) molecules onto a Cu(100) surface [50]. The decacyclene core of the HB-DC is equipped with six bulky *t*-butyl-legs (Figure 37). At monolayer coverage, the molecules are immobile, forming a two dimensional van der Waals crystal (Figure 38). Separated HB-DC molecules on a Cu(100) surface are extremely mobile, making it impossible to get STM images with atomic resolution.

For this reason a coverage of just less than one monolayer was chosen and STM images resemble those of the immobilized 2-D lattice at full monolayer coverage. However, there are some random voids. In this layer the molecules can be at sites with different symmetry with respect to the surrounding molecules (Figure 39). Molecules at sites of lower symmetry rotate at speeds higher than the scan rate used for imaging and therefore appear as torus Figure 40a. The molecules at the higher symmetry sites are observed as six-lobed images, proving that they are immobile Figure 40b. Gimzweski used the lateral manipulation to drag a rotating HB-DC molecule from a low symmetry site into a higher symmetry site and the six lobes of the immobilized molecule was again clearly observed.
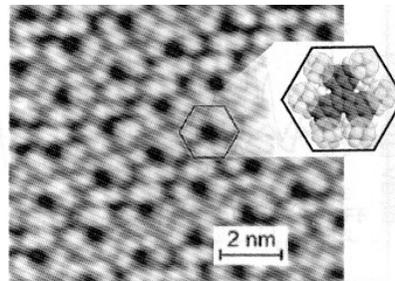

Figure 35: STM image showing the lateral manipulation of a single Cu atom (a) parallel and (b) perpendicular to a step. The motion is indicated by an arrow. In the upper part of the image a single copper atom serves as marker. The processes involved correspond to the motion shown in Figure 34a and b [49].

Surface reconstruction: practically, atoms belonging to the surface can be displaced from one site to another

Figure 40: STM images of a Cu(100) surface after exposure to a coverage just below one complete monolayer of HB-DC molecules at room temperature. In (a) the molecule is imaged as a torus and is in a location where it is not in phase with the overall 2D molecular overlayer. The molecule is rotating. (b) The same molecule is translated by 0.26 nm and imaged as a six-lobed structure in registry with the surrounding molecules. Image area is 5.75 nm by 5.75 nm.

Figure 38: STM image of an Cu(100) surface after exposure to a full monolayer coverage of HB-DC molecules at room temperature. Image area is 11.4 nm by 11.4 nm [50].
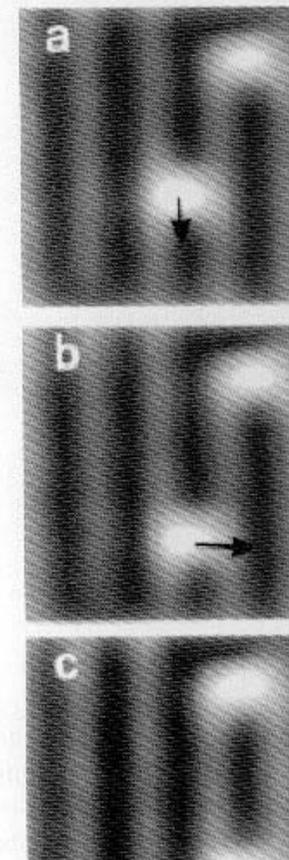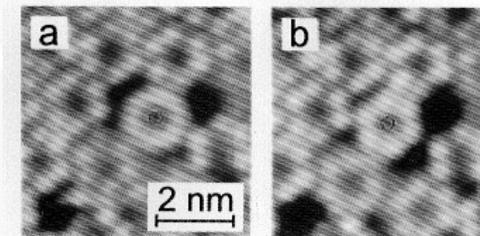
"Vertical" manipulation

5.2 Vertical Manipulation

In the vertical manipulation process, the adparticles are transferred from the sample surface to the tip apex and vice versa [51], [52]. The first experiments on vertical STM manipulation were carried out by Eigler "picking up" Xe atoms [51]. The group of Rieder showed that transferring a Xe atom to the tip apex leads to markedly improved resolution [53]. The single Xe atom obviously "sharpens" the tip.

In Figure 41(a) [54], [55] a schematic presentation of the *pick up* process of a Co molecule from Cu(111) is shown. It is well known that CO molecules stand upright on a Cu(111) surface [56] with the carbon atom bonding to the copper atoms. Due to occasional contact between the tip and the surface some copper atoms are transferred to the tip apex. During the transfer of the CO molecule to the tip, the molecule must consequently rotate. A reliable procedure for transferring the CO to the tip and back to the surface requires ramping of the tunneling voltage and the simultaneous decrease of the tip-surface distance. Figure 41b and c show that scanning with a CO molecule on the tip apex leads to a clear chemical contrast. Figure 41b is scanned with a clean metal tip and all adsorbents appear as depressions. After the transfer of the CO molecule to the tip apex (indicated with an white arrow) and rescanning the area, Figure 41c shows that all CO molecules changed their appearance to protrusions. Only the oxygen atom in the upper left part of Figure 41b and c retains its appearance.

In [57] it has been described, how to combine the potential of single atom manipulation of STM and single atom sensitivity of an atom probe mass spectrum to realize an ultimate technique for surface science. The System used by Shimizu et al. consists of an STM, an atom probe, load lock chambers and a mechanism to transfer tip and sample. The tip can be transferred reversibly between the STM and the atom probe stages. To investigate the pick-up of Si atoms during manipulation, a clean Si surface was approached with a clean tungsten tip applying a bias of + 2 V and 0.3 nA at the sample. After manipulation the tip was transferred from the STM to the atom probe. The atom probe analysis showed the formation of to different layers on top of the tip apex. The top most layer was WSi_2 and the next layer was W_5Si_3, finally the clean tungsten surface appeared. Using this combination of an STM and an atom probe could prove that the tips during manipulation do not only adsorb atoms but furthermore depending on the conditions alloys can be formed.
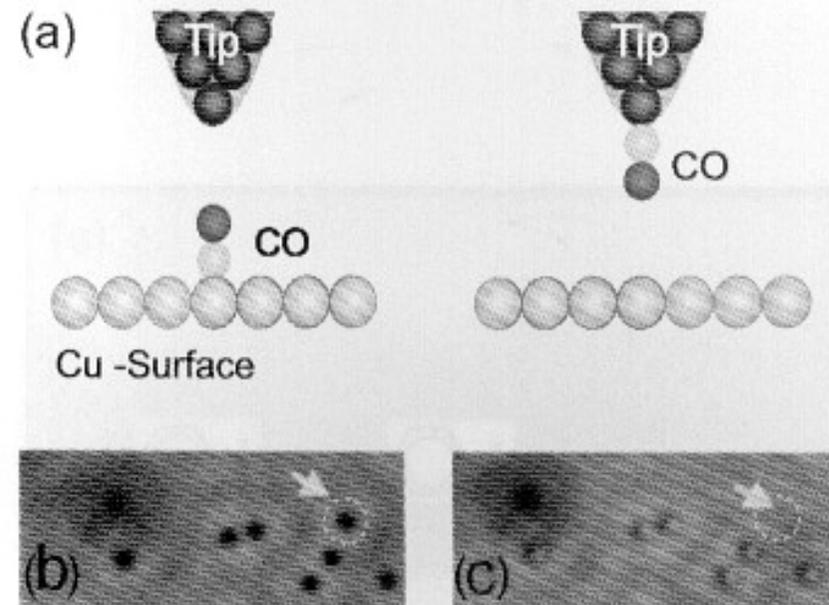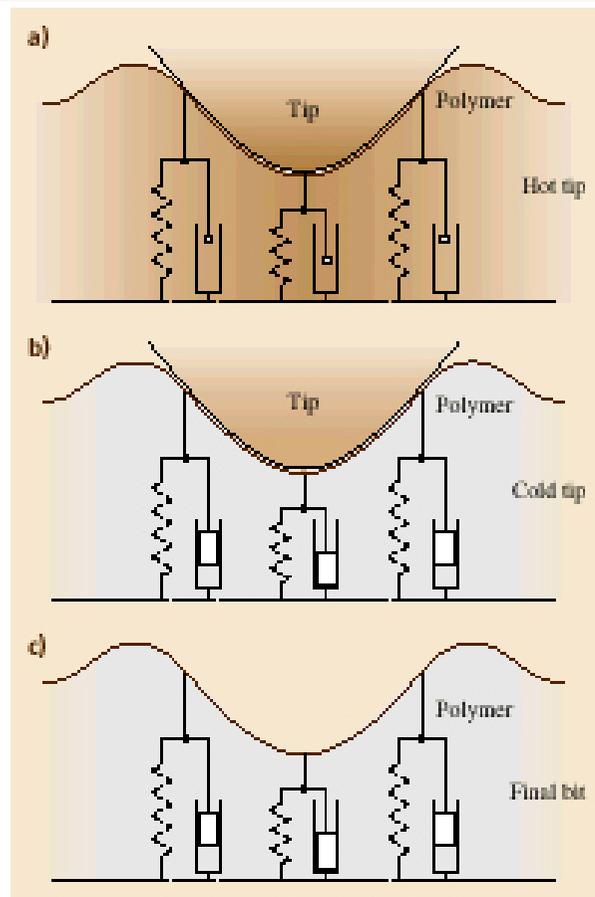

Figure 41:
(a) A sketch of the picking up procedure of CO molecules on Cu(111) surfaces. Notice that the CO molecule stands upright with the carbon atom attached to the surface and has to switch its orientation when being transferred to the tip.
(b), (c) STM images showing the pick up of a CO molecule. Notice the chemical contrast after the pick up [54].

Molecules or atoms can be "trapped" or "released" by the STM tip by simply varying the bias voltage

4.B. Nanoindentation I

31.7 Polymer Medium

The polymer storage medium plays a crucial role in millipede-like thermomechanical storage systems. The thin-film multilayer structure with PMMA as active layer (see Fig. 31.2) is not the only possible choice, considering the almost unlimited range of polymer materials available. The ideal medium should be easily deformable for writing, yet indentations should be stable against tip wear and thermal degradation. Finally, one would also like to be able to erase and rewrite data repeatedly. In or-

---

> **AFM can be used to induce local deformation to (plastic) surfaces**

Fig. 31.19a–c Viscoelastic model of indentation writing. (a) The hot tip heats a small volume of polymer material to more than Θ_g. The shear modulus of the polymer drops drastically from GPa to MPa, which in turn allows the tip to indent the polymer. In response, elastic stress (represented as compression springs) builds up in the polymer. In addition, viscous forces (represented as pistons) associated with the relaxation time for the local deformation of molecular segments limit the indentation speed. (b) At the end of the writing process, the temperature is quenched on a microsecond time scale to room temperature: The stressed configuration of the polymer is frozen-in (represented by the locked pistons). (c) The final indentation corresponds to a metastable configuration. The original unstressed flat state of the polymer can be recovered by heating the indentation volume to more than Θ_g, which unlocks the compressed springs (after [31.15])

der to be able to address all important aspects properly, some understanding of the basic physical mechanism of thermomechanical writing and erasing is required.

31.7.1 Writing Mechanism

In a *gedanken* experiment we visualize writing of an indentation as the motion of a rigid body (the tip) in a viscous medium (the polymer melt). Let us initially assume

---

that the polymer, i.e., PMMA, behaves like a simple liquid after it has been heated above the glass-transition temperature in a small volume around the tip. As viscous drag forces must not exceed the loading force applied to the tip during indentation, we can estimate an upper bound for the viscosity ζ of the polymer melt using Stokes's equation:

$$F = 6\pi\zeta\varrho v. \qquad (31.1)$$

In actual indentation formation, the tip loading force is on the order of $F = 50\,\text{nN}$ and the radius of curvature at the apex of the tip is typically $\varrho = 20\,\text{nm}$. Assuming a depth of the indentation of, say, $h = 50\,\text{nm}$ and a heat pulse of $\tau_h = 10\,\mu\text{s}$ duration, the mean velocity during indentation formation is on the order of $v = h/\tau_h = 5\,\text{mm/s}$. Note that thermal relaxation times are on the order of microseconds [31.20, 21] and, hence, the heating time can be equated to the time it takes to form an indentation. With these parameters we obtain $\zeta < 25\,\text{Pa}\,\text{s}$, whereas typical values for the shear viscosity of PMMA are at least seven orders of magnitude larger even at temperatures well above the glass-transition point [31.39].

This apparent contradiction can be resolved by considering that polymer properties are strongly dependent on the time scale of observation. At time scales on the order of 1 ms and below, entanglement motion is in effect frozen in and the PMMA molecules form a relatively static network. Deformation of the PMMA now proceeds by means of uncorrelated deformations of short molecular segments, rather than by a flow mechanism involving the coordinated motion of entire molecular chains. The price one has to pay is that elastic stress builds up in the molecular network as a result of the deformation (the polymer is in a so-called rubbery state). On the other hand, corresponding relaxation times are orders of magnitude smaller, giving rise to an effective viscosity at millipede time scales on the order of 10 Pa s [31.39], as required by our simple argument (see (31.1)). Note that, unlike normal viscosity, this high-frequency viscosity is basically independent of the detailed molecular structure of the PMMA, i.e., chain length, tacticity, polydispersity, etc. In fact, we can even expect that similar high-frequency viscous properties can be found in a large class of other polymer materials, which makes thermomechanical writing a rather robust process in terms of material selection.

> In thermoplastic materials, deformation can be recovered (as in the *millipede*!)
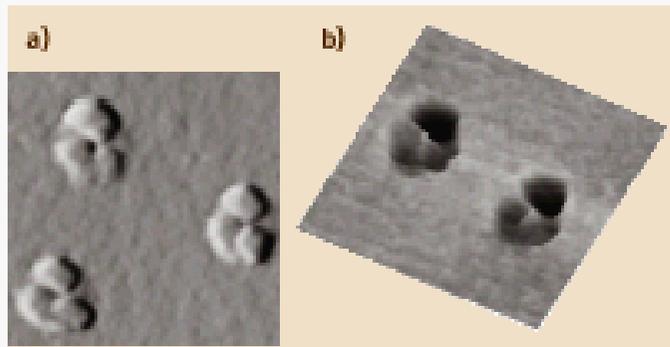
Nanoindentation II

Fig. 31.20a,b Topographic image of individual indentations. (a) The region around the actual indentations clearly shows the threefold symmetry of the tip, here a three-sided pyramid. (b) The indentations themselves exhibit sharp edges, as can be seen from the inverted 3-D image. Image size is $2 \times 2\,\mu m^2$ (from [31.15] © 2002 IEEE)
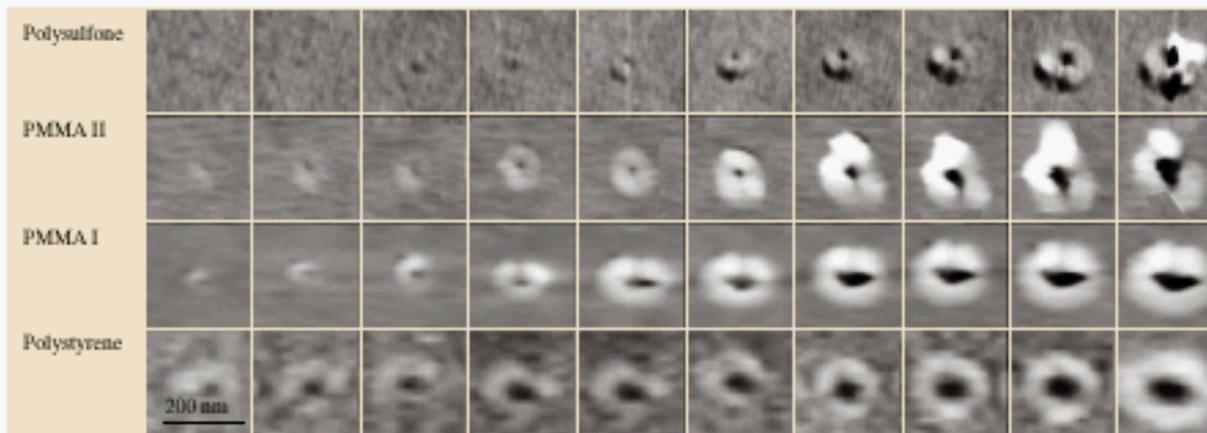
Fig. 31.21 Written indentations for different polymer materials. The heating pulse length was 10 μs, the load about 10 nN. The grey scale is the same for all images. The heater temperatures for the indentation on the left-hand side are 445, 400, 365, and 275 °C for the polymers Polysulfone, PMMA II (anionically polymerized PMMA, $M \approx 26$ k), PMMA I (Polymer Standard Service, Germany, $M \approx 500$ k), and Polystyrene, respectively. The temperature increase between events on the horizontal axis is 14, 22, 20, and 9 °C, respectively (from [31.15] © 2002 IEEE)
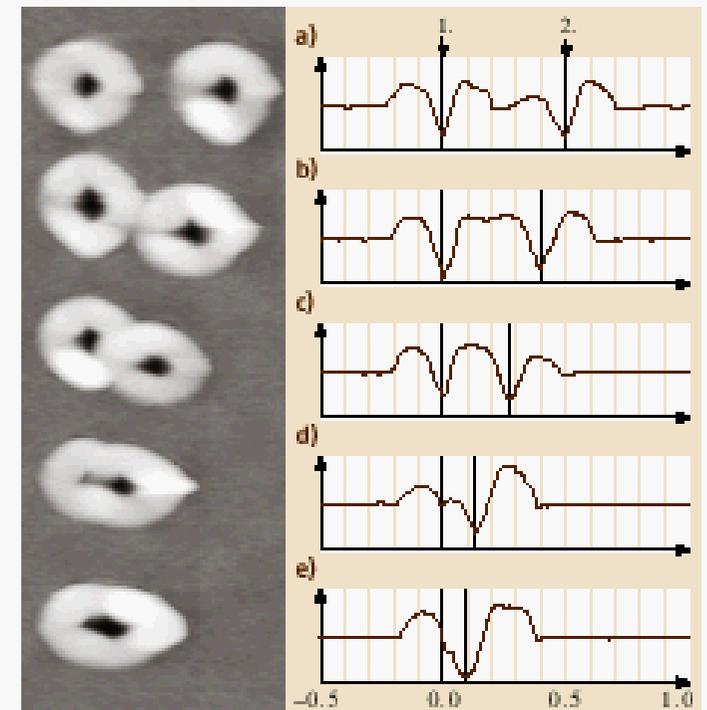

Fig. 31.24a–e Indentations in a PMMA film at several distances. The depth of the indentations is ~ 15 nm, roughly the same as the thickness of the PMMA layer. The indentations on the left-hand side were written first, then a second series of indentations was made with decreasing distance from the first series going from (a) to (e) (after [31.15])
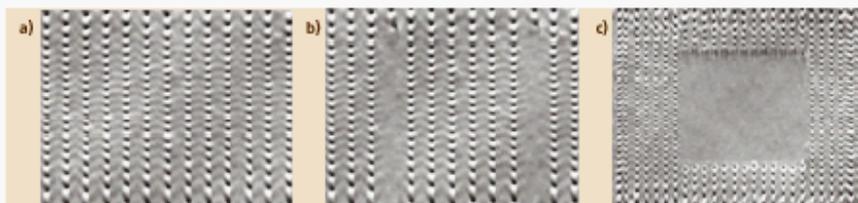

Fig. 31.25a–c Demonstration of the new erasing scheme: (a) A bit pattern recorded with variable pitch in the vertical axis (fast scan axis) and constant pitch in the horizontal direction (slow scan axis) was prepared. (b) Then two of the lines were erased by decreasing the pitch in the vertical direction by a factor of three, showing that the erasing scheme works for individual lines. One can also erase entire fields of indentations without destroying indentations at the edges of the fields. This is demonstrated in (c), where a field has been erased from an indentation field similar to the one shown in (a). The distance between the lines is 70 nm (from [31.15] © 2002 IEEE)

Da B. Bhushan, Handbook of nanotechnology (Springer, 2003)

4.C Nanowriting with SNOM I

Photosensitive polymer sample

Polymethacrylate (PMA) network, modified in the four position with an azobenzene mesogenic unit (3-methyl-4'-pentyloxy) connected to the main chain by an hexamethylene spacer (PMA4)
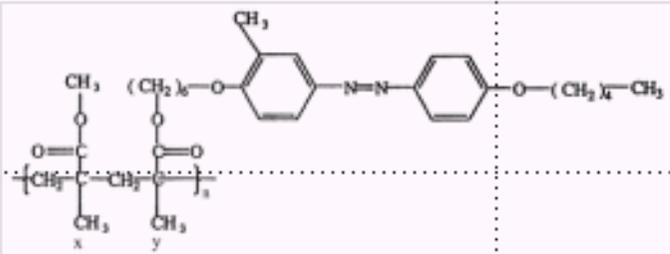
**PMA4
chemical structure
homopolymer ($x = 0$)
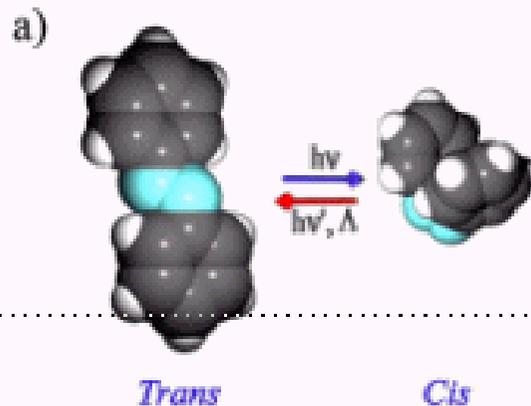co-polymer ($x \neq 0$)**

Samples preparation

· highly concentrated solution of PMA4 powder dissolved in chlorobenzene, stirred at room temperature for a few hours

· thermal treatment before impression

· film from single drops of solution on Corning 4079 glass substrate and spinning at ~ 2000 - 10000 rpm.

· T_g = 294 K.

· Above T_g, nematic phase up to T_c ~ 353 K.

· Conformational transition at 320 K.

· Film thickness ~ 100 - 200 nm.

Near field produced by a SNOM tip can be (obviously) used to induce local modifications of light sensitive materials:
sub-diffraction resist-assisted optical lithography can be envisioned as well as nanowriting for data storage

Nanowriting accomplished frequently on azobenzene containing molecules in order to exploit the photoisomerization of this photosensitive polymer *(as we have already seen)*

a)

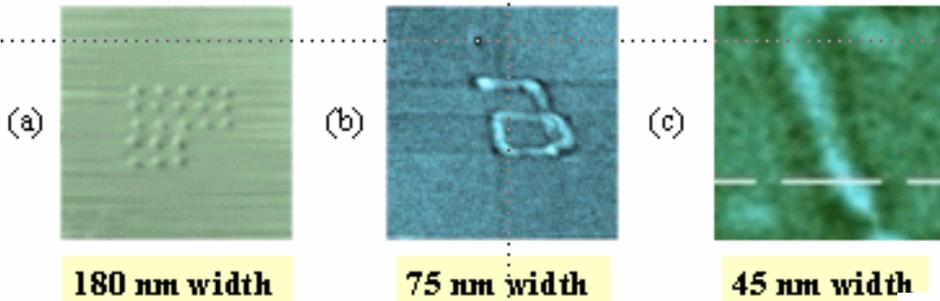Trans-cis photoisomerization of the azobenzene moiety.

b)

$\pi-\pi^*$
trans-cis

$\pi-\pi^*$
$n-\pi^*$
trans-cis-trans

Absorbance

Wavelength (nm)
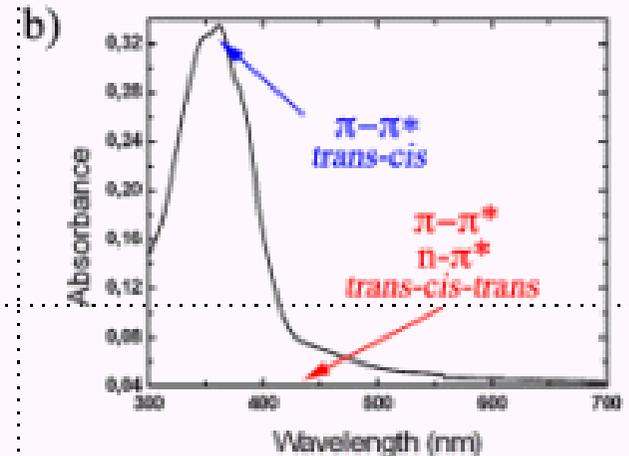
Absorption spectrum

SNOM topography images of the optically
nanostructured PMA4 thin film

(a) homopolymer (exposure time = 1 s/dot, image size = 5 x 5 μm²)

(b) 30/70 copolymer (sensor speed = 20 nm/s, size = 2 x 2 μm²)

(c) 30/70 copolymer (speed = 50 nm/s, size = 300 x 300 nm²)

(a)   (b)   (c)

180 nm width   **75 nm width**   **45 nm width**

[S. Patanè, A. Arena, M. Allegrini,
L. Andreozzi, M. Faetti, and M. Giordano,   Opt. Commun. 210, 37 (2002)]

Topographical nanowriting (due to local photoinduced mass migration)

All optical nanowriting based on birifringence induced by photoisomerization cycles of azo-molecules (it can be detected by PM-SNOM)

PHOTOINDUCED BIREFRINGENCE

Topography [< 2 nm]   Optical images
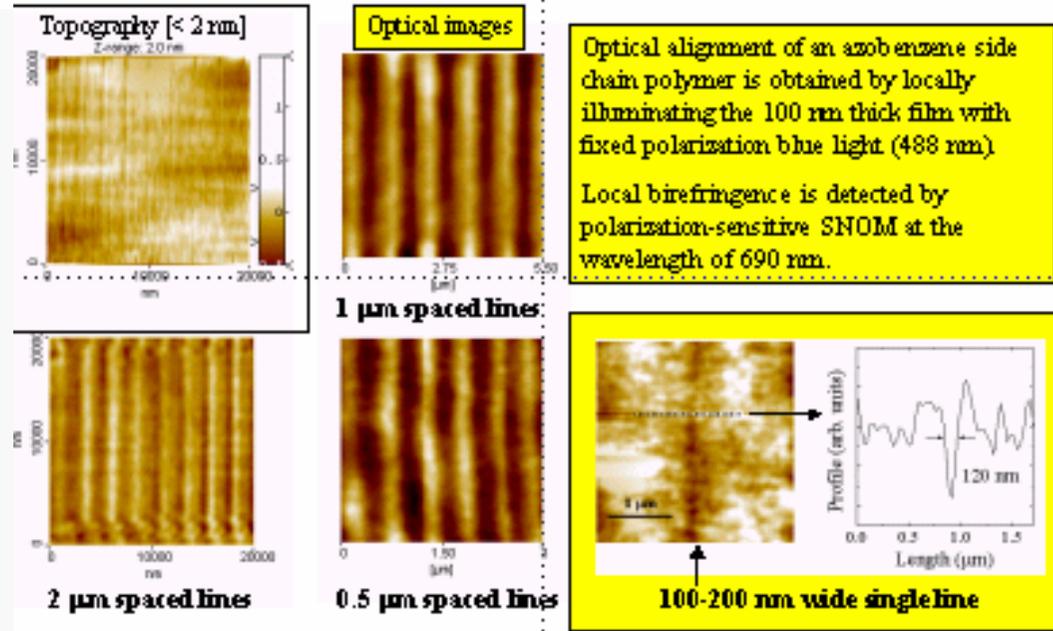
Optical alignment of an azobenzene side chain polymer is obtained by locally illuminating the 100 nm thick film with fixed polarization blue light (488 nm).

Local birefringence is detected by polarization-sensitive SNOM at the wavelength of 690 nm.

1 μm spaced lines

2 μm spaced lines   **0.5 μm spaced lines**   **100-200 nm wide single line**

120 nm

Profile (arb. units)

Length (μm)

V. Likodimos, M. Labardi, L. Pardi, M. Allegrini, M. Giordano, A. Arena, S. Patanè, APL 83, 2212 (2003)

Conclusions

✓ Scanning Probe techniques have been developed thanks to advances in material fabrication (atomic probes), electronics (and piezoelectric translators), and *methods of operation* (e.g., the role of feedback)

✓ Space resolution is excellent in SPMs (at the "atomic level" for some of them)

✓ Most important: physical quantities can be *measured* (in quantitative terms) with SPM, as topographical height, surface density of states, optical properties, ...

✓ Many SPMs have been developed, and the list is still growing

✓ The excellent space control offered by SPM can be exploited also for fabrication (nanomanipulation) purposes, leading to techniques with a poor applicative potential (slow, complicated), but with enormous capabilities in a bottoms-up context, compatible also with "soft" (typ organic) matter